NIST Technical Note 1954

3.5 GHz Radar Waveform Capture at Point Loma

Final Test Report

Paul Hale
Jeffrey Jargon
Peter Jeavons
Michael Souryal
Adam Wunderlich
Mark Lofquist

This publication is available free of charge from:
https://doi.org/10.6028/NIST.TN.1954

National Institute of Standards and Technology
U.S. Department of Commerce

NIST Technical Note 1954

3.5 GHz Radar Waveform Capture at Point Loma
Final Test Report

Paul Hale
Jeffrey Jargon
Peter Jeavons
Michael Souryal
Adam Wunderlich
Communications Technology Laboratory

Mark Lofquist
MITRE Corporation
Boulder, Colorado

This publication is available free of charge from:
https://doi.org/10.6028/NIST.TN.1954

May 2017

U.S. Department of Commerce
Wilbur L. Ross, Jr., Secretary

National Institute of Standards and Technology
Kent Rochford, Acting NIST Director and Under Secretary of Commerce for Standards and Technology

National Institute of Standards and Technology Technical Note 1954
Natl. Inst. Stand. Technol. Tech. Note 1954, 96 pages (May 2017)
CODEN: NTNOEF

This publication is available free of charge from:
https://doi.org/10.6028/NIST.TN.1954

NASCTN Report 2

NIST Technical Note 1954

3.5 GHz Radar Waveform Capture at Point Loma

Final Test Report

Paul Hale, Ph.D., Jeffrey Jargon, Ph.D., Peter Jeavons,
Michael Souryal, Ph.D., Adam Wunderlich, Ph.D.
Communications Technology Laboratory, NIST

Mark Lofquist
MITRE Corporation

May 3, 2017

NASCTN

National Advanced Spectrum and Communications Test Network

Cleared for Open Publication 1 May 2017 by the Department of Defense
Office of Prepublication and Security Review, Reference Number: 17-S-1281

National Advanced Spectrum and Communications Test Network (NASCTN)

The mission of the National Advanced Spectrum and Communications Test Network (NASCTN) is to provide, through its members, robust test processes and validated measurement data necessary to develop, evaluate and deploy spectrum sharing technologies that can increase access to the spectrum by both federal agencies and non-federal spectrum users.

The U.S. Department of Commerce's National Institute of Standards and Technology (NIST) and National Telecommunications and Information Administration (NTIA) established the Center for Advanced Communications (CAC) in Boulder, Colorado, to address, among other challenges, the increasing need for spectrum sharing testing and evaluation capabilities to meet national needs. As part of CAC's mission to provide a single focal point for engaging both industry and other government agencies on advanced communication technologies, including testing, validation, and conformity assessment, NASCTN was formed under the umbrella of the CAC. NIST hosts the NASCTN capability at the Department of Commerce Boulder Laboratories in Boulder, Colorado. NASCTN is a membership organization under a charter agreement. Members

- Make available, in accordance with their organization's rules policies and regulations, engineering capabilities and test facilities, with typical consideration for cost.
- Coordinate their efforts to identify, develop and test spectrum sharing ideas, concepts and technology to support the goal of advancing more efficient and effective spectrum sharing.
- Make available information related to spectrum sharing, considering requirements for the protection of intellectual property, national security, and other organizational controls, and, to the maximum extent possible, allow the publication of NASCTN test results.
- Ensure all spectrum sharing efforts are identified to other interested members.

Current charter members are:

- National Telecommunications and Information Administration (NTIA)
- National Institute of Standards and Technology (NIST)
- Department of Defense Chief Information Officer (DoD CIO)

Acknowledgments

We thank the Department of Defense and Space and Naval Warfare (SPAWAR) Systems Center Pacific for providing access to the measurement site at Point Loma; Michael Cotton and his colleagues at the National Telecommunications and Information Administration (NTIA), Institute for Telecommunications Sciences (ITS), Boulder, Colorado, for the use of the pre-selector; Frank Sanders at NTIA/ITS for sharing his expertise on radar systems and measurements; John Ladbury at NIST for characterizing the antennas we used in our measurements; and the NASCTN staff for stakeholder management, project management, and coordination.

Executive Summary

In view of recently adopted Federal Communications Commission (FCC) rules to share the spectrum from 3550 MHz to 3700 MHz between federal and commercial users, NASCTN launched a measurement effort to create a library of high-fidelity waveforms of federal incumbent radar signals currently operating in the 3550 MHz to 3650 MHz ("3.5 GHz") band. The purpose of this waveform library is to facilitate the development and testing of a commercial environmental sensing capability (ESC) that will detect federal incumbent systems and permit spectrum sharing in U.S. coastal exclusion zones, in accordance with FCC rules.

The primary federal incumbent in the 3.5 GHz band is the U.S. Navy shipborne SPN-43 air traffic control radar, as well as other Department of Defense (DoD) ground-based radar systems. Since the focus of this study was on the shipborne radar, measurements were conducted at two coastal locations, Point Loma, near San Diego, California, and Virginia Beach, Virginia. This report documents the methodology and results of the measurements collected at Point Loma, and a subsequent report will document the Virginia Beach measurements.

Measurements were collected at Point Loma over a two-month period. They consist of 60-second power spectral measurements collected every 10 minutes as well as high-resolution in-phase and quadrature (IQ) digital waveforms covering the entire band in question and portions of adjacent bands. The digital waveforms were retained if energy was detected above a predefined threshold in the band of interest. The majority of these measurements were made with an omnidirectional, slant-polarized antenna, and the remainder were made with a directional, cavity-backed spiral antenna.

The Point Loma measurement campaign resulted in a total of 8543 60-s power spectra and 1863 high-resolution 60-s waveforms. Over the course of these measurements, the target SPN-43 radar system was observed at three different operational frequencies: 3520 MHz, 3550 MHz, and 3600 MHz. In addition to observing SPN-43 at these frequencies in "normal" operation, the following phenomena were observed and are documented in this report:

- Tuning of the radar across a contiguous range of frequencies

- Two radars operating simultaneously on the same frequency channel
- Adjacent-band emissions into the band of interest
- In-band, frequency-hopping, narrowband emissions from an unknown source.

Furthermore, the adjacent-band emissions were frequently observed to be coincident and co-channel with SPN-43 emissions, indicating that the adjacent-band emissions could confound SPN-43 detection by an ESC.

A subset of the high-resolution IQ waveforms containing negligible adjacent-band or other in-band emissions was selected for further statistical analysis. This analysis focused on key parameters of the target radar that could aid detection, namely, the antenna rotation period, pulse repetition interval, pulse duration, and center frequency. The subset of approximately 800 acquisitions of in-band radar consisted of about 11 300 sweeps of the main beam and nearly 223 000 individual pulses ranging in peak power by over 40 dB. The statistical analysis of in-band radar parameters yielded the following observations:

- The median antenna rotation period was 3.85 s, 0.15 s lower than reported in the SPN-43 system manual dated 2005. The difference between the 1st and 99th percentiles (containing 98 % of the observations) was only 0.05 s.
- The median pulse repetition interval was very close to the nominal value of 1 ms (only 13 ns greater). Furthermore, 98 % of the values were confined to a range of only 40 ns.
- The overall median pulse duration was 1.17 μs and varied by 0.027 μs across the three observed frequencies. However, the tails of their distributions differed more significantly, with the 98 % spread reaching 0.4 μs, or 34 % of the median. The median pulse duration observed here differs by 0.22 μs from that reported in the SPN-43 system manual dated 2005.
- The median frequency offset from the nominal center frequency ranged from 43 kHz to 690 kHz across the three observed frequencies, and their 98 % spreads varied from 384 kHz to 1.15 MHz.

Knowledge of these statistics can be used to develop robust ESC detectors. They can also inform the development and selection of waveforms with which these detectors can be tested by a certification body. Furthermore, the waveforms themselves could be "played back"—that is, converted to an analog signal and upconverted to the appropriate radio frequency (RF)—by a vector signal generator to evaluate the performance of an ESC detector. A benefit of playing back the measured waveforms is that the effects of the propagation channel, which can distort the signal, are inherent in these waveforms. Hence, the measured waveforms better reflect the actual signals an ESC will receive in the field.

While the focus of this study was on currently deployed shipborne radars in the band of inter-

est, an important consideration in future work is the class of more sophisticated radars yet to be deployed in this band and which will also need to be detected by commercial users and protected from harmful interference. It is unlikely that the waveforms of these future systems will be shared with commercial users for development of their detectors, hence there is a need to develop and validate surrogate waveforms that adequately represent them.

Another area of interest for future research is the development and validation of 3.5 GHz channel models. These models would be of use to commercial developers of Spectrum Access Systems for 3.5 GHz, which must predict and manage aggregate interference to federal and other incumbents. Furthermore, wideband channel impulse response models, that include the effects of a multipath channel on the pulse shape, would have value in the testing of ESC detectors. They could be used in conjunction with surrogate radar waveforms to render them more representative of the signals that ESC detectors will observe in the field.

Contents

Acronyms

ADC	analog-to-digital converter
BPF	bandpass filter
CAC	Center for Advanced Communications
CBRS	Citizens Broadband Radio Service
CBS	cavity-back spiral
CDF	cumulative distribution function
CCDF	complementary cumulative distribution function
DoD	Department of Defense
ESC	environmental sensing capability
FCC	Federal Communications Commission
FFT	fast Fourier transform
GbE	gigabit ethernet
IQ	in-phase and quadrature
ITS	Institute for Telecommunication Sciences
LNA	low-noise amplifier
LTE	long term evolution
NASCTN	National Advanced Spectrum and Communications Test Network
NEP	noise equivalent power
NIST	National Institute of Standards and Technology
NTIA	National Telecommunications and Information Administration
OSLT	open-short-load-thru
RAID	redundant array of independent disks
RF	radio frequency
SFDR	spur-free dynamic range
SNR	signal-to-noise ratio
VNA	vector network analyzer
VST	vector signal transceiver

List of Figures

List of Tables

Chapter 1

Introduction

FCC rules issued in April 2015 for the Citizens Band Radio Service (CBRS) permit commercial users to offer wireless broadband services in the 3550 MHz to 3700 MHz band ("3.5 GHz band") currently occupied by federal and non-federal incumbents [1, 2]. As part of the CBRS architecture, an environmental sensing capability (ESC) will facilitate the coexistence of CBRS users with federal incumbent users through signal sensing and detection of the incumbent signal, permitting CBRS devices to be assigned non-interfering channels in otherwise excluded areas. The federal incumbents in this band include U.S. Navy radar systems. There is a need for measurements and methodologies with which to test and evaluate the ability of an ESC detector to detect the presence of a signal from a federal system in and adjacent to the 3.5 GHz band. More specifically, there is a need for representative waveforms of federal incumbent signals with which to design and test the ESC detectors.

In this document, we describe the first phase of an effort to create a library of high-fidelity 3.5 GHz federal incumbent radar waveforms that can be used by CBRS ESC providers, federal regulators, and the DoD for ESC design, training, and testing. In this first phase, we measured 3.5 GHz band waveforms at Point Loma, near San Diego, California. The library contains measured waveforms that are representative of the waveforms that ESCs will be required to detect, particularly targeting SPN-43 emissions between 3550 MHz and 3650 MHz. Recording actual emissions allows for both qualitative and quantitative characterization of Navy system emissions that have only loosely been described in the open literature. In order to quantify variations in the waveforms that will be received by the ESCs due to the differences in the deployed radar equipment and due to the effects of dispersion, multipath fading, and loss in the propagation channel, the library contains measurements of SPN-43 signals emitted from a diversity of littoral sources and power levels. We also collected measurements with two different antennas to increase the diversity of channels measured. In a second phase of the effort, to be reported in a later document, we measured 3.5 GHz band waveforms at Fort Story, near Virginia Beach, Virginia.

Transmitter	1973 Specification [3, 4]	2005 Specification [5]
Tuning range (MHz)	3590 to 3700	3500 to 3700
Pulse generation method	Magnetron	Magnetron
Pulse repetition interval (μs)	$889(\pm 25)$	1000
Pulse duration (μs)	$0.9(\pm 0.15)$	$0.95(\pm 0.05)$
Peak power output (kW)	$850(\pm 150)$	1000
Antenna		
Polarization	Horizontal or left-hand circular, switchable	
Gain (boresight, dBi)	32	> 33.4
Rotation period (s)	4	4

Table 1.1: Relevant parameters of SPN-43 radar from the most current 2005 specification [5], which differs somewhat from the 1973 specification in [3] and [4], particularly in pulse repetition interval, peak power, and antenna gain.

Operating parameters of the SPN-43 radar system have not been readily available to the public. Some generic specifications of SPN-43 were listed in [3] (which were also repeated in [4]). Updated specifications are given in [5] and are listed in Table 1.1. A description of SPN-43 capabilities and how the system is used operationally is given in [6]. NTIA has had previous projects concerned with measuring various aspects of SPN-43 emissions. High dynamic range measurements of the spectra of SPN-43 emissions at a ground-based site were previously reported in [7]. Spectra, however, do not fully describe the individual radar pulses or beam sweep because they do not include phase information, and so cannot be used to reconstruct the signal waveforms for testing purposes. A small number of IQ waveforms were also recorded for that effort but only characterize the operation of a particular source with distortion due to that particular over-land channel, and the number of recorded waveforms are not adequate to develop a statistical characterization of the radar signals. Reference [4] reports representative time-domain recordings of the SPN-43 antenna rotation, pulse repetition interval, and pulse shape, but the number and diversity of recorded waveforms are again not adequate for a statistical characterization.

In Chapter 2 we describe the measurement equipment and methodology we used to assemble a library of digitally sampled and stored waveforms emitted by SPN-43 and other systems in the 3.5 GHz band. The library is comprised of 1863 waveforms, of about 60 s duration and 200 MHz bandwidth, recorded after down-conversion and sampling of the in-phase and quadrature (IQ) components. These waveforms give detailed information on the radar pulses and can be used to synthesize or "play back" realistic signals for ESC training or testing. The library also contains 8543 metadata files with aggregated, low-resolution, spectrograms and aggregated, low-resolution, time-domain data. In Chapter 3, we describe qualitative behavior and usage of SPN-43 as well as other observed occupants of the 3.5 GHz band. Chapter 4 summarizes statistics of the sweep and pulse parameters of a high signal-to-noise ratio (SNR) subset of the IQ waveforms. This subset includes 800 waveforms, 11 300 sweeps of the radar over our location, and 223 000 individual

pulses. In Chapter 5 we draw conclusions on the work, and in Chapter 6 we describe future work that could build on the present report.

Chapter 2

Test Summary

2.1 Measurement configuration

The primary goal of this effort was to collect high fidelity measurements of radar emissions in the 3.5 GHz band at Point Loma. After initial setup and validation, we acquired measurements over a period of two months with the objective of capturing the emissions of a number of SPN-43 systems. To facilitate future testing of ESCs, we recorded waveforms that could be played back in real time. We determined, from industry requirements being developed [8], that we needed to record waveforms with at least 60 s duration. With strong emissions from Radar 3 in the adjacent 3100 MHz to 3500 MHz band [7, 9], we also wanted to be able to investigate signals in the 3.5 GHz band conditioned on occupancy of the 3100 MHz to 3500 MHz band. Finally, we conjectured that environmental conditions (temperature, humidity, barometric pressure, and wind speed) might have an influence on the measured waveforms, so we monitored these quantities during the measurement campaign.

2.1.1 Location

The location for data collection met the following criteria: known SPN-43 activity, clear line of sight view of the ocean over approximately 180 ° azimuth, and data and equipment security. Arranged in coordination with the DoD, the location used for the measurement campaign reported here is at the naval base at Point Loma, near San Diego, CA, specifically a small tower at 32 ° 41' 39" N, 117 ° 14' 49.6" W (see Figs. 2.1–2.4).

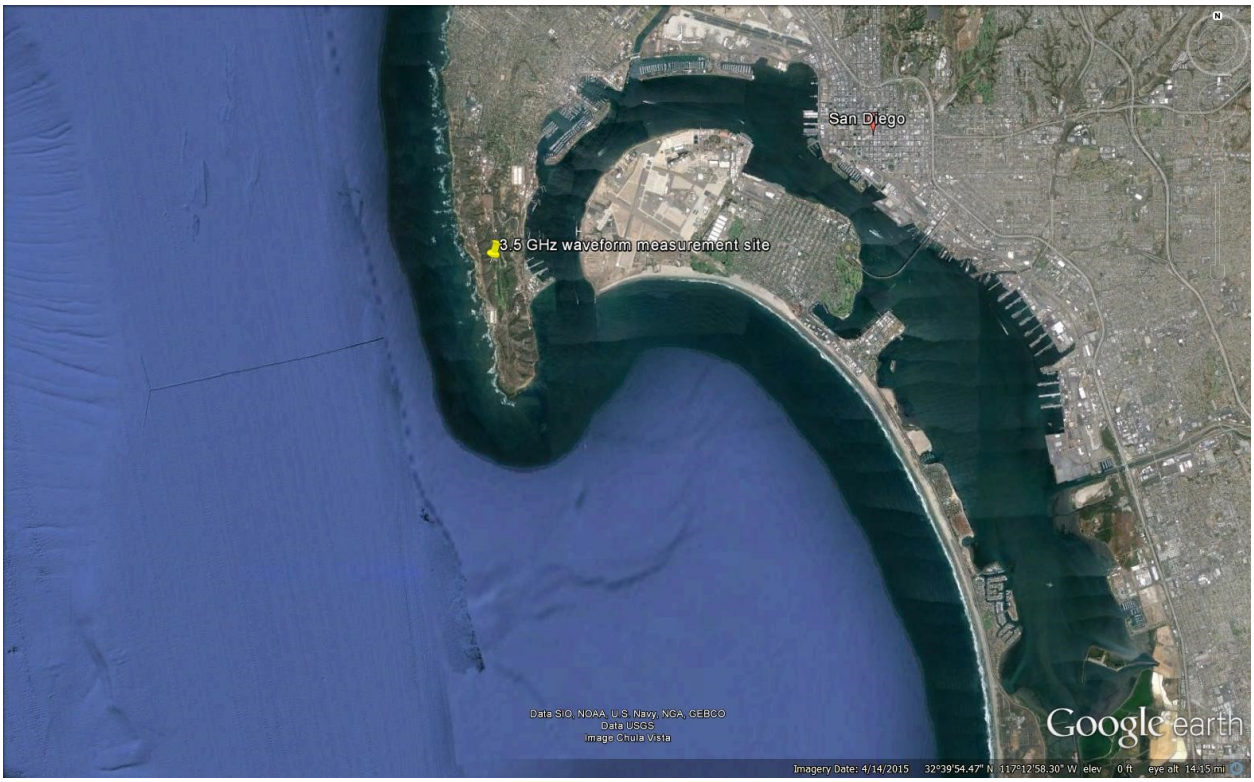

Figure 2.1: View of Point Loma measurement site from 22.8 km altitude. The opening to San Diego Bay is due East of the measurement site.

2.1.2 Measurement system

The equipment used for this measurement campaign is illustrated in Fig. 2.5, and included:

- two antennas (used separately) for capturing the emissions of SPN-43 systems
- a short cable from the output of the antenna to the input of the pre-selector
- the pre-selector, which consisted of a bandpass filter (BPF) and a low-noise amplifier (LNA) contained in a shielded box, with filtered power supply
- a long cable from the output of the pre-selector to the input of the splitter/isolator box
- the splitter/isolator box, which split the power of the incoming signal into two channels to enable multiple analyzers to make measurements simultaneously
- the receiver, which consisted of a Vector Signal Transceiver (VST) in conjunction with a controller
- two pairs of RAID (redundant array of independent disks) drives (one pair for storage, and the other for backup)

Figure 2.2: View of Point Loma measurement site from 601 m altitude. Measurement tower indicated with yellow arrow. Red dashed line indicates approximate crest of hill to the East of measurement tower.

Figure 2.3: View of measurement tower from the Northeast at ground level, looking Southwest.

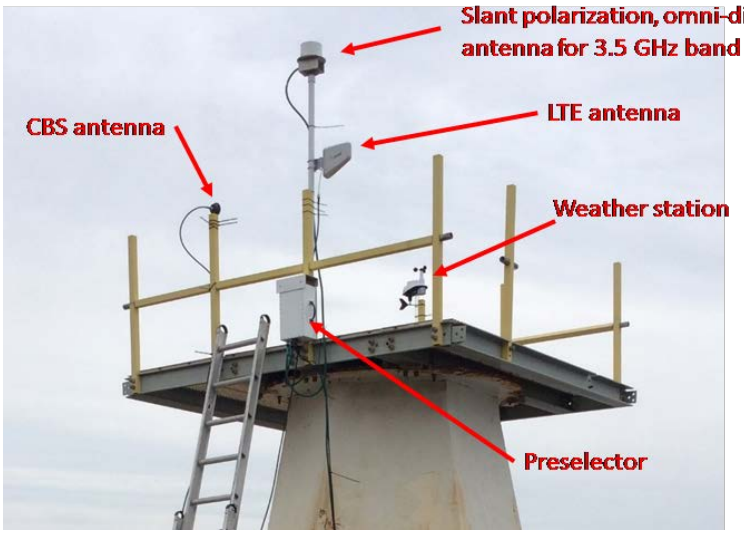

Figure 2.4: Detail of measurement tower showing equipment deployment, including cavity-backed spiral (CBS) antenna and omni-directional antenna. Antenna height above sea level is approximately 122 m.

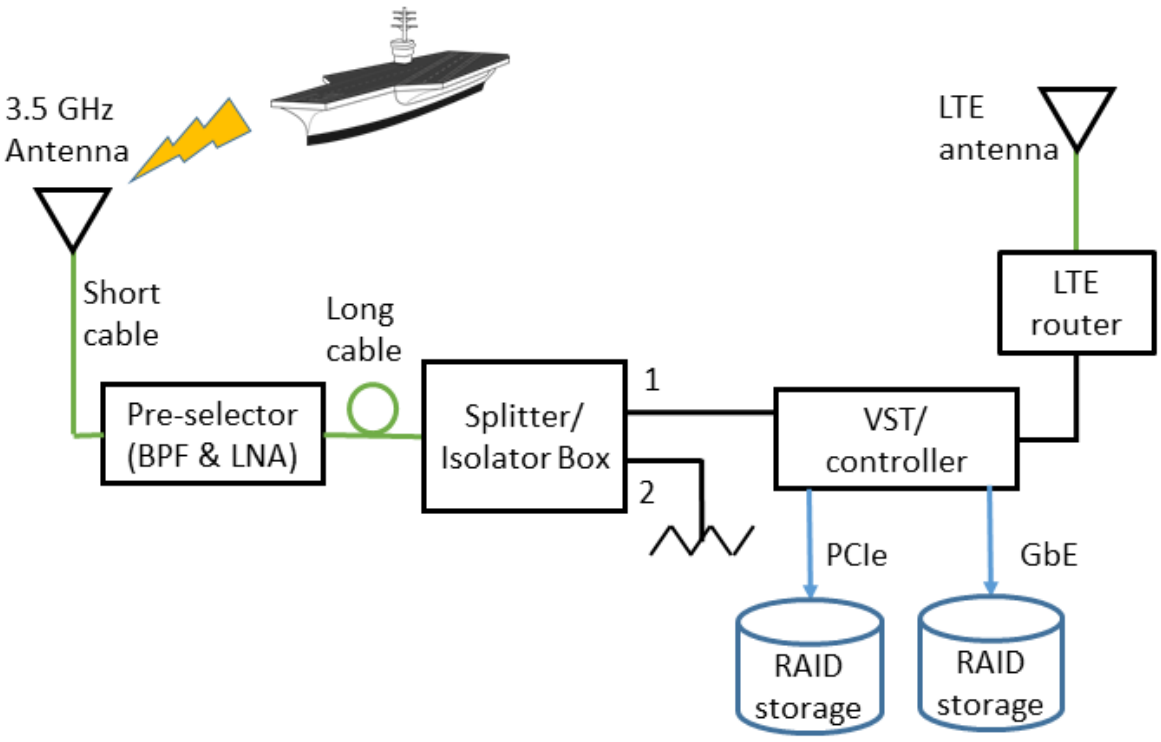

Figure 2.5: Schematic diagram of measurement system

- an LTE (long term evolution) router for remote access and control of the controller
- an LTE antenna
- and a weather station for tracking temperature, humidity, precipitation, and wind speed.

We used two different types of antennas for capturing SPN-43 emissions to add to the diversity of propagation channels. A slant-polarization, omnidirectional antenna was placed in the system for the first half of the measurement campaign, and a cavity-backed spiral (CBS) antenna was placed in the system for the second half. The CBS antenna was pointed due west with zero elevation angle. The short cable connecting the output of the antenna to the pre-selector was low-loss (approximately 1 dB of insertion loss) and included Type-N connectors.

The pre-selector was constructed by the Institute for Telecommunication Sciences (ITS), the research and engineering arm of the National Telecommunications and Information Administration (NTIA). The unit we borrowed (Serial Number PS4) was capable of switching between 3.0 GHz and 3.5 GHz bandpass filters; we made use of the 3.5 GHz bandpass filter in series with the LNA for signal selection and amplification purposes. The overall gain of the pre-selector was approximately 29.2 dB.

Since the pre-selector was located on the roof of the tower near the antenna, a long cable was required to connect to the input of the splitter/isolator box, which was located inside the bottom of the tower along with the VST, the RAID drives, and the LTE router. This long cable was low-loss (approximately 2.6 dB of insertion loss) and included Type-N connectors.

The splitter/isolator box served to split the incoming signals into two paths, each of which contained an isolator in an attempt to prevent the two potential analyzers from interfering with one another.[1] Channel 1 of the splitter/isolator box had an overall insertion loss of about 5.9 dB.

The Channel 1 output of the splitter/isolator box was fed into the receiver, a National Instruments (NI) PXIe-5646R VST, while the second channel was connected to a 50 Ω termination.[2] The VST uses a direct down conversion technique, with the LO frequency f_{LO} centered in the band of interest. This means that signal frequencies $f_s = f_{LO} \pm \Delta$ are down converted to $\pm\Delta$. The output of the down converter is then fed to an IQ demodulator, whose quadrature outputs are sampled (synchronously) with ADCs, each supporting a sample rate of up to 250 MSamples/s and a sample resolution of 14 bits. The system frequency range is specified to be between 65 MHz and 6.0 GHz, with a bandwidth of 200 MHz ($\pm$100 MHz around f_{LO}). The VST was contained in an NI PXIe-1085 chassis along with an NI PXIe-8880 embedded controller. Our data collection

[1] Our initial measurement plan included a spectrum analyzer in parallel with our recording system. In our actual deployment we used a separate antenna, LNA, and spectrum analyzer (not shown in Fig. 2.5) in parallel to independently observe signals and verify proper operation of the recording system and its preselctor.

[2] Use of trade names in this document is solely for the description of the experimental setup and does not constitute endorsement by NIST or CTL. Other instruments may perform as well or better for this application.

software, written in LabVIEW code, ran on the controller, and included user-adjustable settings for the VST reference level, sample rate, file-naming scheme, and threshold level for determining whether or not to save the captured data.

The data sampled by the VST were stored on a pair of 24-TB RAID drives (referred to later as fast RAIDs) connected to the PXIe chassis via PCIe cables. An additional pair of 24-TB RAID drives (referred to later as slow RAIDs) with gigabit Ethernet (GbE) cables were used to store the data for back-up purposes. The PXIe chassis was also connected to an LTE router along with an LTE antenna to enable remote access.

2.2 Statistical considerations

2.2.1 Blind sampling

Our sampling was not coordinated with the Navy; we did not have prior knowledge of the location of the signal source or of the time and frequency of transmission, nor did we obtain ship locations or assigned frequencies during or after the measurements. Thus, our sampling was necessarily blind, and we did not target acquisition of any particular source or time window.

We did not know if emissions observed at different frequencies and/or times were from the same or different shipborne radars. We initially conjectured that, due to the DoD need to coordinate spectrum usage, each frequency observed would correspond to a unique source, and conversely, each source would correspond to a unique frequency. That is, if we acquired SPN-43 signals at two different frequencies, we could be reasonably certain that the signals were emanating from two distinctly different sources. Since our goal was to acquire signals from at least three different sources, we addressed our lack of knowledge by acquiring data until we measured SPN-43 signals at three different frequencies. However, we had no way of knowing if signals observed at a given frequency and time originated from a source whose emission we might also have recorded at a different frequency during our measurement campaign.

Acquisition of signals over uninterrupted 60 s time intervals allowed us to observe unexpected radar behavior that might have otherwise been missed, as described in Sections 3.4 through 3.6.

2.2.2 Relevant variables and potential sampling biases

Controlled experimental variables included the local oscillator frequency used for IQ demodulation, the receiver antenna, receiver noise floor (via the VST's reference level), and the triggering

and data retention criteria (discussed in the next subsection).

Because the measurements were observational in nature, and collected in an uncontrolled environment, there were several uncontrolled experimental variables, including

- Number, locations and movements of shipborne SPN-43 radar transmitters
- Operating frequencies of SPN-43 radars
- Presence of non-SPN-43 RF emitters
- Weather conditions, including atmospheric and sea conditions
- Seaborne scatterers, such as watercraft
- Tropospheric scatter
- Topographical and structural scatterers, such as nearby hillsides and man-made structures.

Some aspects of the RF and weather conditions can potentially be inferred from our measurements. However, knowledge of the other uncontrolled variables, particularly those concerning the SPN-43 radar and ship movements (i.e., location and orientation), was necessarily limited due to the sensitive nature of naval deployments. Consequently, the set of collected measurements likely suffers from sampling biases that are difficult to quantify without additional information. For example, received power is a function of distance and off-axis angle with the cavity-backed spiral antenna, each of which might cause different distortions to the received pulses. High SNR pulses will result from sources that are close and off axis as well as from emitters that are far and on axis.

Additionally, there was an unavoidable selection bias in our measurements due to (1) the limited geographical location and experimental timeframe, and as explained below, (2) the triggering and data retention criteria, and (3) the $10\,\%$ measurement duty cycle. For these reasons, the sample was not likely representative of the entire population of all SPN-43 radar emissions. Unfortunately, characterization of this selection bias is not possible, since it requires access to a larger, comprehensive sample of SPN-43 emissions, which is not available.

2.2.3 Trigger and data retention criteria

A diagram showing our trigger and data retention algorithm is provided in Fig. 2.6. In this section we describe in more detail the trigger criteria and how metadata is generated.

From our VST, we collect in-phase (I) and quadrature (Q) samples at a rate of 225 MSamples/s. We use this sampling rate because it provides an effective 200 MHz bandwith and is also streamable to a fast RAID without dropping samples. In contrast, using a 250 MSamples/s sampling rate provides a flatter 200 MHz bandwidth, but drops samples while streaming to storage. After a data

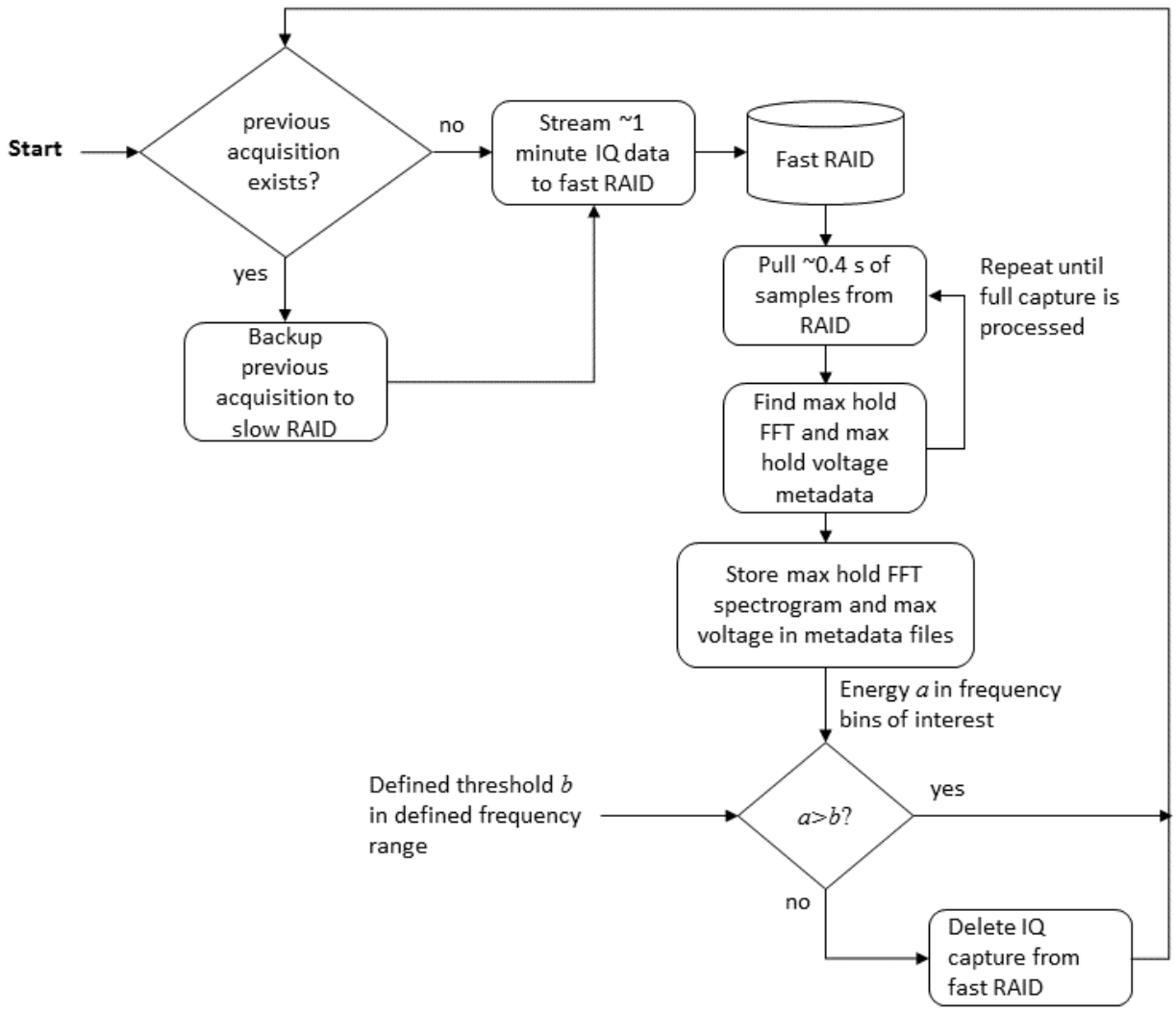

Figure 2.6: Flow chart of acquisition method. After storage of 1 minute of IQ data to the fast RAID, the extraction of metadata requires about 9 minutes of processing, leading to a $10\,\%$ measurement duty cycle.

set is collected to a fast RAID, we have a vector of 16-bit integers that is composed of interleaved Q and I samples. The structure of this vector can be visualized as: $[Q_1\, I_1\, Q_2\, I_2\, Q_3\, I_3\, \cdots\, Q_N\, I_N]$, where N represents the number of samples taken. We de-interleave these values and scale them to double precision to obtain the complex vector $\overrightarrow{IQ}$. This complex vector has the form $\overrightarrow{IQ} = \overrightarrow{I} + i\overrightarrow{Q}$. Specifically, we collect 51 GiB of samples spanning a time period slightly over 60 s. Each complex IQ sample is composed of four bytes before scaling to double precision. To be precise, $\overrightarrow{IQ}$ has a length of $13\,685\,760\,000$ samples.

$\overrightarrow{IQ}$ is large enough that it is costly in terms of time and memory to load and analyze. Our wish to examine this data in a time efficient manner dictates that we generate metadata; descriptions of this data that are less memory intensive. We specifically use a spectrogram and a max-hold amplitude vector as metadata.

To generate metadata, we load sequential subsets of $\overrightarrow{IQ}$ of length 1024×10^5 samples. Let us represent the i^{th} subset of $\overrightarrow{IQ}$ as $\overrightarrow{S_i}, i \in \{1, 2, \ldots, 134\}$. We should note that the last subset, $\overrightarrow{S_{134}}$, is shorter than 1024×10^5 samples due to the total number of samples being a non-integer multiple of 1024×10^5. We also note that 1024×10^5 samples represent about 0.455 seconds of recorded signal. For each $\overrightarrow{S_i}$ we calculate two pieces of information: a scalar A_i, the maximum amplitude of $\overrightarrow{S_i}$, and a vector $\vec{F_i}$, the max-hold spectra of $\overrightarrow{S_i}$. We calculate $\vec{F_i}$ using a short-time Fourier transform and retain the maximum amplitude in each frequency bin. With A_i and $\vec{F_i}$ concatenated over i we obtain a max-hold amplitude vector and a max-hold spectrogram, respectively.

Fig. 3.5 contains an example spectrogram. Each horizontal line (or row) of this plot represents one max-hold spectra. Each vertical trace represents a frequency bin's amplitude through approximately 60 seconds.

After generating metadata, we use a threshold to determine if we wish to retain the raw IQ data or delete it. The threshold compares a subset of the spectrogram with a fixed value.[3] For example, we typically used a portion of the spectrogram corresponding to 3510 MHz to 3660 MHz. If any amplitudes in this portion of the spectrogram exceeded the threshold then we retained the raw data. The reason for deleting data that did not exceed the threshold was to extend the time we could collect data to weeks or months before reaching storage capacity.

The time required to load the data back into the CPU and calculate the metadata is about nine minutes, leading to an acquisition duty cycle of $10\,\%$.

[3] We used a threshold that corresponds to a power of approximately -74 dBm in a frequency bin, referenced to the output of the antenna, indicated as a dotted line in the lower graph of Fig. 3.5 and subsequent spectrograms.

2.3 Measurement calibration

We characterized the individual system components to verify the system gain and gain flatness, and to ensure that the system would be stable with respect to temperature variations that might be encountered with field deployment. We also characterized the system noise and linearity and the gain of our two antennas. Our characterization procedures are described in Sections 2.3.1 through 2.3.7 and the results are summarized and discussed in Section 2.3.8. Detailed response measurements are plotted at the end of the chapter.

2.3.1 RF section magnitude response

We estimated the gain and associated uncertainty for the RF path between the output of the antenna and the input of the VST, which included the following four components: a short cable from the output of the antenna to the input of the pre-selector; the 3.5 GHz path of the pre-selector; a long cable from the output of the pre-selector to the input of the splitter/isolator box; and channel 1 of the splitter/isolator box (see Fig. 2.5).

All of the measurements, except for the short cable, were performed using a metrology-grade vector network analyzer (VNA) corrected with a Type-N open-short-load-thru (OSLT) calibration using the Microwave Uncertainty Framework [10], which allows the physical error mechanisms in the calibration standards to be propagated to the measurements of the components under test, and statistical correlations to be determined between both the scattering parameters at a single frequency and uncertainties at different frequencies. Additionally, these components were measured in an environmental chamber, in an effort to take temperature dependence into account. The short cable was measured on-site using a portable VNA with built-in Type-N OSLT calibration.

The reported measurement values and uncertainties (represented as $95\,\%$ confidence intervals) were determined for the frequency range between 3520 MHz to 3600 MHz. Fig. 2.7 plots the magnitudes of the transmission coefficients (S_{21}) for the pre-selector's 3.5 GHz path as functions of frequency and temperature along with uncertainties. The pre-selector was measured at four distinct temperatures: $11\,^{\circ}\mathrm{C}$, $20\,^{\circ}\mathrm{C}$, $29\,^{\circ}\mathrm{C}$, and $38\,^{\circ}\mathrm{C}$. For the 3520 MHz to 3600 MHz frequency range, the average gain is approximately 29.2 dB with an uncertainty of ± 0.7 dB, which takes into account repeatability, frequency dependence, and temperature dependence.

Figs. 2.8 and 2.9 show the pre-selector's out-of-band rejection at four different temperatures and shows that out-of-band rejection is fairly constant with temperature.

The magnitudes of S_{21} for channel 1 of the splitter/isolator box measured at the same four temperatures is shown in Fig. 2.10. For this frequency range, the average loss is 5.8 dB with an

Component	Gain $\pm$ Uncertainty (dB)
Front-End 3.5 GHz Path	$+29.2 \pm 0.7$
Splitter/Isolator Box Channel 1	-5.8 ± 0.3
Short Cable	-1.0 ± 0.3
Long Cable	-2.6 ± 0.3
Net Gain	$\mathbf{+19.8 \pm 0.9}$

Table 2.1: RF path gain from the output of the antenna to the input of the VST averaged from 3520 to 3600 MHz and averaged over all temperatures.

uncertainty of ± 0.3 dB. Fig. 2.11 plots the magnitudes of S_{21} for the long cable measured at the same four temperatures. The average loss is 2.6 dB with an uncertainty of approximately ± 0.15 dB. The cable manufacturer specifies an uncertainty of $\pm 3.5\,\%$ (or ± 0.3 dB) for this temperature range, so we use this larger value for the cable's uncertainty. Fig. 2.12 plots the magnitudes of S_{21} for the short cable measured with the portable VNA. Since we were not able to perform temperature-dependent measurements on this cable, we chose to apply the same uncertainty of ± 0.3 dB.

Table 2.1 summarizes our average measurements of gain for the four components, along with their respective uncertainties. The table also includes the overall net gain and uncertainty. The overall uncertainty was determined by a root-sum-of-squares calculation, rounded up to the nearest tenth of a decibel.

2.3.2 RF section group delay

We calculated the group delay distortions of a 1 MHz bandwidth pulse for each of the four components using the measured phases of S_{21}. For each component, we unwrapped and de-trended the phase, and then calculated the group delay distortion by taking the second derivative of the phase with respect to frequency and multiplying by the 1 MHz bandwidth. Of the four RF components, the pre-selector had the largest group delay distortion, which ranged between -60 ns and $+60$ ns over the observed frequency range, although it had magnitude of about 17 ns at each of the frequencies where SPN-43 was observed. We can thus expect a positive bias in our estimated pulse duration of ~ 17 ns due to our measurement system.

2.3.3 VST response magnitude

A typical measurement of the VST response magnitude at room temperature is shown in Fig. 2.13. The manufacturer specifies the typical flatness of the VST magnitude response as ± 0.5 dB and the absolute accuracy ± 0.8 dB (95% confidence interval) over a temperature range of $\pm 5\,^{\circ}$C after

running the internal calibration routine. We measured the response of the VST after changing the temperature *without* running the internal calibration routine. For this measurement, we used a VNA with an additional power calibration to deliver a $+5$ dBm sine-wave to the VST input, which was set to the $+5$ dBm reference level. After settling at the temperatures (in order) $25\,^{\circ}$C, $30\,^{\circ}$C, and $20\,^{\circ}$C, the VST measured the sine wave without running the internal calibration routine. This allowed us to test the absolute accuracy of the VST when the temperature had changed by $5\,^{\circ}$C or $10\,^{\circ}$C. Also, the response of the VST is not flat with frequency and ramps up from the local oscillator (LO) frequency f_{LO} at a rate of about 0.01 dB/MHz. The VST was generally found to attenuate the signal by 1.7 dB $\pm$ 0.6 dB, where the 0.6 dB standard uncertainty [11] includes effects of gain drift over a $10\,^{\circ}$C temperature range and the flatness of the response with frequency.

As mentioned above, the sample rate of the ADCs in the VST is 250 MSamples/s. We believe that this rate is fixed and lower sample rates are achieved by interpolation and sub-sampling. Fig. 2.13 shows the out-of-band rejection of the VST anti-aliasing filter. For input signal frequencies less than $f_{N1} = f_{LO} - f_S/2 = 3565 - 112.5 = 3452.5$ MHz, spurious tones occur near f_{N1} and near $f_{LO} + 112.5 = 3677.5$ MHz. For input frequencies between f_{N2} and f_{N1} the later of these tones appear between 3665 MHz and 3677.5 MHz and these are the tones used to calculate the out-of-band rejection. Due to the interpolation and sub-sampling method used in the VST, the exact frequency of all these spurs is a complicated function of both f_{N1} and $f_{N2} = f_{LO} - f_{S,max}/2 = 3565 - 125 = 3440$ MHz and will not be discussed further here.

The net out-of-band rejection of the pre-selector's filter plus the VST's anti-aliasing filter is shown in Fig. 2.14, with approximately 12 dB rejection at 3452.5 MHz and between 50 dB and 60 dB rejection at 3440 MHz.

2.3.4 VST local oscillator and sampling frequencies

The pulse parameters of Chapter 4 depend critically on the frequency accuracy of the VST. While the manufacturer specifies the internal frequency reference accuracy of the VST as $\pm$ Aging $\pm$ Temperature stability $= \pm 2 \times 10^{-6}$ per year, maximum, it is not clear how the LO frequency and sampling rate are affected by the frequency reference accuracy. Therefore, it is important that the LO frequency and sampling rate accuracy be verified. To do this we used a VNA whose 10 MHz reference was tied to one of the NIST Hydrogen masers as a signal source [12]. The VST LO frequency was set to 3565 MHz and we measured records of 1 ms or longer with input signal frequencies greater than and less than 3565 MHz. For measured data at each frequency, we performed an FFT on the time record and made note of the calculated peak signal frequency. We also used an adaptive algorithm to estimate the signal frequency with sub FFT-bin resolution. We expect that measured frequency errors would have the same sign if the LO frequency were in error, while the measured frequency grid would be stretched or contracted if the sampling rate were in error. A

combination of these effects would result in an error verses offset from the LO frequency having some mean offset and trend. The measurements showed a general offset but no significant trend, indicating that the LO frequency error dominates. The mean LO frequency was found to be in error by $+3.06 \pm 0.17$ kHz (from the mean and standard deviation of eight measurements symmetrically distributed around the LO frequency), or slightly less than the manufacturer's specified 1 part in 10^6 accuracy.

2.3.5 Antenna characterization

We attempted a spot characterization of each of our antennas: a 45° (linear) slant polarization omni-directional antenna and a cavity-backed spiral antenna. However, it should be noted that we cannot compensate for the antenna gain or antenna pattern in our measurements because we do not know the position of the emitters or the path that the signals take between the emitter and our measurement system. The analysis of subsequent chapters is referenced to a calibration plane at the coaxial output of the antenna. The antenna characterization performed here is used to fully specify the measurement system.

The antennas were characterized in a 10.4 m $\times$ 5.6 m $\times$ 4.1 m anechoic chamber (from cone tip to cone tip) by use of a conical spiral reference antenna positioned 3 m from antenna under test. The gain of the reference antenna was measured by the manufacturer and we estimate that it was characterized with uncertainty $U_{\text{ref}} = 1$ dB.

The mean gain of the omni-directional antenna, variation in gain with azimuth, gain standard uncertainty, and gain expanded uncertainty at the $68\,\%$ confidence level are given in Table 2.2.

To measure the horizontal gain and azimuthal dependence of the omni-directional antenna, it and the reference antenna were mounted $\sim$ 2.3 m from the floor of the anechoic chamber. Measurements were taken at the cardinal directions of 0°, 90°, 180°, 270°, and 360°, where measurements at 0° and 360° can be used to characterize the positioning repeatability of the measurements.

We estimate the positioning repeatability uncertainty U_r with one degree of freedom as

$$U_r = \sqrt{\left(\overline{G(0^\circ)} - G(0^\circ)\right)^2 + \left(\overline{G(0^\circ)} - G(360^\circ)\right)^2} \tag{2.1}$$

where,

$$\overline{G(0^\circ)} = \frac{1}{2}\left(G(0^\circ) + G(360^\circ)\right). \tag{2.2}$$

We use the mean gain $\overline{G}$ and the standard deviation S_G of the gain $G(\phi_i)$ over all azimuthal angles $\phi = (0^\circ, 90^\circ, 180^\circ, 270^\circ)$, where $G(0^\circ) = \overline{G(0^\circ)}$, to quantify the gain and gain uniformity

Frequency (MHz)	$\overline{G}$ (dBi)	U_r (dBi)	S_G (dBi)	U_G (dBi)	$U_G k_{0.68}$ (dBi)
3520	-0.7	1.1	1.5	2.1	2.2
3550	-0.1	1.0	1.3	1.9	2.0
3600	0.9	0.8	0.7	1.4	1.6

Table 2.2: Estimated gain of omni-directional antenna in the horizontal plane, averaged over cardinal directions, with uncertainty at three frequencies. Variables are defined in the text.

of the antenna. S_G is found with three degrees of freedom.

The standard uncertainty of the gain, which quantifies the uncertainty in the gain experienced when measuring any particular signal, is found by adding the uncertainties in quadrature:

$$U_G = \sqrt{U_r^2 + S_G^2 + U_{\text{ref}}^2} \tag{2.3}$$

Since we have a limited number of measurements, we next find the expanded uncertainty for a $p = 0.68$ confidence interval. First we find the effective number of degrees of freedom ν_{eff} by use of the Welch-Satterthwaite equation [11]

$$\nu_{\text{eff}} = \frac{U_G^4}{S_G^4/3 + U_r^4}, \tag{2.4}$$

and then find $k_p = t_p(\nu_{\text{eff}})$, where $t_p(\nu_{\text{eff}})$ is the t-distribution, for degrees of freedom ν_{eff}, that defines an interval $-t_p(\nu_{\text{eff}})$ to $+t_p(\nu_{\text{eff}})$ that encompasses the fraction p of the distribution. Here we have assumed that the degrees of freedom of the reference antenna gain is a large number. Note that ν_{eff} is a function of the relative contributions of the different uncertainty components and is therefore not fixed with frequency, varying here between 10 and 23.

Our observed gain agrees well with the manufacturer's characterization of the antenna. However, the manufacturer indicates maximum gain roughly at 60° above the horizon and roughly 5 dB to 7 dB higher than at the horizon.

The omni-directional antenna is specified as a "slant polarization" antenna by the manufacturer, and has maximum input coupling when the incident signal is linearly polarized at 45° to horizontal. Horizontally polarized and circularly polarized signals will experience 3 dB loss.

The CBS antenna is right-hand circular polarized and we expect 3 dB coupling loss into the antenna when the SPN-43 is linearly polarized and tens of dB coupling loss when the SPN-43 is left-hand circularly polarized.

To measure the CBS antenna gain, the antenna was mounted on a polyvinyl chloride (PVC)

Frequency (MHz)	Boresight gain (dBi)	Uncertainty (dBi)
3520	6.1	1
3550	6.4	1
3600	6.9	1

Table 2.3: Boresight gain of CBS antenna at three frequencies with estimated uncertainty. Note that uncertainties at off axis angles may be greater

Reference level (dBm)	Noise equivalent power (dBm/Hz)
5	−155.6
−10	−165.6
−20	−167.7
−30	−168.6

Table 2.4: System noise equivalent power, referenced to the antenna output for various VST reference level settings. The measurements analyzed, qualitatively or quantitatively, in this document were conducted at a reference level of 5 dBm unless otherwise noted.

pipe, which in turn was mounted on a kinematic mount capable of rotation in 15° increments. The CBS antenna pattern, measured in 15° increments, is shown in Fig. 2.15 and boresight gain is given in Table 2.3. Here the dominant contributions to the uncertainty in the boresight gain are the reference antenna gain and the orientation error.

2.3.6 System noise floor

The system noise floor was measured in the field by connecting a $50\ \Omega$ coaxial termination at the end of the short cable where the antenna would normally be located, acquiring a 60 s temporal record, and then calculating the metadata. The system noise floor, referenced to the short cable input, was then calculated based on spectrograms (see Section 3.2 for more information) and verified with the full IQ waveform files. The measured noise equivalent power, referenced to the antenna output is given in Table 2.4.

2.3.7 System nonlinearity

System linearity was a major consideration in both the design of the system and analysis of the measurement data. The pre-selector uses an LNA whose -1 dB compression point is 27.9 dBm. The VST was typically run with the reference level at 5 dBm or lower, meaning that the VST would saturate at much lower power than the LNA.

The VST uses ADCs with 14-bit resolution. The spur-free dynamic range (SFDR) of the VST was calculated, when characterizing its gain, and was shown to be typically between 65 dB and 70 dB with a sinusoidal input signal and power equal to the reference level.

The max-hold metadata A_i (in the time domain) and $\vec{F}_i$ (in the frequency domain) were used for checking for VST saturation *post facto*. Peak voltages A_i were confirmed to be lower than the reference level, e.g., see Fig. 4.1. Files containing spurs that might have been caused by receiver nonlinearity were rejected from analysis, as described in the Appendix.

2.3.8 Summary and discussion of system gain and uncertainty

The component gain measurements described in sections 2.3.1 through 2.3.7 are summarized in Table 2.5. As described previously in Sections 2.3.1 and 2.3.3 we measured the temperature dependence of the RF section and VST gains, and temperature was certainly a significant contribution to the uncertainties in the gain of those components. Table 2.6 gives statistics of the temperature observed outside the measurement tower, where the pre-selector was, and inside the tower, where the VST was. Temperature measurements were recorded asynchronously from the beginning of system deployment till the end of campaign ~ 2 months later. Both temperatures were relatively stable, as characterized by the standard deviation. Temperature excursions (to low temperatures) inside the tower were due to opening the tower door and removing protective covering over the equipment during a few days at the beginning and the middle of the campaign, when the system was being assembled or modified. Stability of the internal VST temperature, measured on a third temperature sensor inside the VST, confirms temperature stability of the environment in which the VST was placed. Based on this line of reasoning, the uncertainties for the RF section and VST gain may actually be conservatively high.

While we believe that we are able to characterize the RF section and VST gain, we cannot say the same with the antennas because of the unknown paths of propagation from the source to the measurement antenna and the angle of arrival in both azimuth and elevation. The paths involved include direct line-of-sight propagation, as well as reflections from nearby objects and atmospheric scattering. For the omni-directional antenna, elevation angle could cause as much as 5 dB to 7 dB variation, while azimuthal variation could cause roughly 2 dB variation (see Table 2.2). For the CBS antenna, given the approximately 180° field of view at the measurement site, variation in azimuthal direction of arrival could cause as much as 19 dB variation.

In conclusion, antenna pattern effects potentially dominate our measurement uncertainties and could severely distort incoming signals, particularly in the case of multiple signal paths with significantly different angles of incidence. However, if we assume that the antennas used in an ESC system are similar to the ones used in our measurements, signals measured by ESCs would be

Component	Gain $\pm$ Uncertainty (dB)
RF section	$+19.8 \pm 0.9$
VST	-1.7 ± 0.6
Omni-directional antenna	$(-0.7$ to $0.9) \pm (2.2$ to $1.5)$
CBS antenna (on boresight)	$(6.1$ to $6.9) \pm 1$

Table 2.5: Summary of component gains. See discussion of uncertainties due to angle of arrival in Section 2.3.8.

Outside temperature	°C
Mean	16.2
Max.	25.2
Min.	12.2
Std. dev.	1.8
Inside temperature	**°C**
Mean	36.2
Max.	40.4
Min.	21.2
Std. dev.	2.3

Table 2.6: Summary of temperature statistics at tower during measurement campaign.

similarly distorted. Therefore, we believe that our measured signals are still representative of those that ESCs would need to detect.

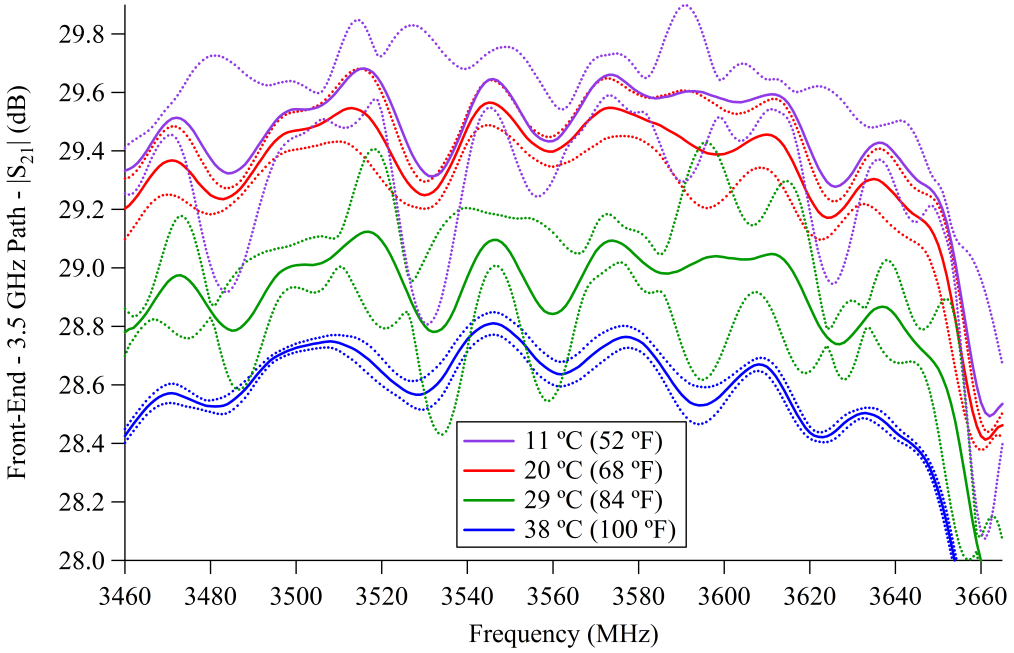

Figure 2.7: Transmission measurements of the pre-selector's 3.5 GHz path as functions of frequency and temperature along with uncertainties.

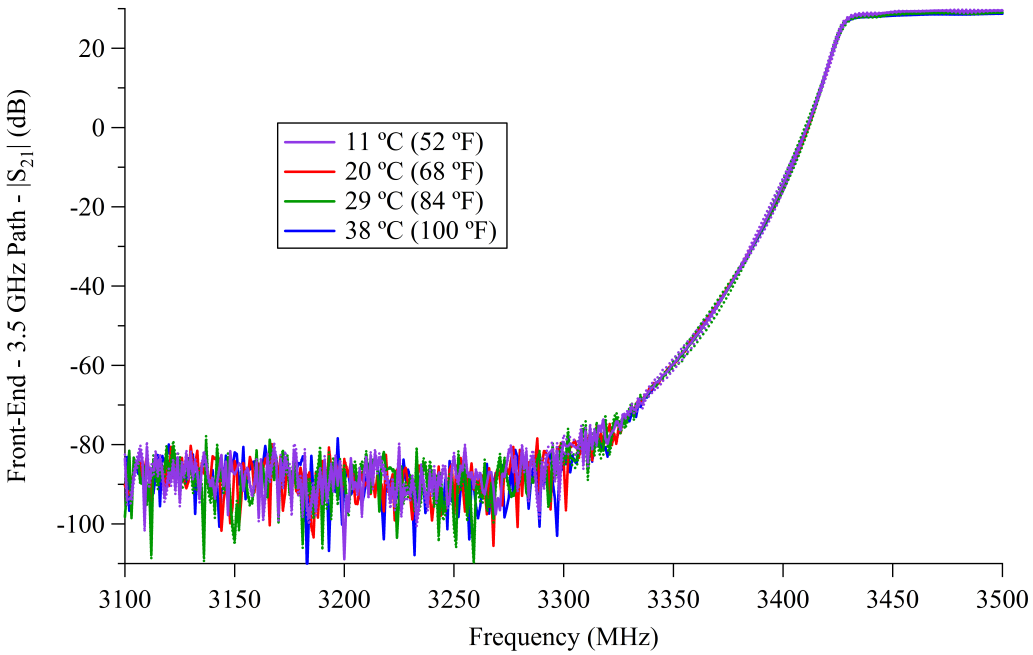

Figure 2.8: Transmission measurements of the pre-selector's 3.5 GHz path low frequency rejection as functions of frequency and temperature along with uncertainties.

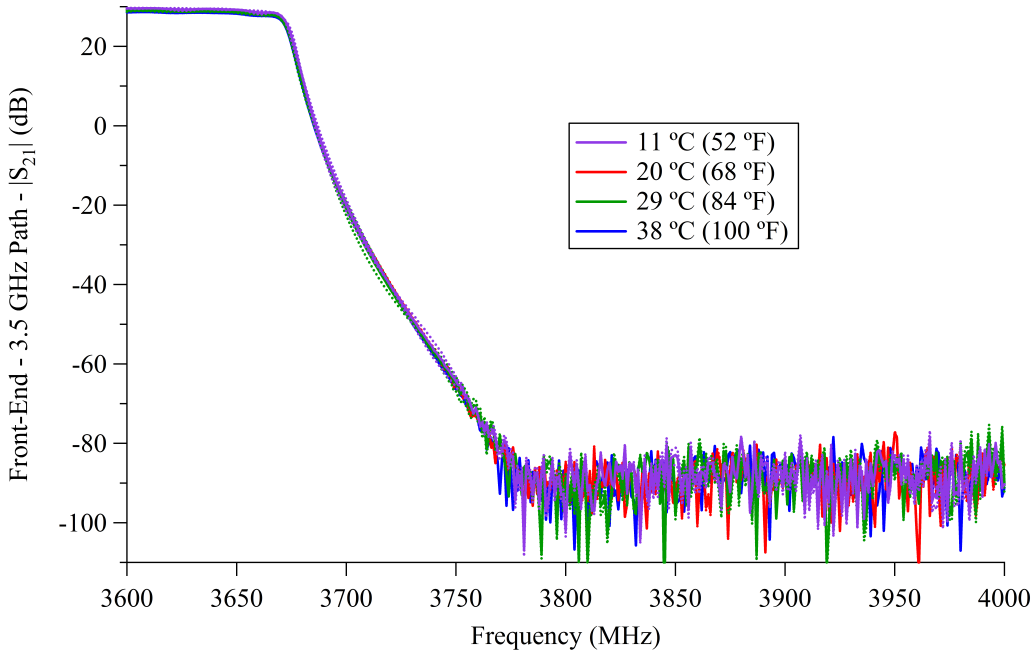

Figure 2.9: Transmission measurements of the pre-selector's 3.5 GHz path high frequency rejection as functions of frequency and temperature along with uncertainties.

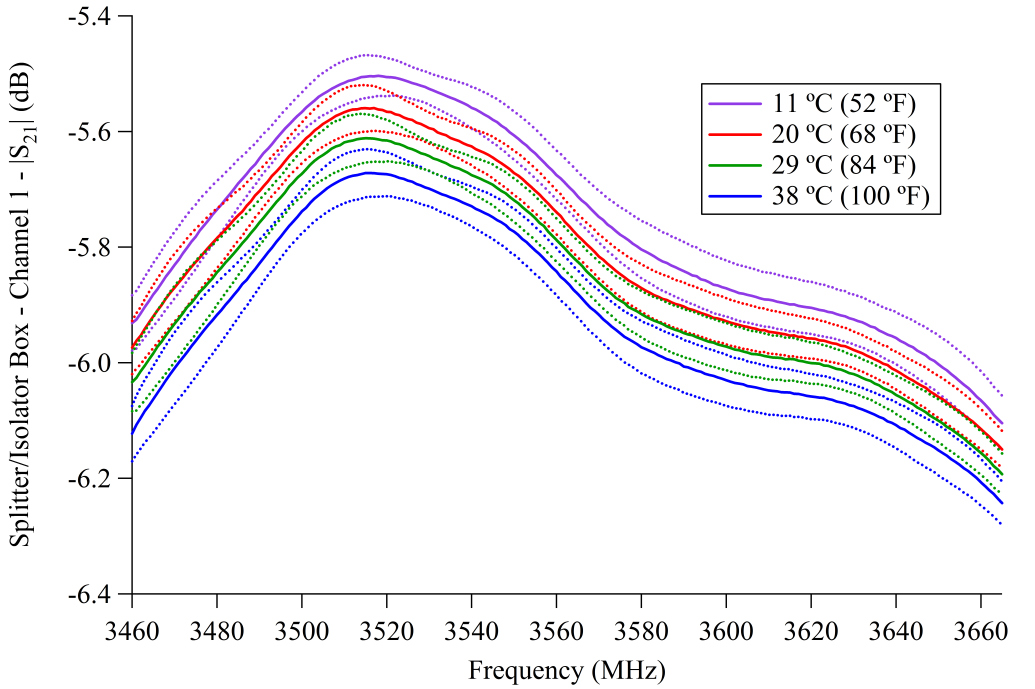

Figure 2.10: Transmission measurements of channel 1 of the splitter/isolator box as functions of frequency and temperature along with uncertainties.

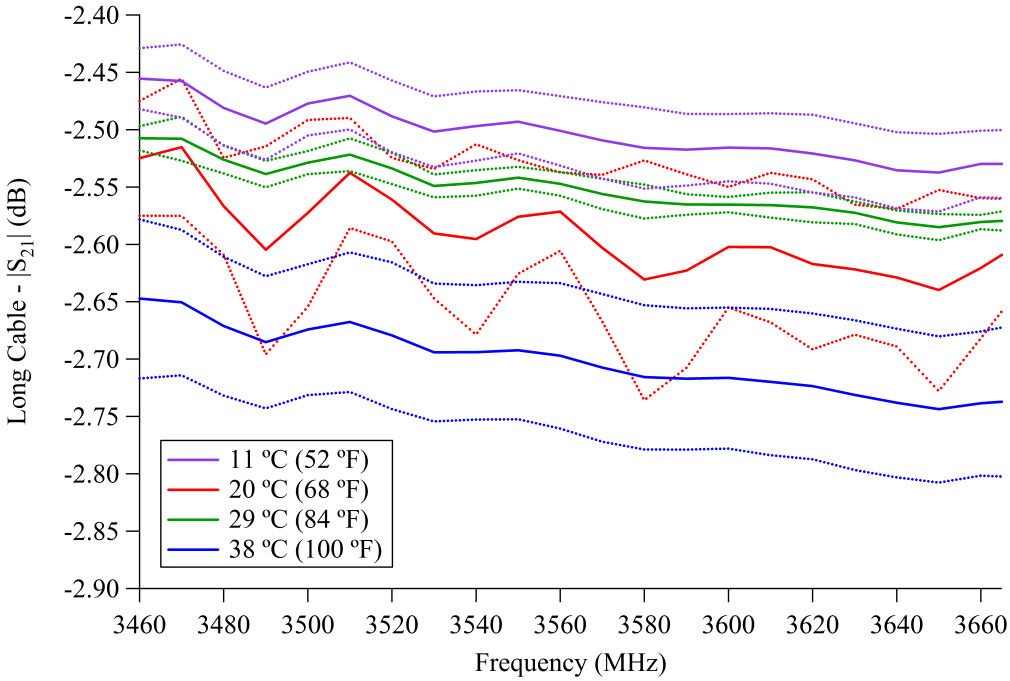

Figure 2.11: Transmission measurements of the long cable as functions of frequency and temperature along with uncertainties.

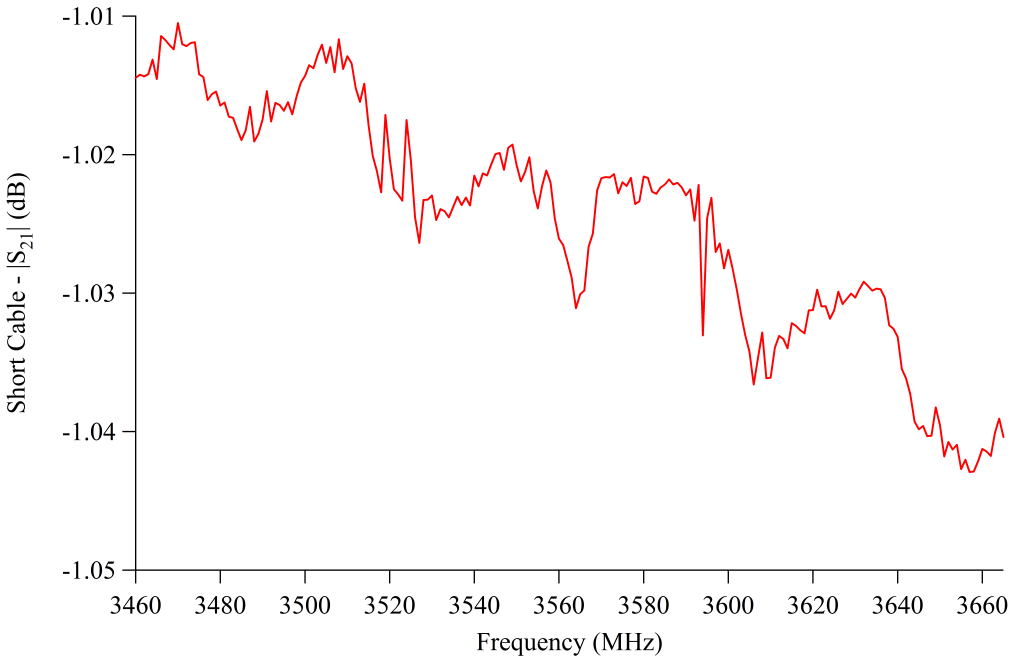

Figure 2.12: Transmission measurements of the short cable as a function of frequency.

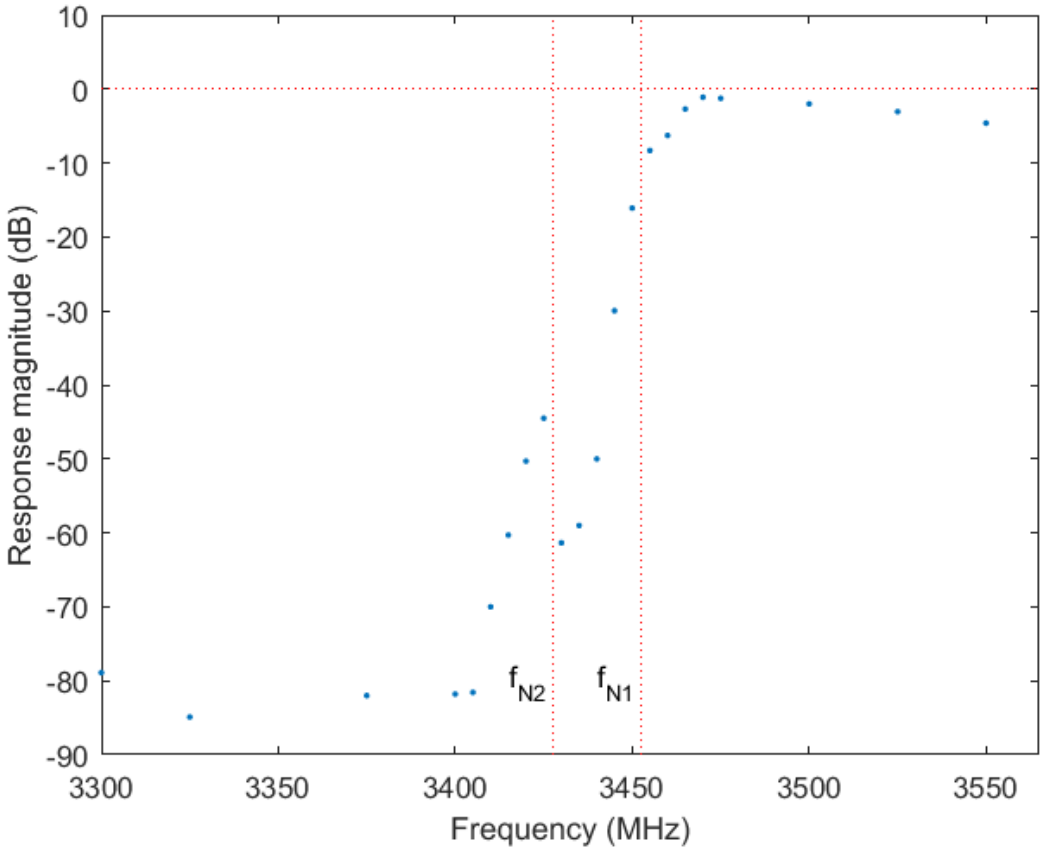

Figure 2.13: Normalized response of the VST measured at room temperature and at select input frequencies below the LO frequency $f_{LO} = 3565$ MHz. The VST reference level and the input power were $+5$ dBm. Frequencies f_{N2} and f_{N1} refer to the Nyquist frequency due to the VST 250 MSample/s sample rate and the re-sampling rate of 225 MSample/s, respectively. For input frequencies below f_{N1} the response is measured at the frequency of the spur appearing above f_{LO}.

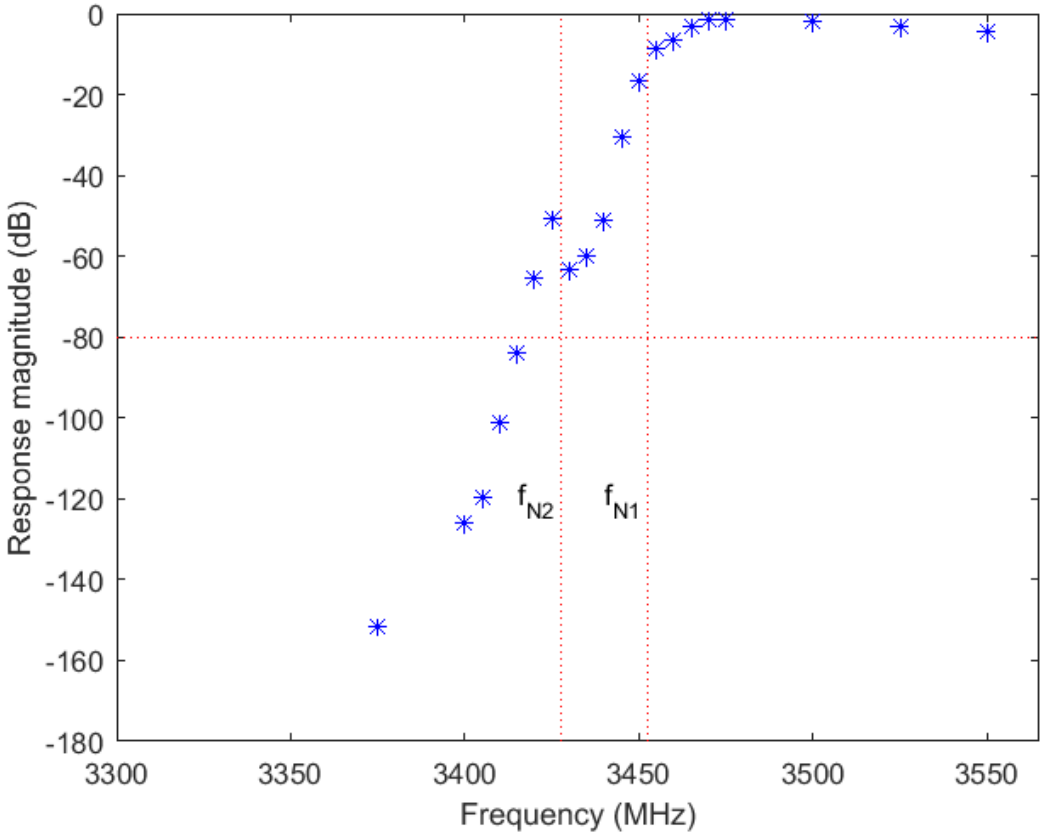

Figure 2.14: Normalized out-of-band gain of pre-selector plus VST measured at room temperature and at select input frequencies below the LO frequency $f_{LO} = 3565$ MHz. Rejection is calculated by summing the room temperature (interpolated) curves in Figs. 2.8 and 2.13, then normalizing to the maximum in-band transmission gain. Horizontal line at -80 dB denotes noise floor of VST.

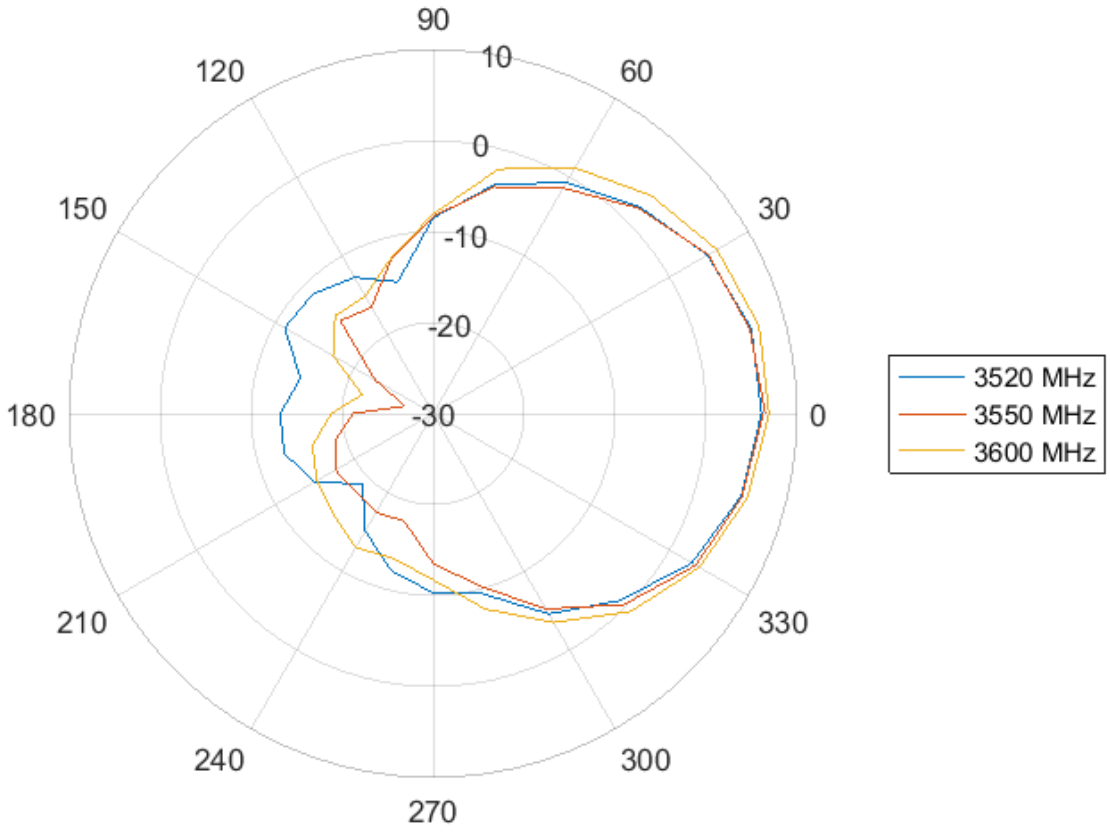

Figure 2.15: CBS antenna gain (dBi) vs. azimuth angle (degrees) at three frequencies. Boresight gain is given in Table 2.3. The -3 dB beam width is roughly 60° at all frequencies and the ratio of front to back gain is at least 17 dB.

Chapter 3

Qualitative Results

Although the library of high quality IQ waveform data is the key outcome of this work, the spectrogram metadata used for triggering the data acquisition and for diagnostics is also useful for analyzing the qualitative behavior of the signals. In particular, observation of specific events can serve as counter examples to conjectures on how the DoD uses the spectrum. In this chapter we start with an overview of typical SPN-43 waveforms and spectrograms during what could be called normal operation. We then show a few examples of SPN-43 signals that we call anomalous, disproving a few of our initial assumptions. We conclude the chapter with a discussion of observed spectrograms of signals that could interfere with CBRS or ESC operation.

3.1 Overview of SPN-43 waveforms

Previous to the current work, public information regarding SPN-43 was limited to the standard SPN-43 radar specifications from 1973 [3], which are summarized in [4]. More current specifications are available in [5] and are summarized in Table 1.1. A limited number of measurements were reported in [4] and [7]. In Chapter 4 we give detailed statistics of our measured antenna rotation period, pulse repetition interval, pulse duration, and frequency offset.

The magnitude of a typical IQ waveform from the Point Loma measurement campaign is shown in Fig. 3.1, where the radar dish rotation is clearly shown as a high peak-power burst of pulses roughly every 4 s. Significant structure is also observed between these rotations. This structure may be due to back-lobes of the radar antenna or reflections from neighboring objects, such as ships or mountains. Some of the structure close to the main beam of radar is shown in Fig. 3.2. This structure is seen to change with every capture and even within the captures. Further details can be observed by looking at the waveform in finer detail. Fig. 3.3 shows the main lobe of the

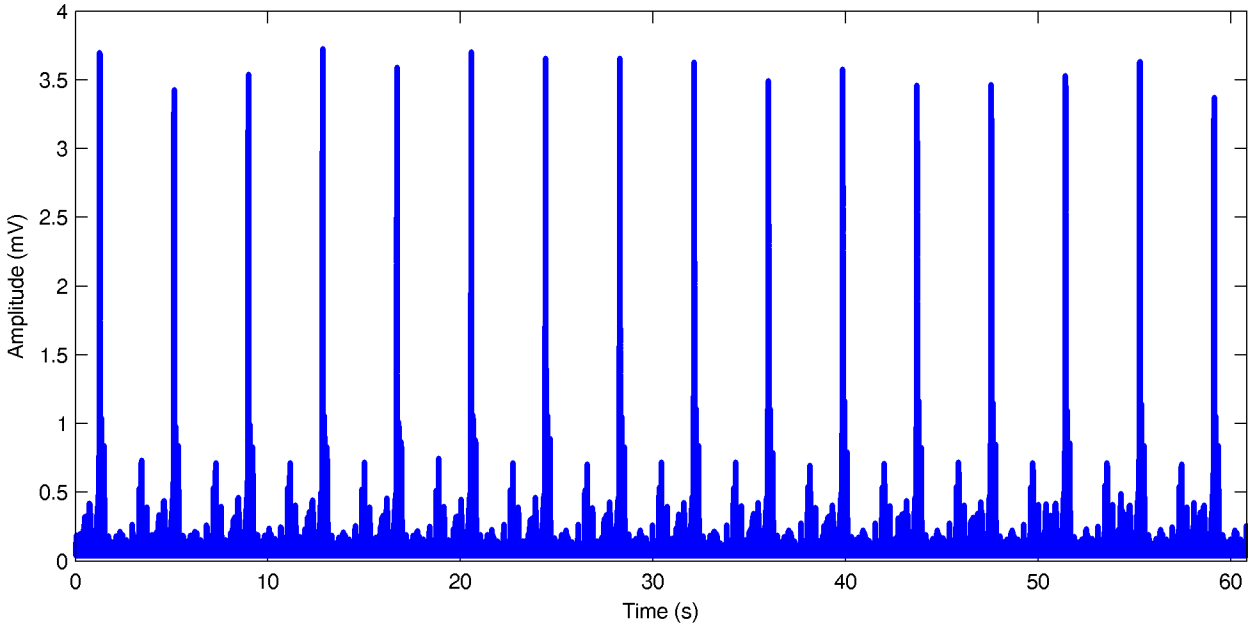

Figure 3.1: Magnitude of an IQ capture of a typical 3550 MHz SPN-43 radar. The full capture epoch of just over 60 s duration is shown here. The next three figures show details of the radar antenna sweep near 28 s with increasingly finer temporal resolution.

sweep made up of periodic pulses with period 1 ms, and Fig. 3.4 shows the envelope of one such pulse which has a duration of approximately 1 μs.

3.2 Spectrograms and their projections onto the time and frequency axes

In this section, we further describe the spectrograms that will be used extensively for the remainder of this chapter and the projection of these spectrograms onto the time- and frequency-axes. Fig. 3.5 shows a spectrogram of a signal measured, by use of the omni-direction antenna, when little or no radar signals are present. A plot of time vs. power, aggregated over all frequencies is shown at left. This aggregation is found by finding the maximum frequency bin for each time slot. We refer to this plot as the frequency-aggregated spectrogram. Similarly, a plot of power vs. frequency, aggregated over all time is shown at bottom. We refer to this plot as the time-aggregated spectrogram.

Two scales are shown on the time-aggregated spectrogram: maximum power on the left and noise equivalent power (NEP) on the right. The maximum power is referenced to the output of the antenna. It is computed by converting the peak-hold frequency-domain amplitude in volts to power in decibels (assuming $50\,\Omega$ impedance) referenced to one milliwatt (dBm), subtracting the

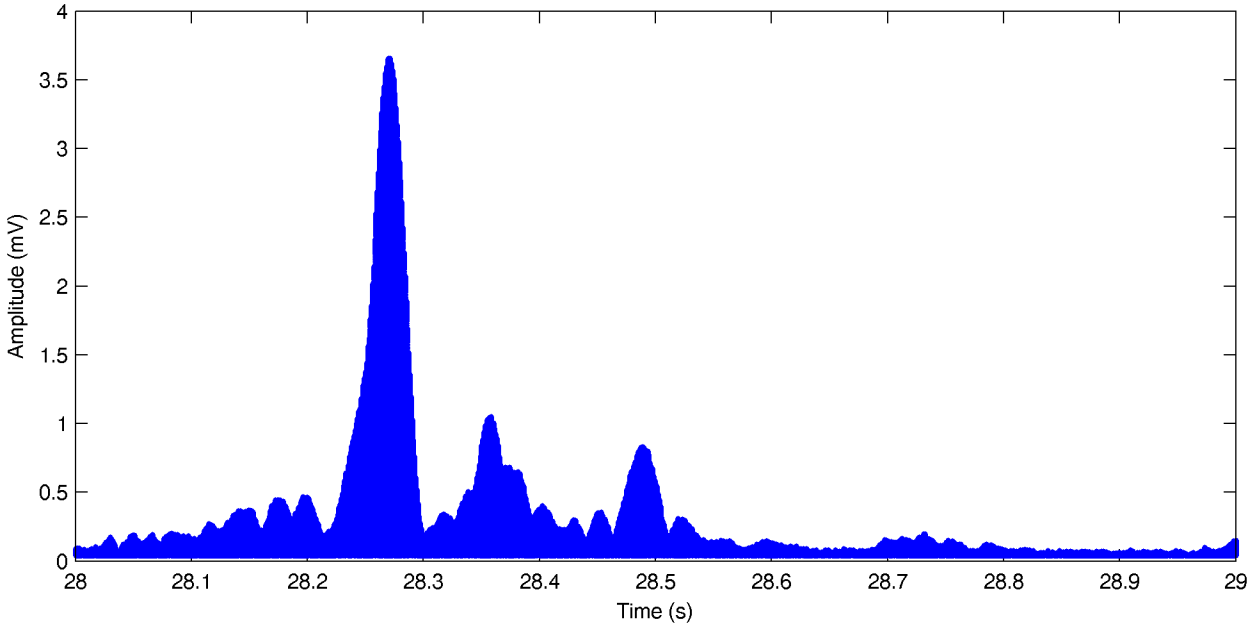

Figure 3.2: A 1 s duration sub-epoch of the SPN-43 radar capture of Fig. 3.1 showing detail in the time interval in which the main radar beam passes over the measurement system antenna.

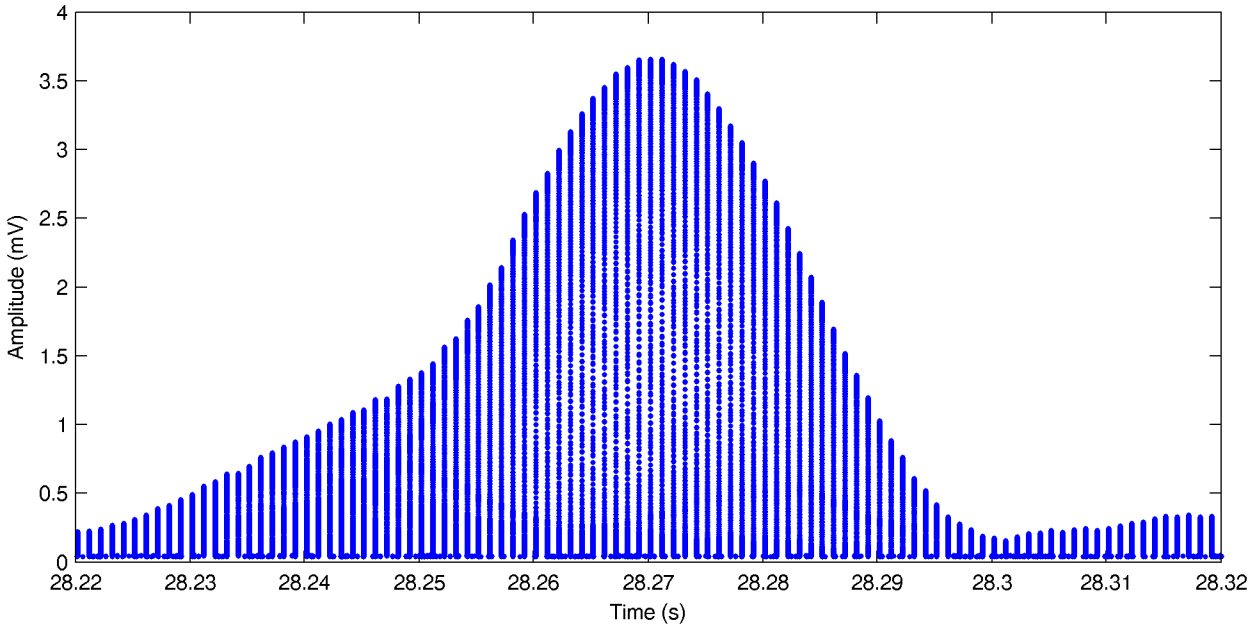

Figure 3.3: A 100 ms duration sub-epoch of the SPN-43 radar capture of Fig. 3.1 showing detail in the time interval in which the main radar beam passes over the measurement system antenna. Here individual pulses are resolved.

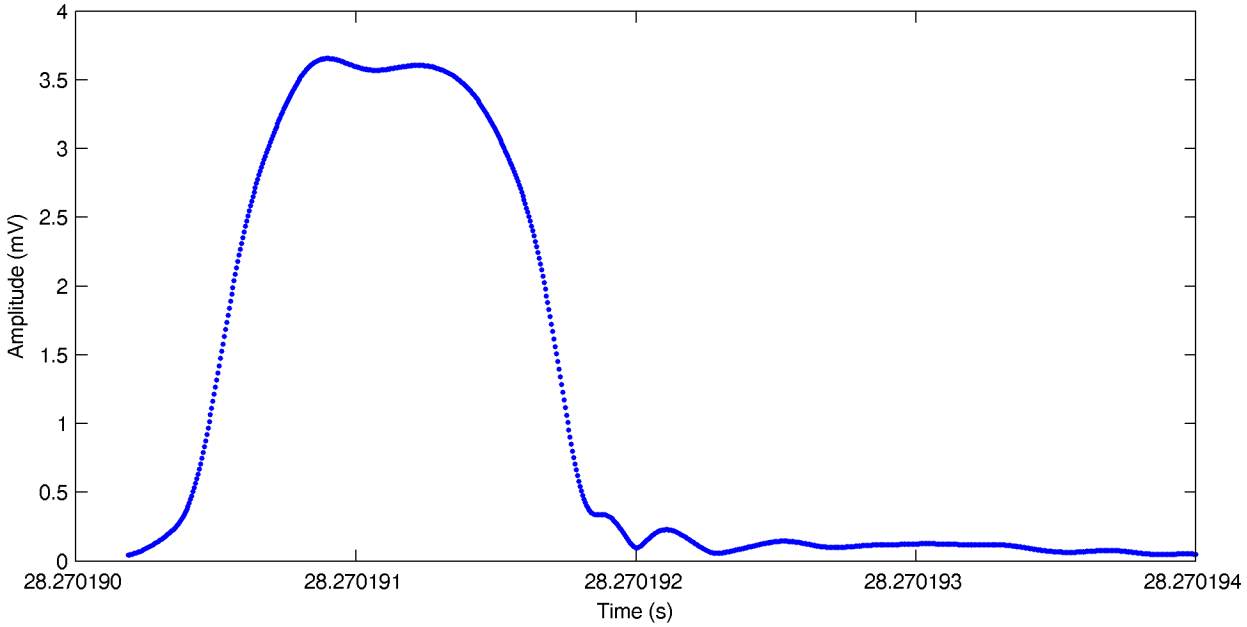

Figure 3.4: A 4 μs duration sub-epoch of the SPN-43 radar capture of Fig. 3.1 showing detail in the time interval in which the main radar beam passes over the measurement system antenna. Here detail in an individual pulse is clearly resolved.

RF path gain from the output of the antenna to the input of the VST, and adding a VST calibration factor of 1.7 dB.

The NEP is the power spectral density (dBm/Hz) one would measure if the input signal was additive white Gaussian noise. We calculate the NEP because this is the scale commonly used by analog spectrum analyzers and can be used to quantify the sensitivity of our measurement system. It is computed by converting the peak-hold frequency-domain amplitude in volts to power in decibels referenced to one milliwatt (dBm), subtracting the RF path gain from the output of the antenna to the input of the VST, adding the 1.7 dB VST calibration factor, converting from peak power over the 0.455 s epoch to average power,[1] and subtracting the effective noise bandwidth of the time-domain window used in computing the discrete Fourier transform (53.8 dBHz).

The noise at frequencies below 3465 MHz and above 3650 MHz falls due to the anti-aliasing filter inside the VST. The anti-aliasing filter plus the pre-selector proved to be effective in eliminating signal images due to aliased out of band signals, except when those signals were quite large. In these cases (e.g., Fig. 3.16) it is visually clear when there is an image present above ~ 3665 MHz due to strong signals present below 3452.5 MHz .

The peak in Fig. 3.5 at 3565 MHz for all times is present because of the direct downconversion

[1]The ratio of the peak to average power, assuming additive white Gaussian noise and where the peak is obtained over 1.28×10^5 independent complex Gaussian envelope samples, is approximately 10.9 dB.

architecture of our VST. It is due to LO energy leaking between the LO port and the IF port of the mixers used for IQ demodulation. For display purposes, the actual LO tone, which is typically about 10 dB higher than the surrounding pedestal, has been suppressed by setting its power equal to the average of the powers in the FFT bins on either side of the LO tone. The region between 3525 MHz and 3535 MHz with slightly higher power than the noise background is what we believe to be a WiMAX signal. This signal can be observed in most of the measurements acquired during the measurement campaign.

3.3 Qualitative behavior of SPN-43 in normal operation

The spectrogram of Fig. 3.6 shows typical behavior of a SPN-43 radar, as expected from [3], with a slightly smaller antenna rotation period of approximately 3.8 s. The pulses display a shoulder towards lower frequency, as is commonly observed with conventional magnetron radar sources [13, 14]. The region between rotations, which is nominally in the antenna back lobes, exhibits power levels that are at least 10 dB above our receiver's noise floor, and in this case includes one prominent peak. Possible explanations for the structure between rotations include reflections from the ship's superstructure, reflections from large nearby objects, such as large ships, reflections from geographic features near the receiver, and back lobes of the antenna itself. The structure of the measured between-rotation signals evolves with time in all of our measured spectrograms. In this case, the peak sweep powers vary slowly and by about 0.7 dB.

The spectrogram of Fig. 3.7 displays roughly symmetric shoulders. Note that if the low-frequency shoulder of Fig. 3.6 were present in this measurement it would be 25 dB above the measurement noise floor and clearly visible. It was shown in [15] that the spectrum of a magnetron or coaxial magnetron generated pulses can be modified by changing the pulse driver circuit, giving one possible explanation for the differences in spectral shape.

The spectrogram of Fig. 3.8 shows the received radar signal undergoing 31.5 dB of fading, while the other captures shown are relatively constant. Thus, ESC detectors may need to be robust against a range of fading channels.

3.4 Observed SPN-43 anomalous behavior

We expected the SPN-43 to operate at a single frequency so as to not interfere with other users of the spectrum that have a fixed spectrum allocation [16]. Fig. 3.9 shows a counter example where the frequency of a SPN-43 is being tuned in frequency at a constant rate between the beginning of the spectrogram and about 55 s, at which time the tuning reverses.

In Fig. 3.10 we see the radar turning on, accompanied by frequency and rotation period instabilities. Frequency changes at the beginning of detected emission may be due to intentional tuning or to instability in the radar system just after being turned on. Rotation period changes may be due to the radar rotation startup and proceeding to the quiescent rotation rate over the course of 20 s to 30 s.

3.5 Two SPN-43 operating in the same frequency band

We would expect that in a given area, SPN-43 radars would be assigned different frequencies so as to not conflict with each other [16]. Here we present evidence indicating that two SPN-43 radars within detectable range may have been operating at the same nominal frequency over the course of a few hours.

Fig. 3.11 shows a spectrogram of SPN-43 signals at 3520 MHz and 3550 MHz. The signal at 3520 MHz had been visible for about one day previous to this capture and the signal at 3550.72 ± 0.22 MHz had been present for about 30 minutes.[2] Ten minutes later, the spectrogram in Fig. 3.12 was captured. Here we see the 3550 MHz signal still at about the same weak power level. The signal at 3520 MHz had been turned off some time between the two captures and is being restarted and the frequency is changing. Ten minutes after this capture, the spectrogram of Fig. 3.13 was captured. In this spectrogram we see a train of peaks separated by about 3.8 s with comparable power to the 3520 MHz signal in the previous figure but at frequency 3550.06 ± 0.22 MHz. We also see faint peaks spaced by about 3.8 s at 3550.50 ± 0.22 MHz. In Fig. 3.14, recorded 2.5 hours later, we see similar interleaved peaks at center frequencies 3549.84 ± 0.22 MHz and 3550.50 ± 0.22 MHz, where the higher frequency source has increased in power.

3.6 Other signals observed in the 3550 MHz to 3650 MHz band

3.6.1 Adjacent-band emitters

It was concluded in [7] that adjacent-band radar, in particular the Radar 3 of [9], could generate significant emissions into the 3.5 GHz band, as shown in Fig. 3.15. In that figure, the emissions into the 3550 MHz to 3650 MHz band can be roughly 50 dB below the power emitted into the primary 3100 MHz to 3500 MHz band. We confirmed this conclusion in numerous measurements, e.g., Fig. 3.16, where the power in the 3550 MHz to 3650 MHz band is 15 dB to 20 dB above

[2] The frequency resolution of the spectrogram is $225\ \mathrm{MHz}/1024 \approx 220\ \mathrm{kHz}$.

the system noise floor and less than 50 dB lower in power than the signal in the $\sim$ 3460 MHz to 3500 MHz band. Although the observable band of our recording equipment was limited to 3455 MHz to 3655 MHz, we were able to observe spectra over the entire 3 GHz to 4 GHz band with similar characteristics to those reported in [7] by use of a separate observation system[3] and verify concurrent signals in the 3100 MHz to 3500 MHz band and broadband signals in the 3.5 GHz band. Furthermore, ships carrying Radar 3 were commonly observed visually during and in the vicinity of our measurements. We therefore conclude that the broadband signals observed in the 3550 MHz to 3650 MHz band are indeed emanating from Radar 3.

Broadband emissions from Radar 3 were often observed during the measurement campaign, examples of which are shown in Figs. 3.17 and 3.18. In Fig. 3.18, a SPN-43 at 3550 MHz is clearly visible during the first 30 s of the spectrogram, but (assuming it did not turn off) is obscured at times later than 30 s, showing that Radar 3 emissions into the 3.5 GHz band could confound SPN-43 detection. In Fig. 3.19 we see that Radar 3 can also operate in a pulsed mode that might make ESCs that are looking for pulsed emitters give a false detection.

3.6.2 In-band emitters

As shown in Fig. 3.5, and several other figures in this chapter, measurements with the omni-directional antenna revealed a WiMax-like signal between 3525 MHz and 3435 MHz

Measurements with the VST reference level reduced from $+5$ dBm to -30 dBm have a lower noise floor, as previously detailed in Table 2.4. Measurements with the lower noise floor and the omni-directional antenna revealed other weak WiMax-like signals, shown in Fig. 3.20 between 3475 MHz and 3485 MHz, 3540 MHz and 3545 MHz, and 3568 MHz and 3573 MHz. The source of these signals is unknown.

Measurements with the higher directionality and gain of the CBS antenna, and the pre-selection filter removed from the RF path revealed a low-power in-band source operating between 3609 MHz and 3704 MHz, as shown in Figs. 3.21 and 3.22. This signal hops in frequency roughly every 2.7 s (note that the spectrogram resolution is 0.455 s), and its source is unknown.

[3] Consisting of an antenna, LNA, and analog spectrum analyzer.

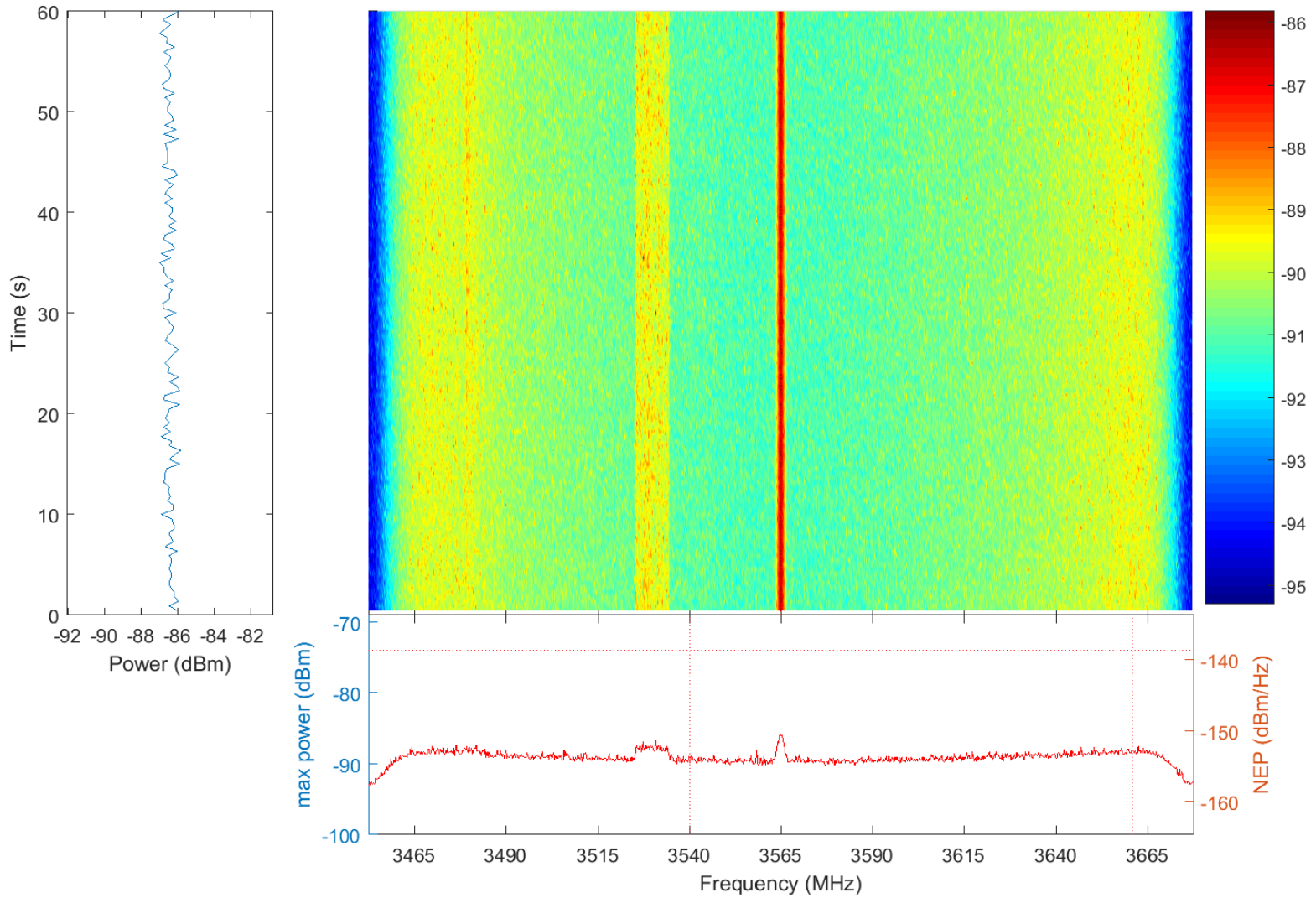

Figure 3.5: Spectrogram (colored surface plot) assembled from spectral metadata, along with the frequency-aggregated signal plotted on the left and the time-aggregated signal below. Units for the time-aggregated signal plot are described in the text.

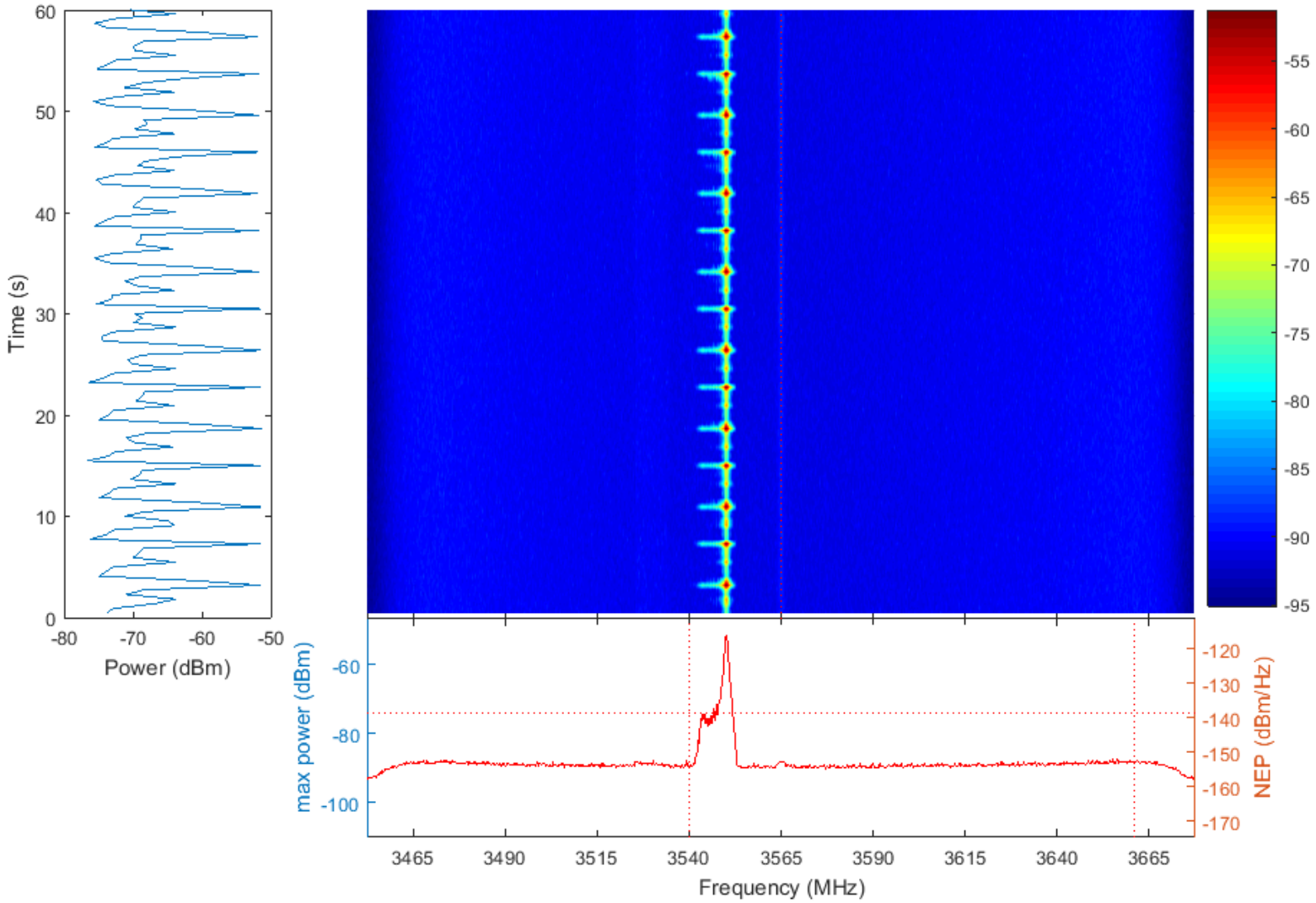

Figure 3.6: Spectrogram of a SPN-43 signal, centered near 3550 MHz, and captured with the omni-directional antenna. Frequency-domain pedestal on lower frequency side of peak is clearly visible. The mean peak power pooled over all rotations in this 60 s capture is -51.6 dBm in a frequency bin, referenced to the antenna output, with a spread of 0.7 dB.

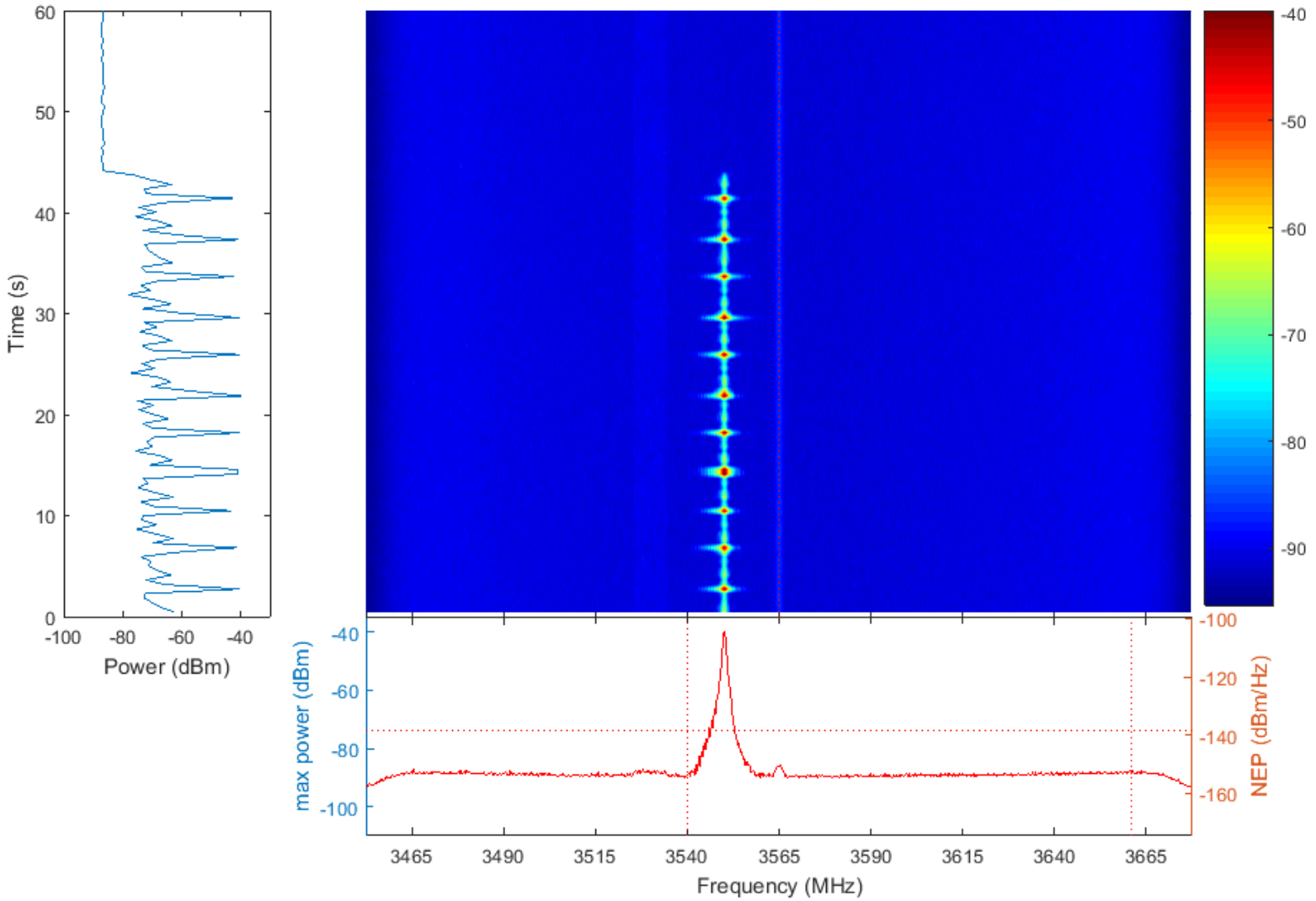

Figure 3.7: Spectrogram of a SPN-43 signal, centered near 3550 MHz, and captured with the omni-directional antenna. The frequency-domain pedestal here is roughly symmetrical around the main peak. Also, the radar source was apparently turned off at about 44 s after start of the capture. The mean peak power pooled over all rotations (while the signal was on) in this capture is -41.1 dBm with a spread of 3.3 dB.

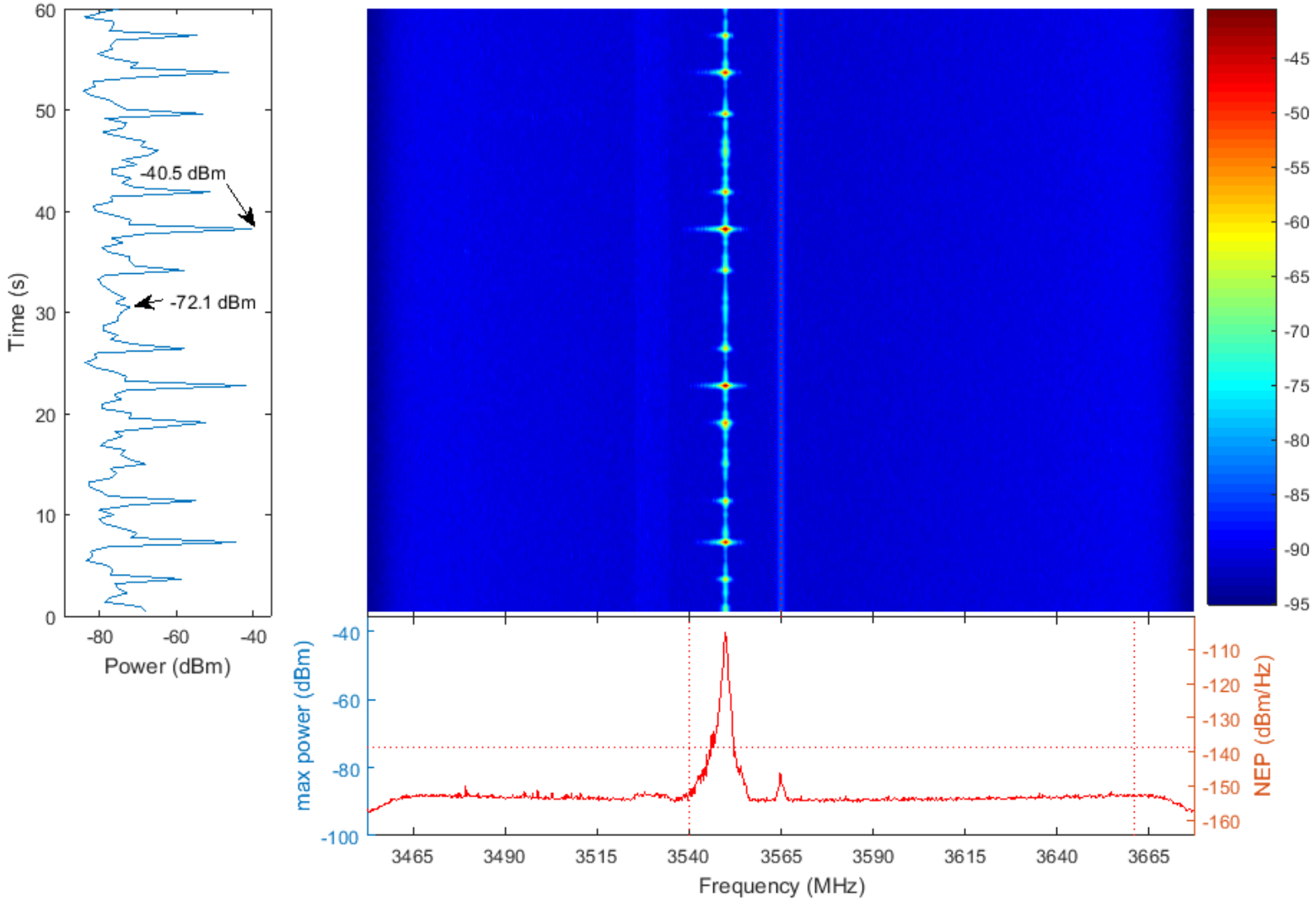

Figure 3.8: Spectrogram of a SPN-43 signal with temporal fading, captured with the omni-directional antenna showing spread of peak rotation power of 31.5 dB, while the mean peak power, pooled over all rotations in this capture, is -54.6 dBm.

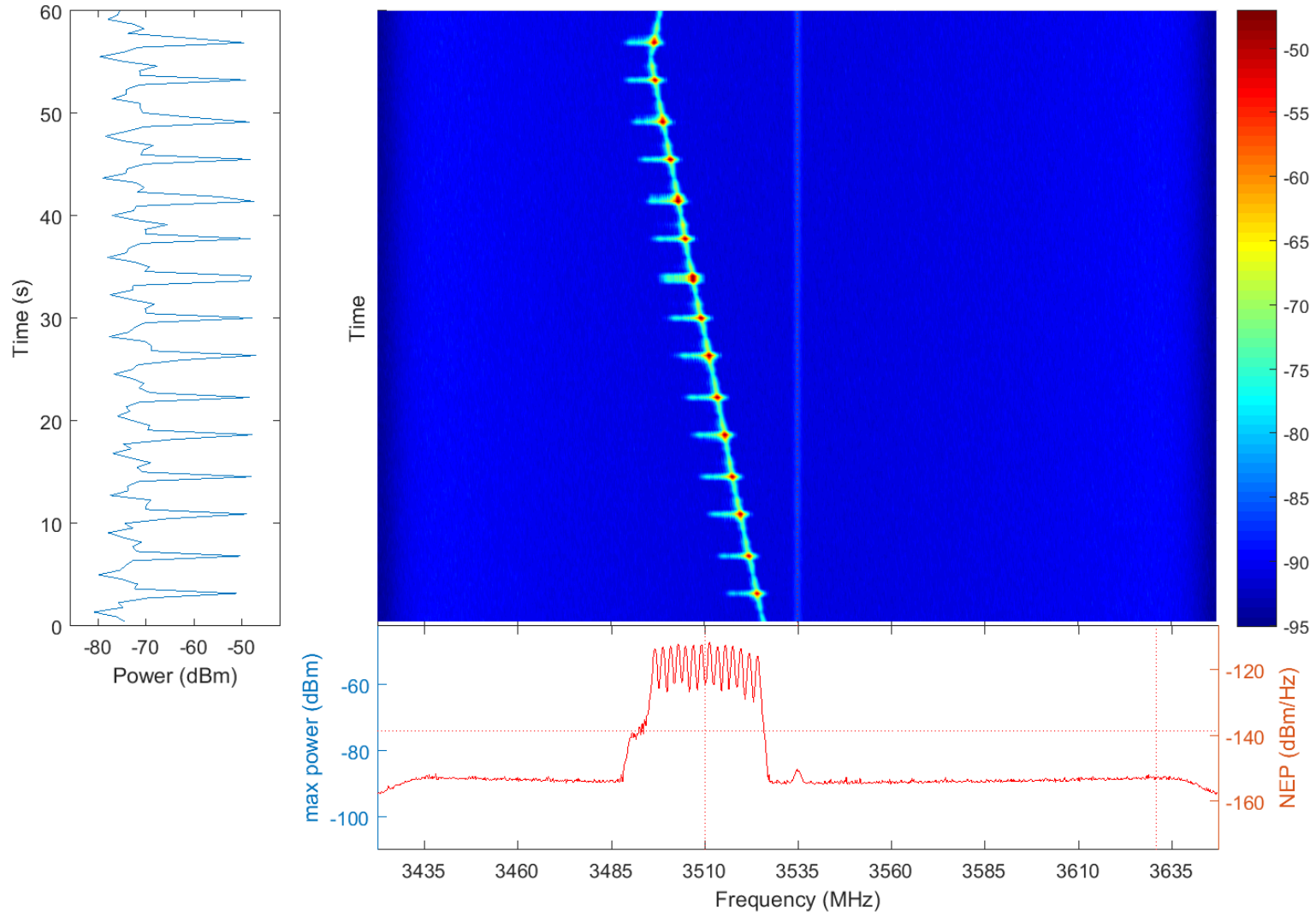

Figure 3.9: Spectrogram of a SPN-43 signal that is apparently being tuned at a rate of 0.54 MHz/s. Approximately (5 to 10) instances of tuning were observed during the Point Loma measurement campaign.

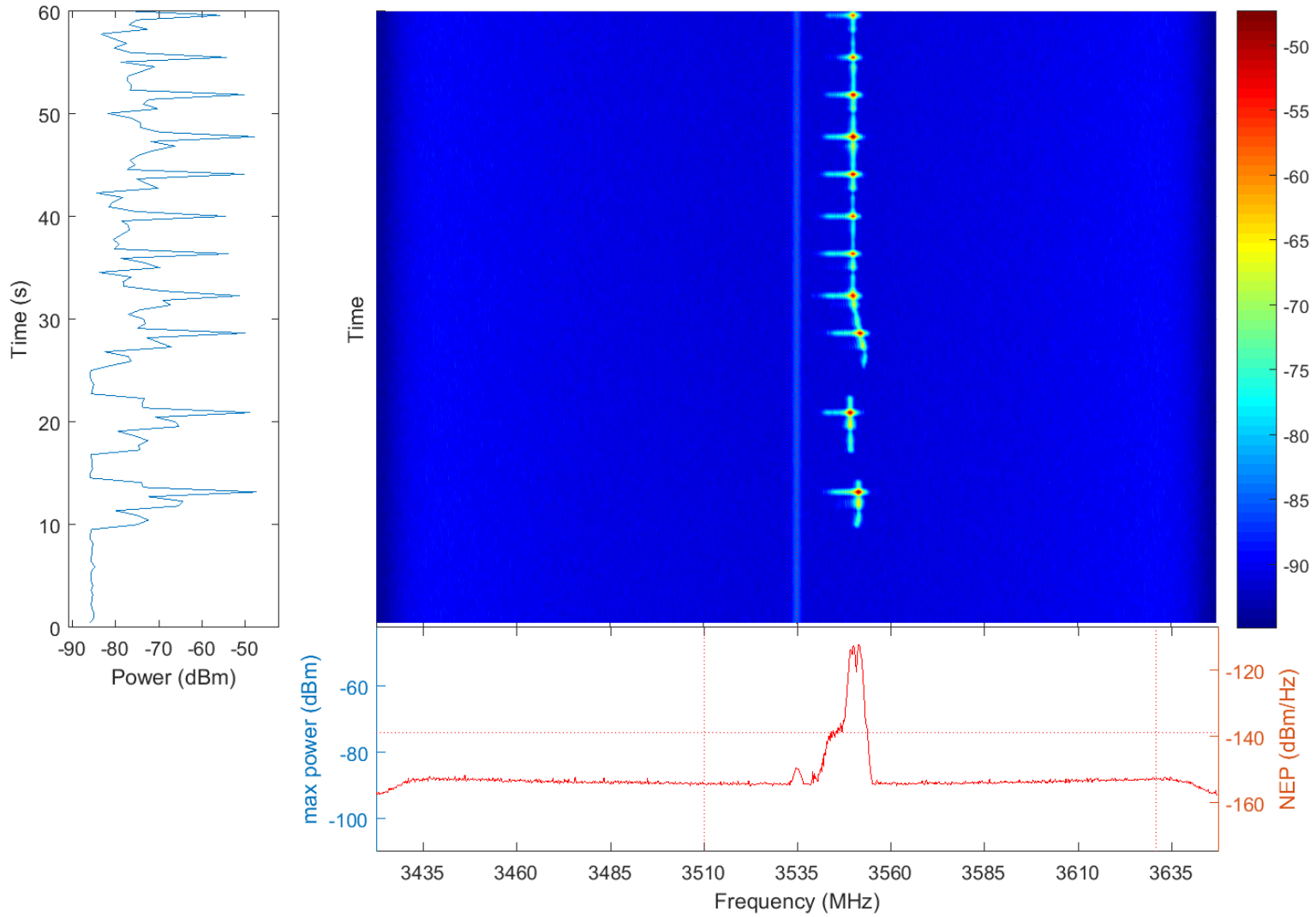

Figure 3.10: Apparent capture of SPN-43 turning on. Note changing frequency and rotation period and gaps in transmitted power during roughly the first 20 s of emissions.

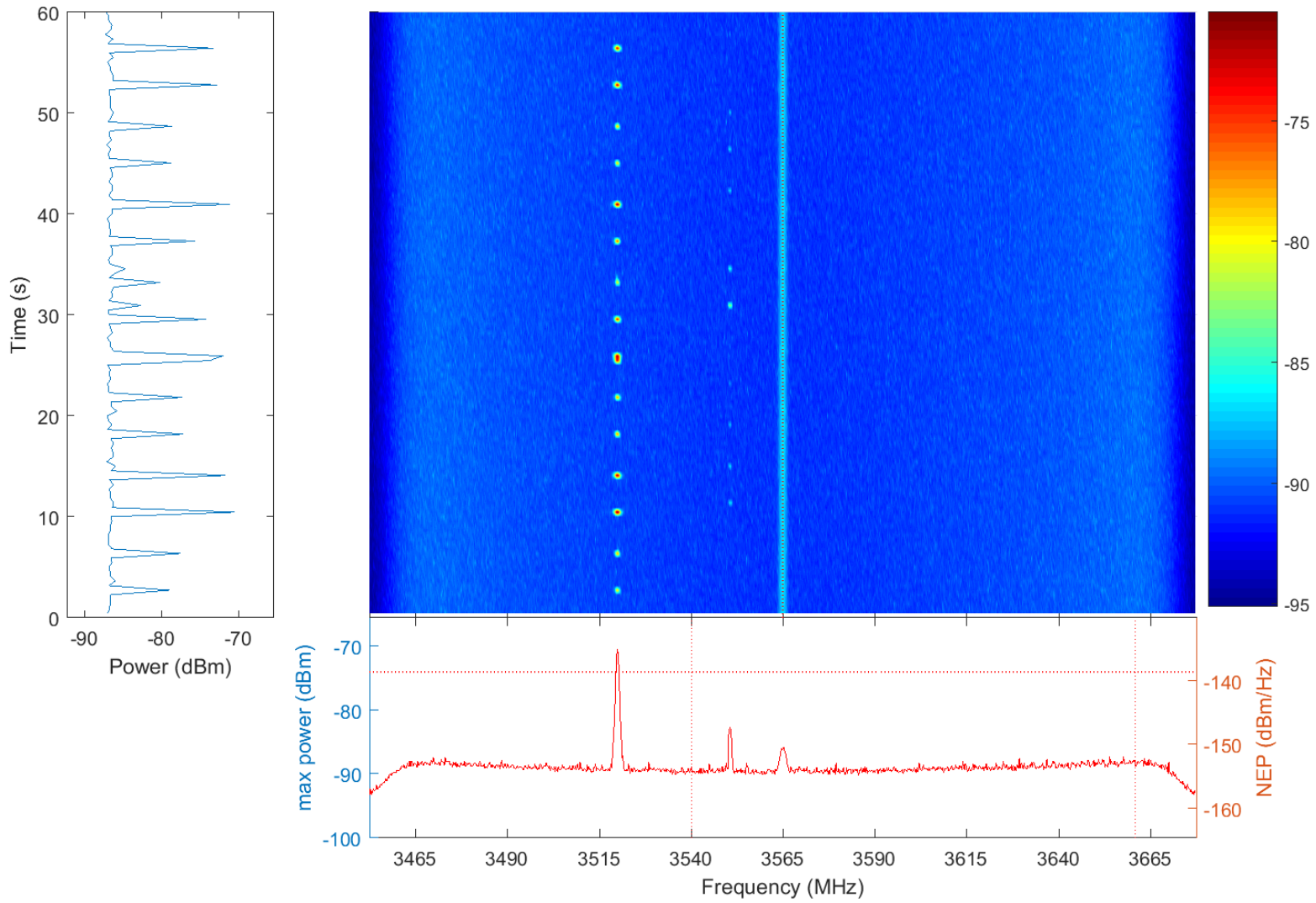

Figure 3.11: Spectrogram of SPN-43 signals at 3520 MHz and 3550 MHz. The signal at 3520 MHz had been visible for about one day previous to this capture and the signal at 3550 MHz had been present for about 30 minutes.

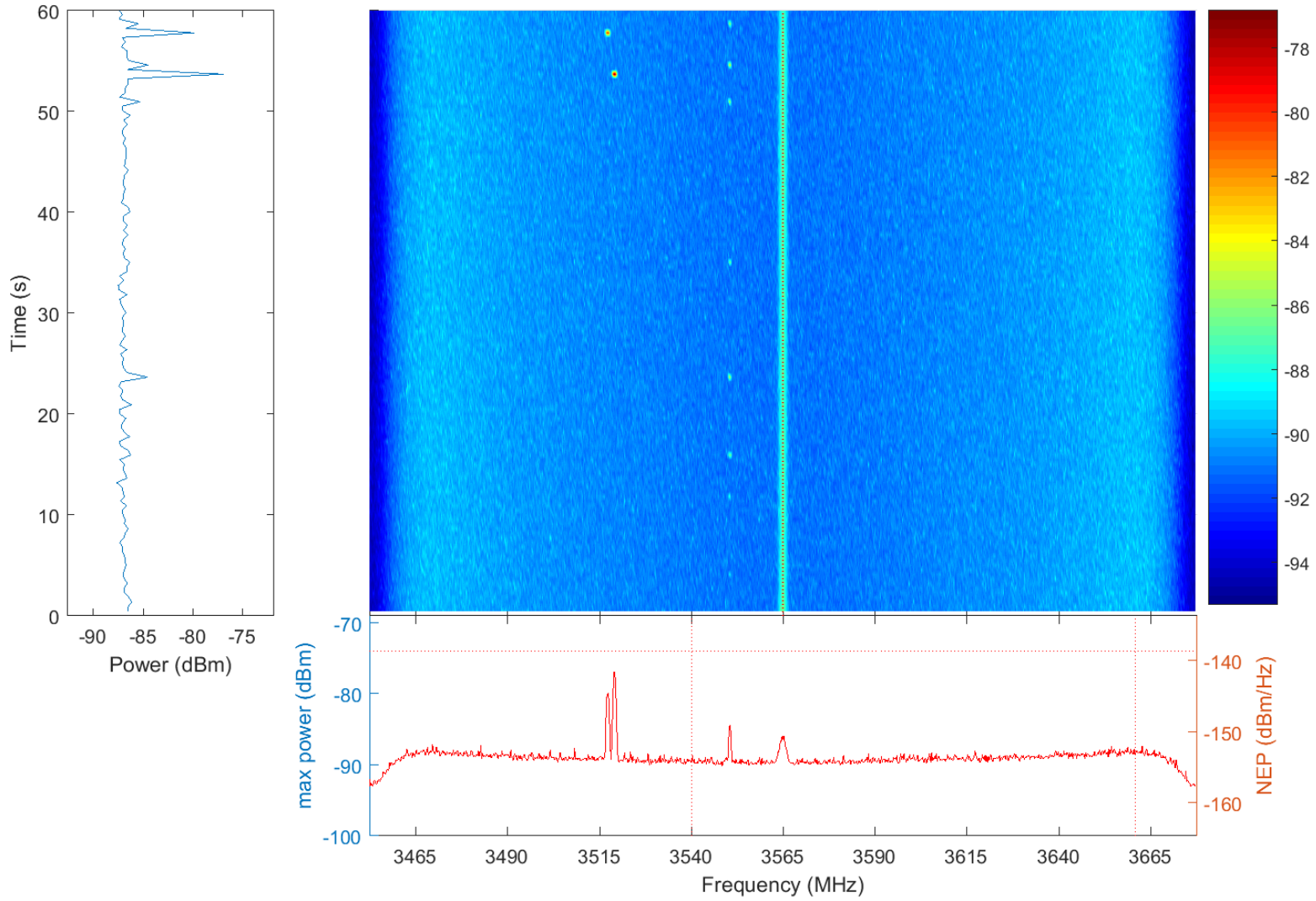

Figure 3.12: Capture occurring about 10 minutes after Fig. 3.11. Apparently, some time between the captures, radar at 3520 MHz was turned off and then started during this capture epoch. The signal at 3520 MHz appears to be tuning.

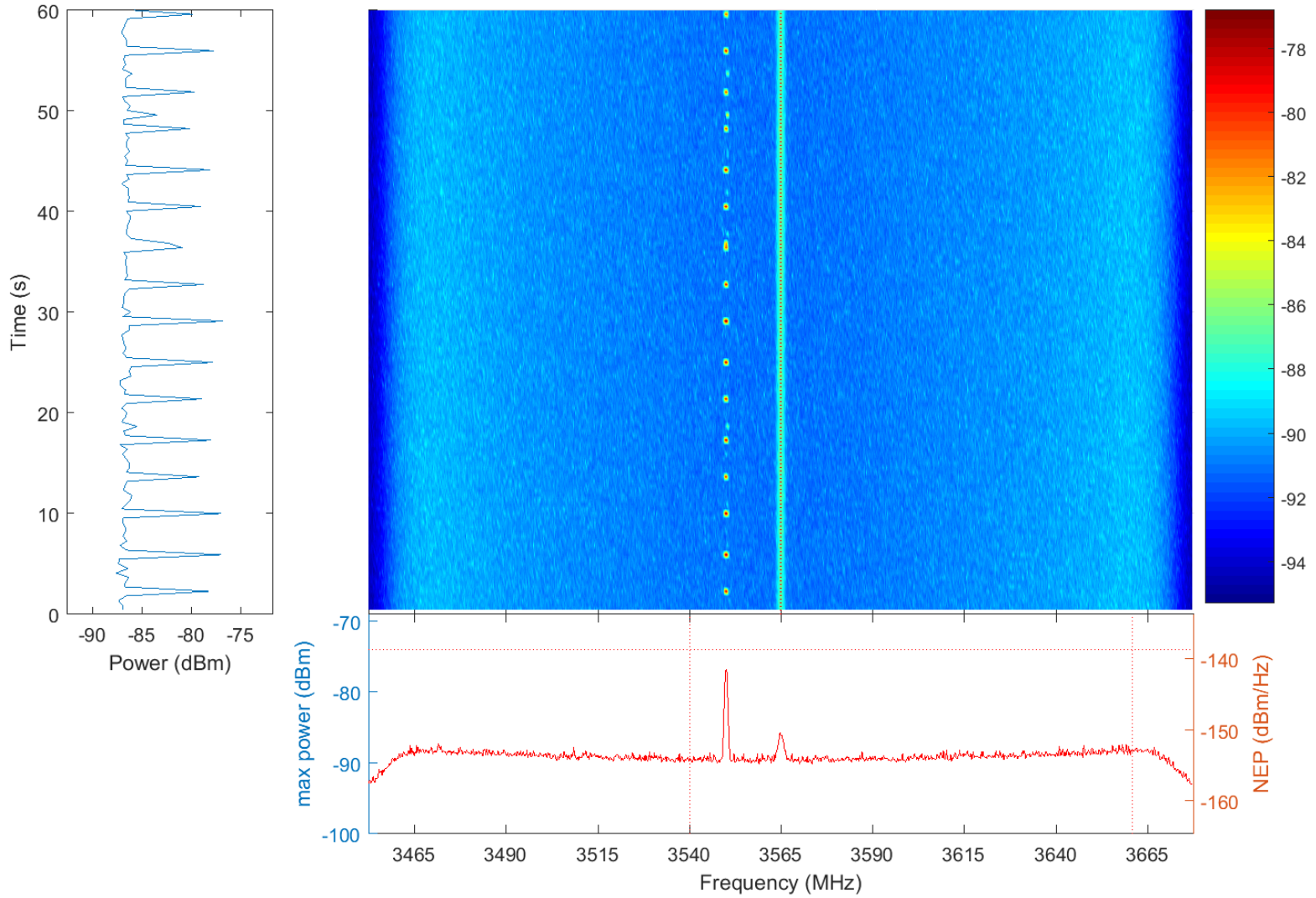

Figure 3.13: Capture occurring about 10 minutes after Fig. 3.12. At this time there is a series of signal peaks at about the same power level as was observed at 3520 MHz in the previous capture with some interleaved peaks at powers comparable to those previously observed at 3550 MHz. The high power peaks are lower in frequency than the low power peaks by about 440 kHz, (two frequency bins).

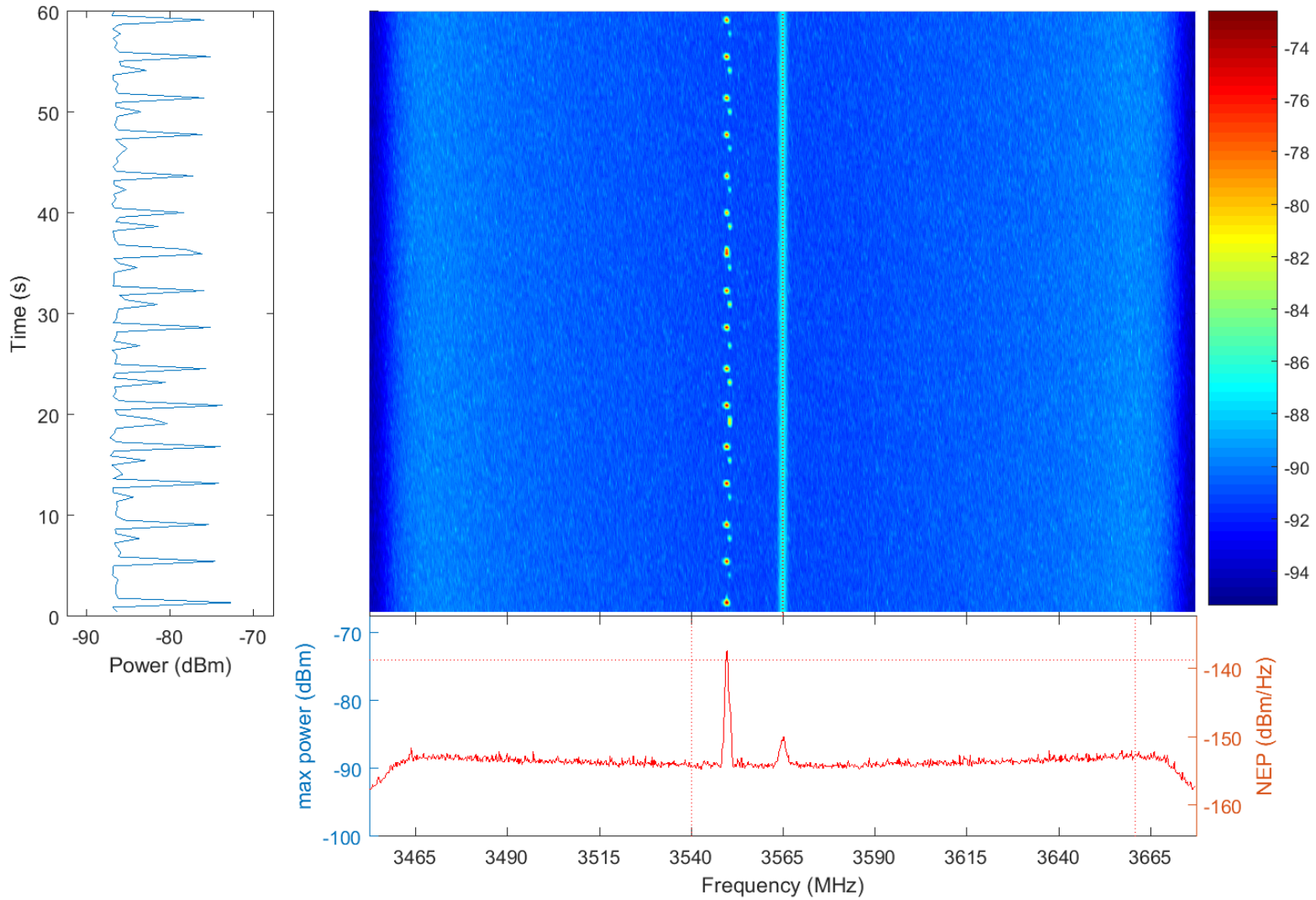

Figure 3.14: Spectrograms similar to those of Fig. 3.13 continued to be observed for several hours. This figure shows a capture about 2.5 hours after the spectrogram of Fig 3.13 was captured.

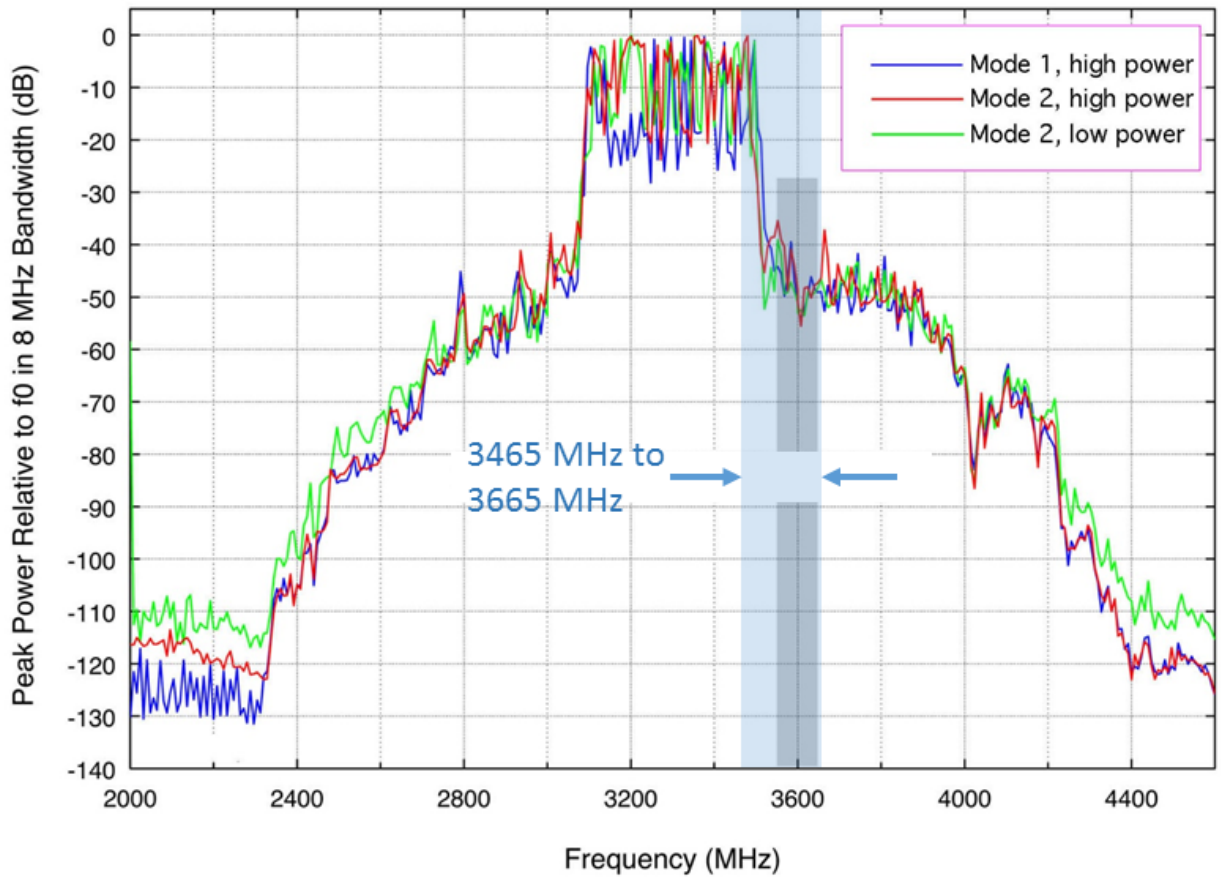

Figure 3.15: Fig. 7 of [7] showing broadband emissions of Radar 3 into the 3550 MHz to 3650 MHz band, shown by dark grey rectangle. Light grey rectangle shows 3465 MHz to 3665 MHz band typically measured in this campaign, which includes some of the primary band for Radar 3.

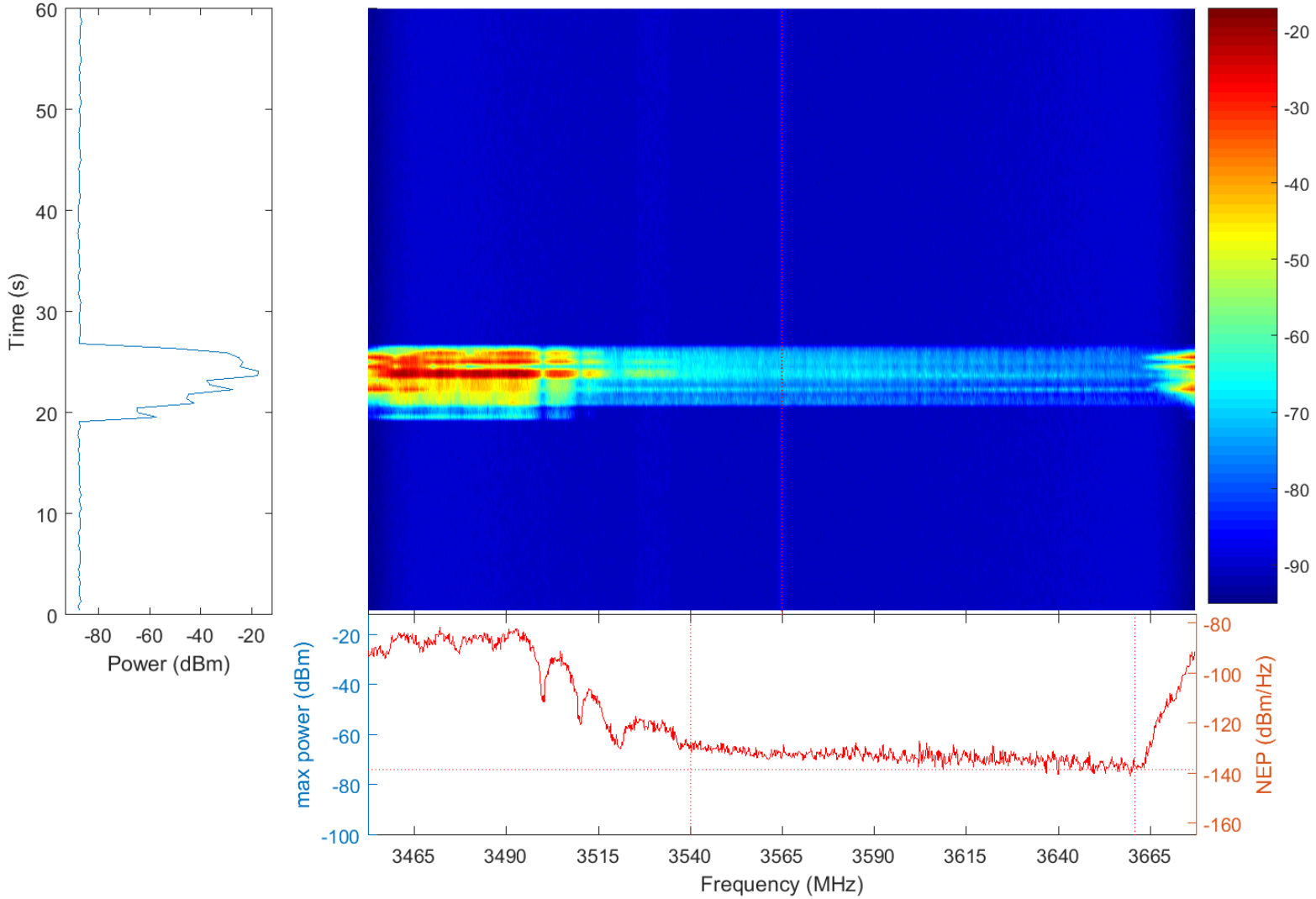

Figure 3.16: Spectrogram showing burst from Radar 3 signal at frequencies below 3540 MHz and broadband pedestal consistent with Fig. 7 of [7]. High power observed above 3665 MHz is aliased image of signal below $f_{N1} = 3452.5$ MHz.

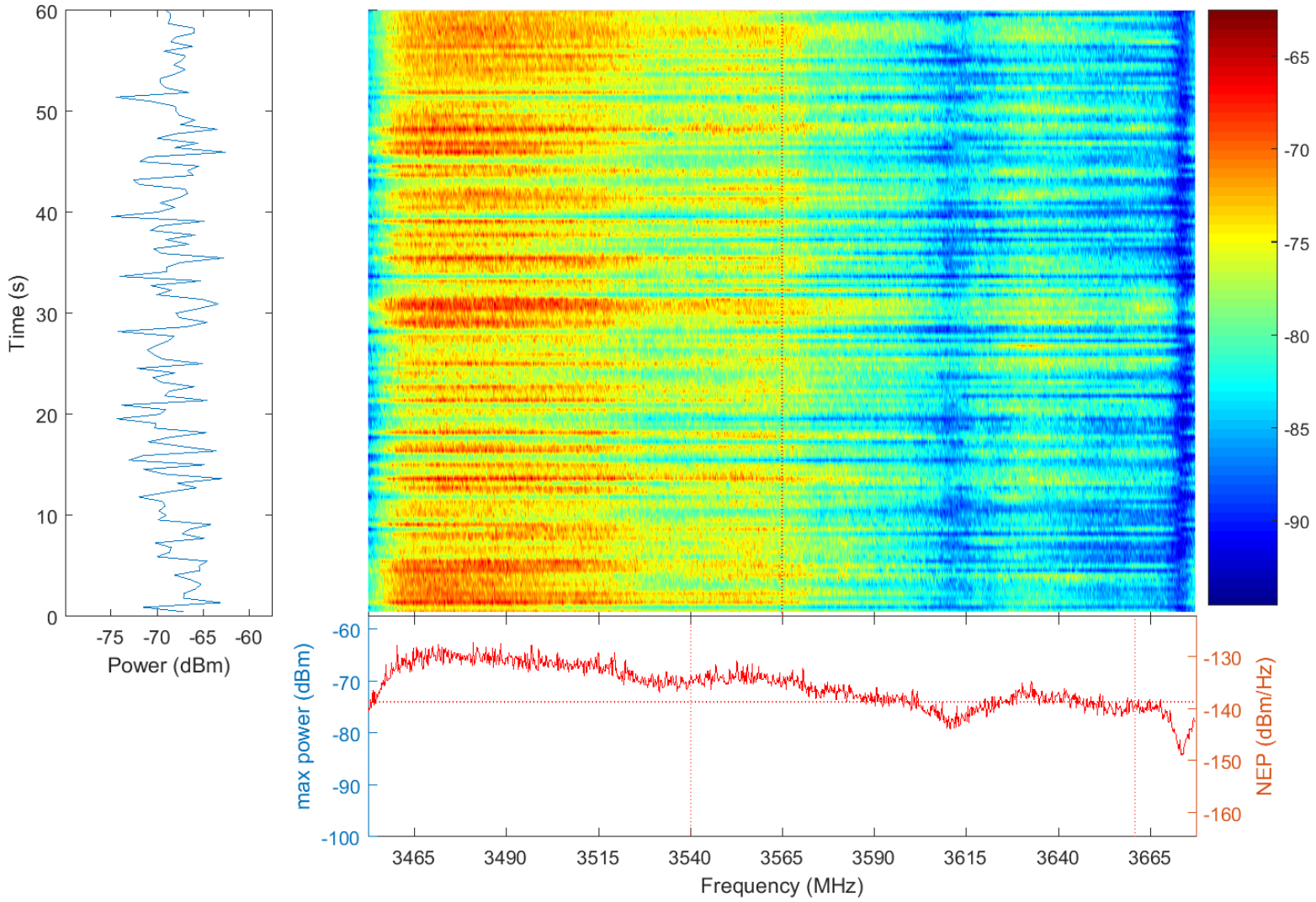

Figure 3.17: Spectrogram showing broadband noise from Radar 3.

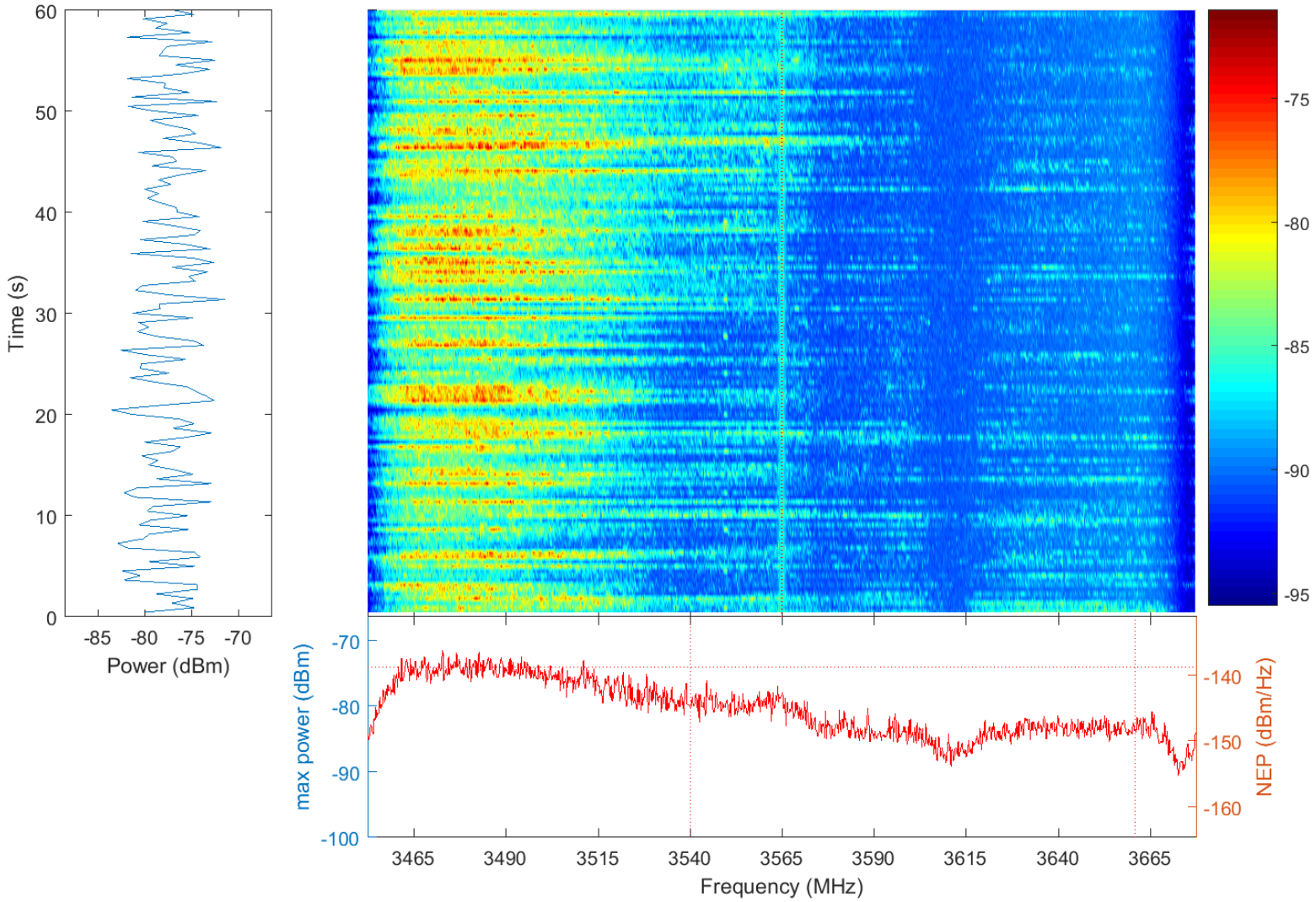

Figure 3.18: Spectrogram showing broadband noise from Radar 3. Note that SPN-43 peaks at 3550 MHz are visible at times earlier than 30 s, but are hidden by interference at later times.

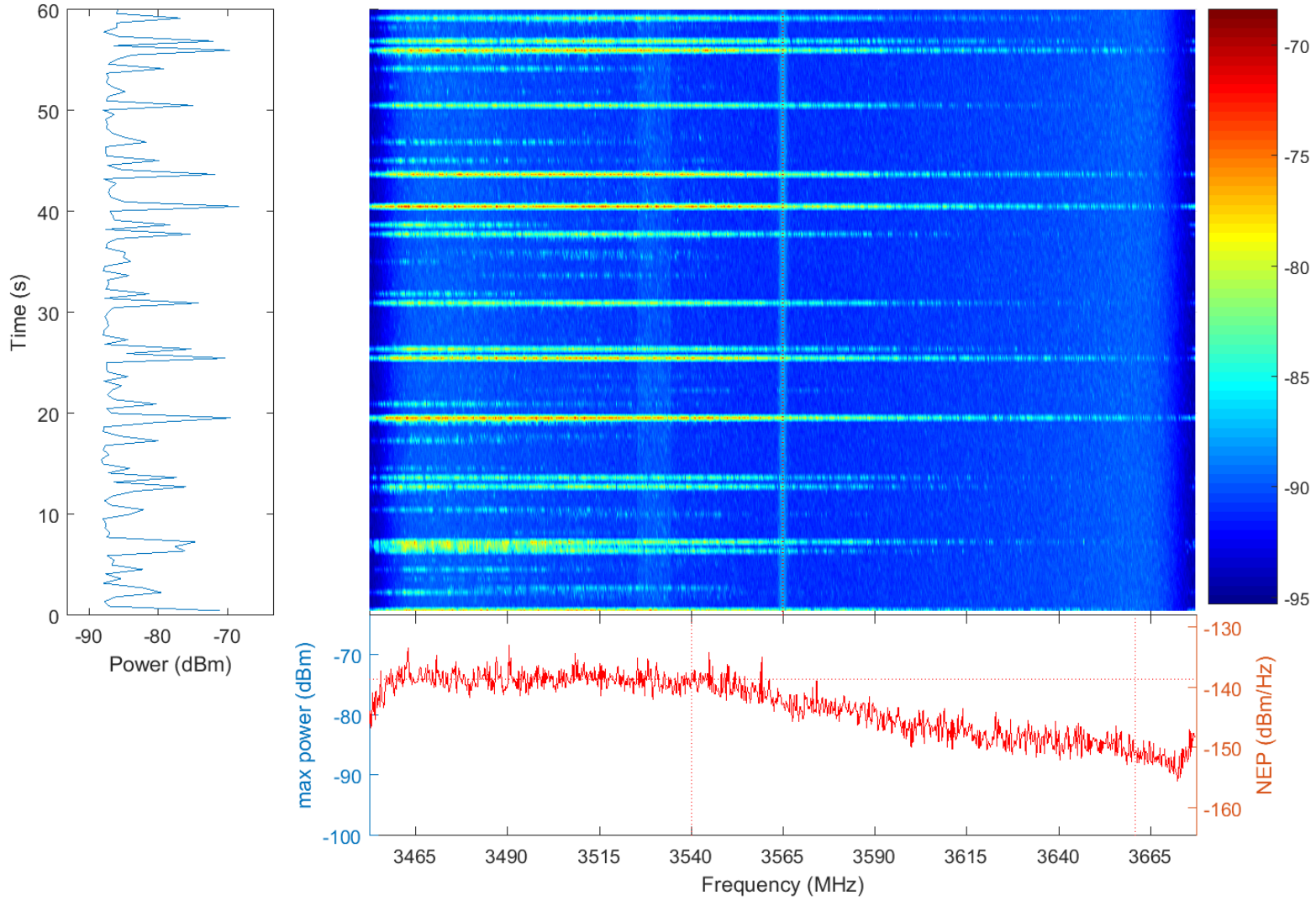

Figure 3.19: Spectrogram showing broadband pulsed noise from Radar 3.

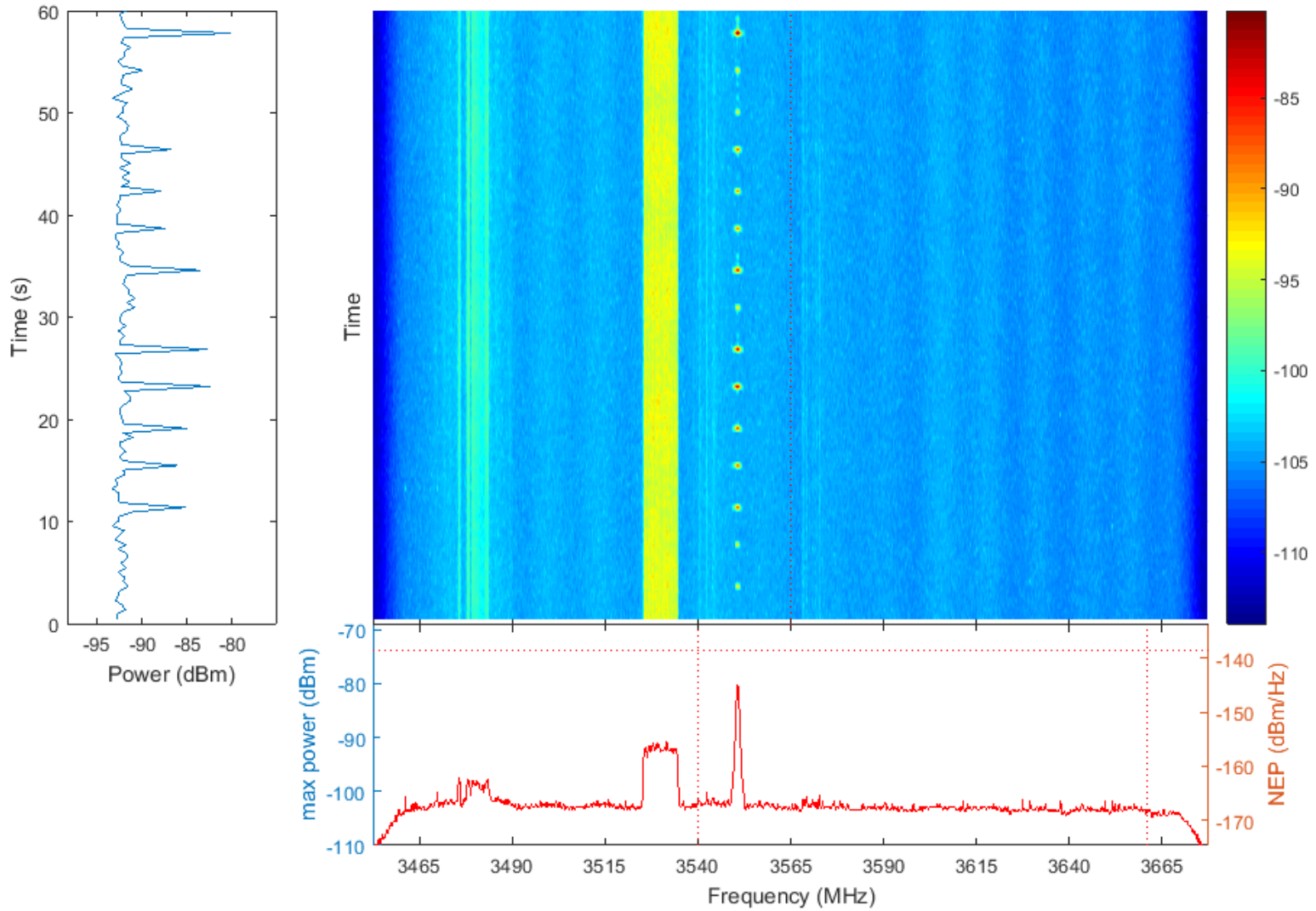

Figure 3.20: Spectrogram showing four WiMax-like signals and a SPN-43 signal. Signals were captured by use of the omni-directional antenna and by setting the VST reference level to -30 dBm.

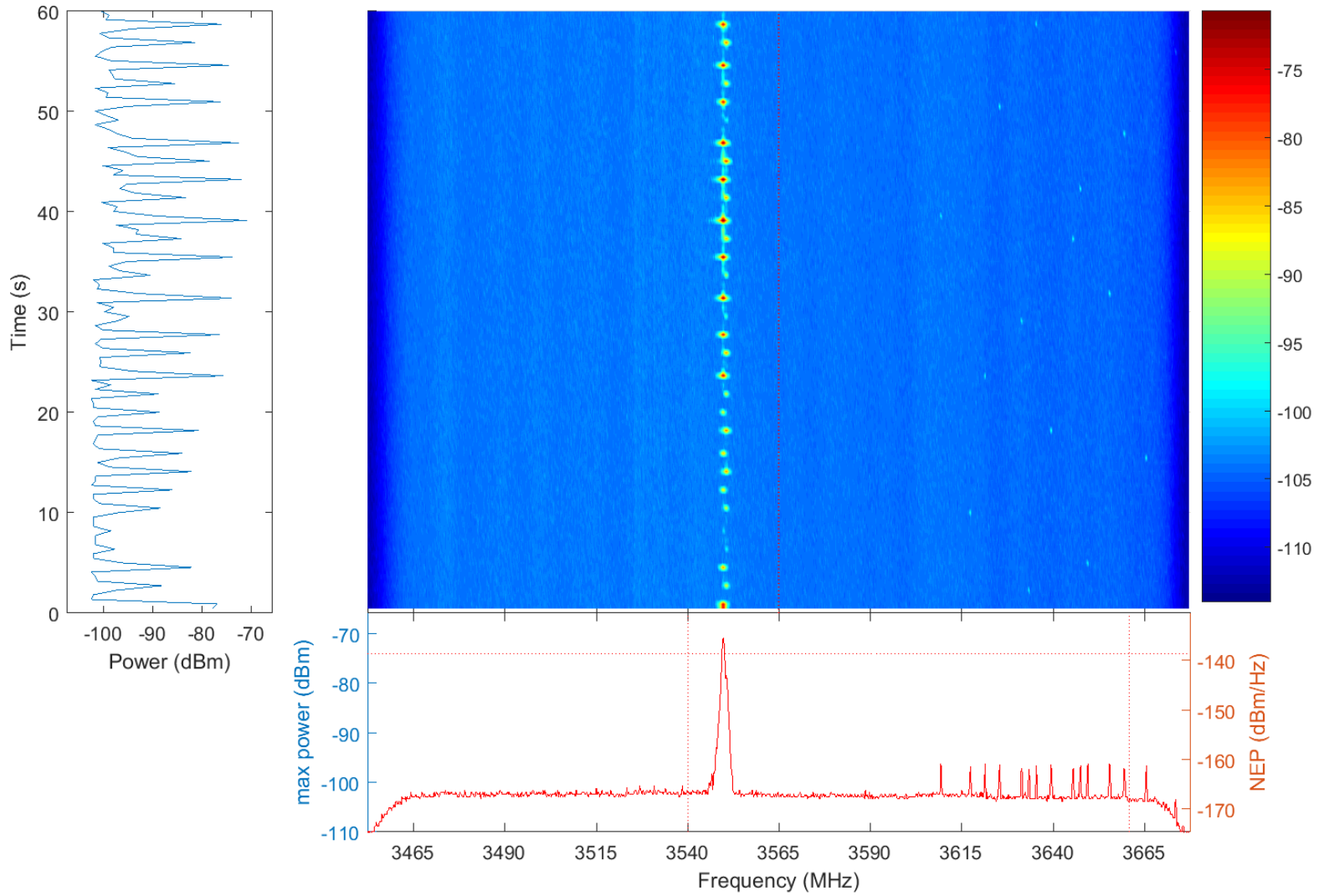

Figure 3.21: Spectrogram showing frequency hopping signal, above approximately 3609 MHz, observed by lowering the VST reference level to -30 dBm. SPN-43 at 3550 MHz, possibly from two sources, is also clearly visible.

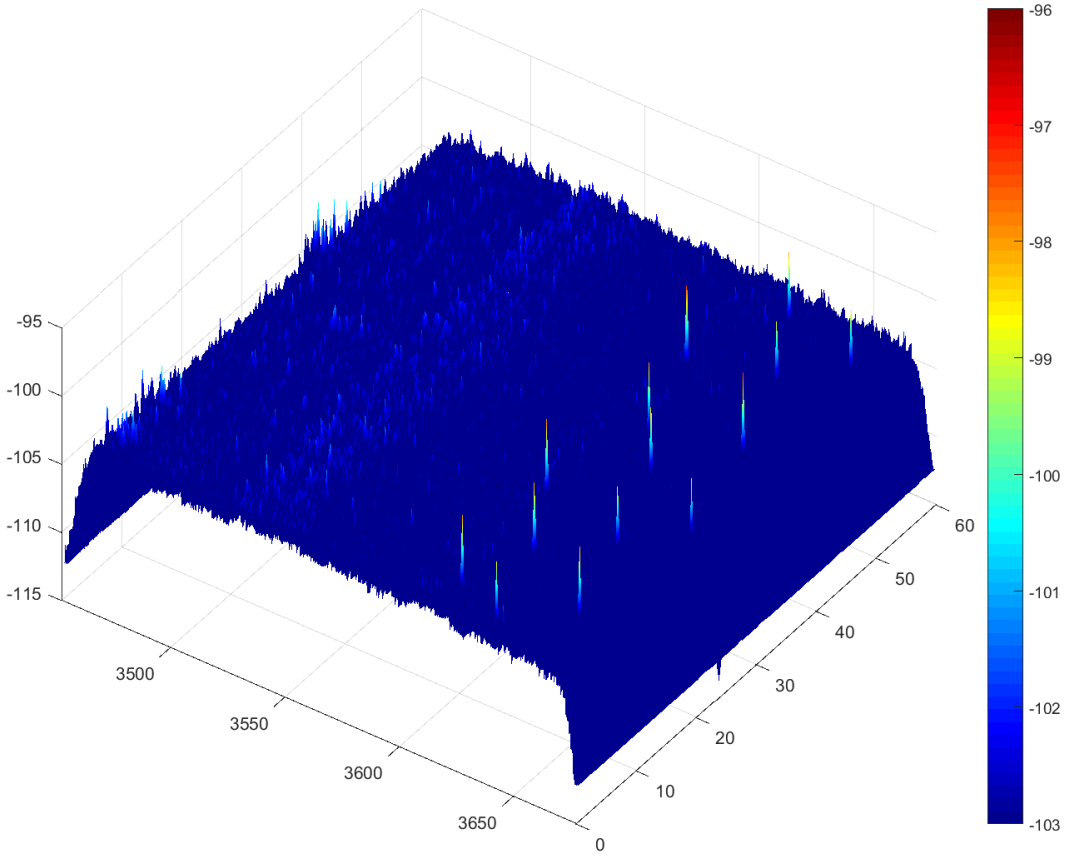

Figure 3.22: Oblique view of spectrogram showing frequency hopping signal, above approximately 3609 MHz, observed by lowering the VST reference level to -30 dBm. Note that, for visualization purposes, the vertical scale has been expanded.

Chapter 4

Waveform Parameter Analysis

This chapter presents an analysis of the radar waveforms measured in or near the 3550 MHz to 3650 MHz band. It begins with a summary of the collected data followed by a quantitative analysis of specific radar parameters.

4.1 Summary of collected data and processing

A total of 1863 high-fidelity, 60-s recordings were acquired over the two-month period of measurement at Point Loma. A subset of approximately 800 acquisitions was identified as not containing measurable emissions from out-of-band radar systems below 3500 MHz, and this subset was used for further processing using algorithms described in Appendix A.

Data processing first identifies the locations in time and frequency of the main-beam emissions of the radar in each acquisition. There are typically 15 sweeps of the main beam in each 60-s acquisition. The maximum amplitude of each sweep and the time of its occurrence relative to the beginning of the acquisition are recorded.

Data processing then identifies the pulses within each sweep. Specifically, it selects pulses having amplitudes within 3 dB of the peak power of each sweep. Approximately 20 pulses are identified in each sweep. A number of parameters are then computed for each pulse, namely its maximum amplitude, center frequency, pulse duration, and the time interval between consecutive pulses.

Out of the approximately 800 60-s acquisitions that were selected for processing, a total of about 11 300 antenna sweeps and close to 223 000 pulses were identified for analysis. Table 4.1 breaks down the pulses by the antenna used for collection (omnidirectional vs. cavity-backed spi-

	3520 MHz	**3550 MHz**	**3600 MHz**	Total by Antenna
Omni	$0\,\%$	$71.0\,\%$	$2.4\,\%$	$73.5\,\%$
CBS	$4.0\,\%$	$15.2\,\%$	$7.3\,\%$	$26.5\,\%$
Total by Frequency	$4.0\,\%$	$86.3\,\%$	$9.7\,\%$	

Table 4.1: Percentage of processed data by antenna and pulse center frequency

	3520 MHz	**3550 MHz**	**3600 MHz**	by Antenna
Omni	0	13	1	14
CBS	2	5	2	8
by Frequency	2	18	3	

Table 4.2: Number of days over which data was collected, by antenna and pulse center frequency[1]

ral) and the approximate center frequency of the pulses. The majority of pulses ($73.5\,\%$) were captured with the omnidirectional antenna, and of those the vast majority were observed at 3550 MHz.

The processed data was collected over 22 unique calendar days. This data is a subset of the total data collected over the course of two months. Table 4.2 lists the number of calendar days over which the data was collected, broken down by antenna and frequency.

4.2 Sweep parameters

4.2.1 Peak sweep power

Fig. 4.1 shows a histogram of the analyzed radar sweeps by peak sweep power at the output of the measurement antenna over the entire analysis bandwidth. The peak sweep power of the analyzed data ranges from -54 dBm to -15 dBm, and the most frequent peak power (the mode) is just below -30 dBm.[2] Considering that pulses within 3 dB of the peak power are analyzed, the pulse analysis below comprises a range of over 40 dB.

[1]Data collected with the CBS antenna totals 8 days because on one of those days radar was observed at both 3520 MHz and 3550 MHz.

[2]Note that the peak powers quoted here, measured in the time domain, are higher than their frequency-domain counterparts in Chapters 2 and 3 due to time-averaging of the approximately 1 μs pulse in the 1024-sample (4.55 μs) window of the discrete Fourier transform. The difference due to pulse desensitization in the frequency domain is approximately 13 dB, assuming a rectangular pulse shape.

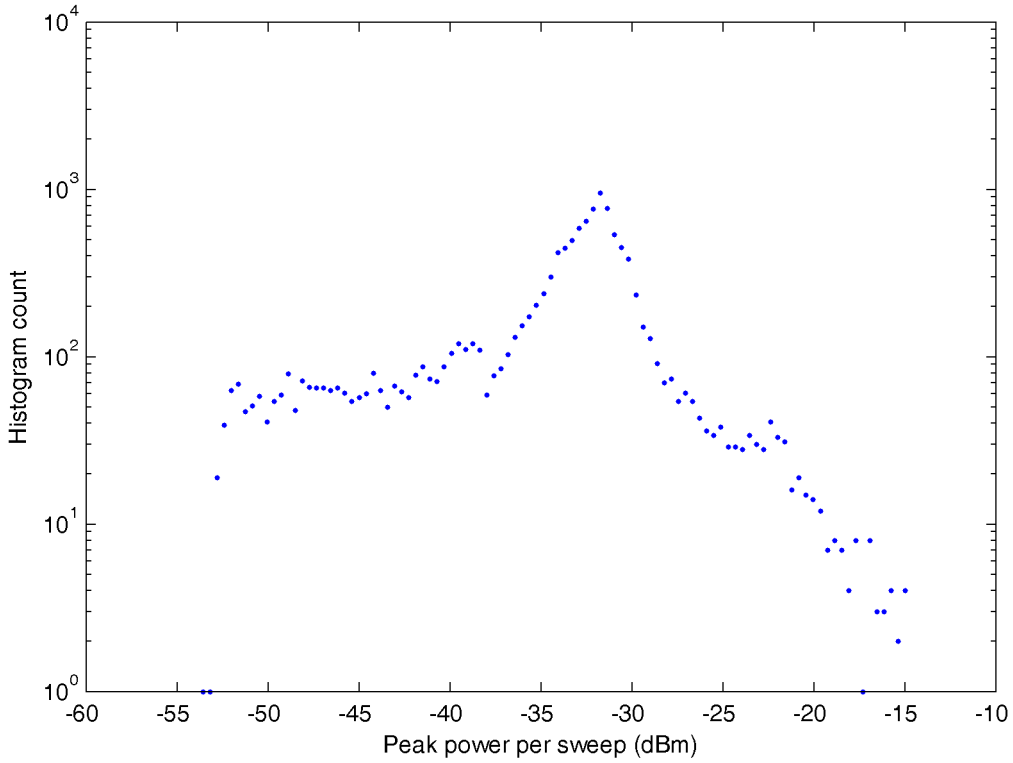

Figure 4.1: Histogram of peak power per antenna sweep

4.2.2 Sweep interval

The sweep interval is the time interval between successive peaks of received power due to the rotation of the radar's transmitting antenna in the azimuth plane. Fig. 4.2 plots the empirical cumulative distribution function (CDF) and complementary CDF (CCDF) of the sweep interval for all $11\,300$ sweeps. The empirical CDF and CCDF depict the distribution of the observations from which key percentiles, including the median, can be read. Probabilities are shown on a logarithmic scale in order to better view the lower tail of the distribution via the CDF and the upper tail via the complementary CDF (one minus the CDF). For example, Fig. 4.2 shows that the median sweep interval is 3.854 s (≈ 0.15 s lower than given in [5]), and that $98\,\%$ of the measured sweep intervals lie between 3.833 s and 3.885 s. The antenna rotation rates corresponding to the $98\,\%$ interval are (15.44 to 15.65) rotations per minute. The dotted lines in Fig. 4.2 represent the $95\,\%$ confidence bounds on the empirical data, assuming independence of the observations [17].

Fig. 4.3 illustrates the empirical CDF and CCDF of the sweep interval by the antenna used for data collection. We observe that the distribution of the sweep interval observed with the cavity-backed spiral (CBS) antenna has slightly heavier tails. Note, however, that the flatness of the CCDF of the CBS data above 3.88 s is the result of individual sweeps of the radar antenna being missed by the data processing algorithm due to channel fading. Such missed detections of the sweep lead

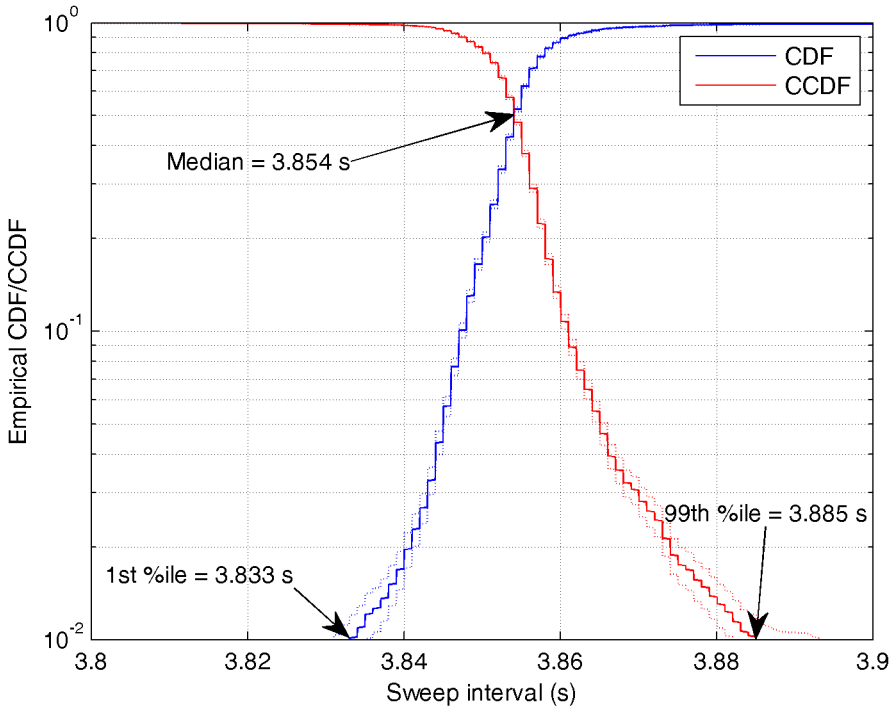

Figure 4.2: Empirical CDF and complementary CDF (CCDF) of sweep interval annotated with select percentiles (%ile)

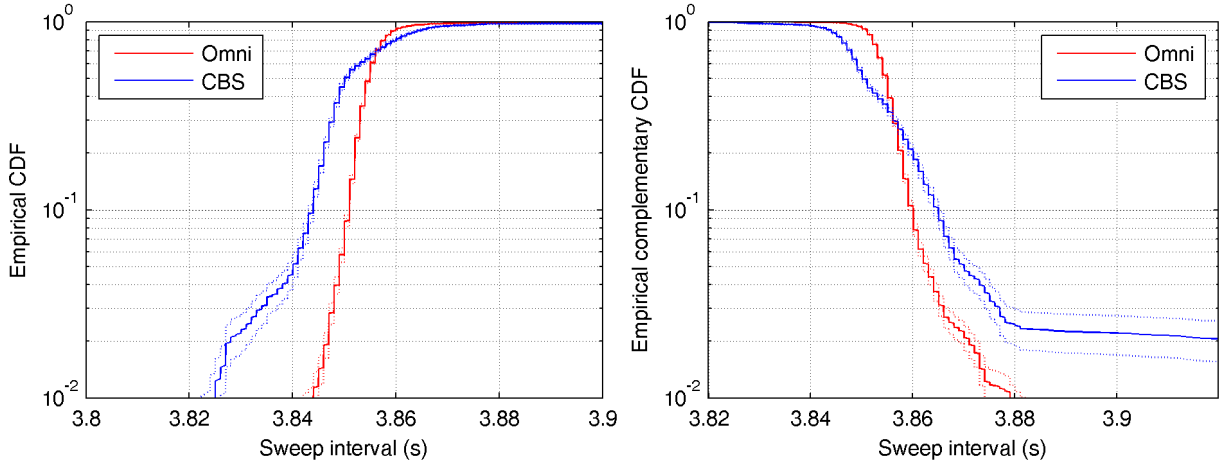

Figure 4.3: Empirical CDF and CCDF of sweep interval by antenna type

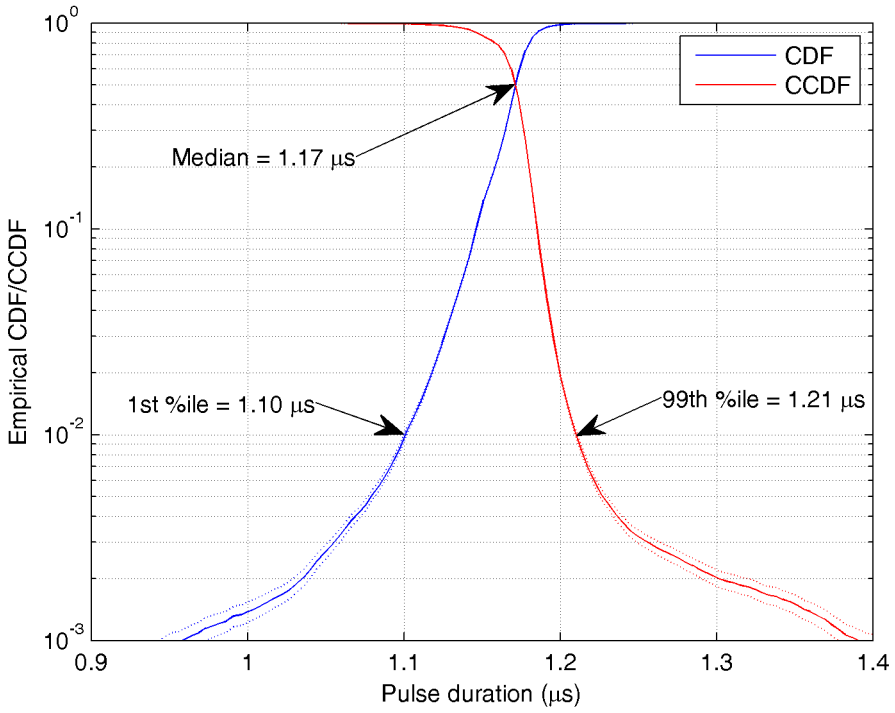

Figure 4.4: Empirical CDF and CCDF of pulse duration over all data

to sweep intervals that appear as multiples of 3.85 s.

4.3 Pulse parameters

4.3.1 Pulse duration

Pulse duration is defined as the time between the rising-edge and falling-edge crossings by the pulse envelope of half the maximum amplitude of the pulse (see Appendix A for a more detailed description). Fig. 4.4 plots the empirical CDF and CCDF of the pulse duration over all $223\,000$ analyzed pulses. The empirical distributions indicate that the median pulse duration is 1.17 μs (0.22 μs higher than expected from [5]), and that 98 % of the measured pulse durations lie between 1.10 μs and 1.21 μs.

Fig. 4.5 shows the empirical CDF and CCDF of the pulse duration by the antenna used for data collection. Although the median and 10th percentile of the two data sets differ by only 13 ns and 22 ns, respectively, pulse durations observed with the omnidirectional antenna have heavier tails. For example, the 99.9th percentile of the pulse duration observed with the omnidirectional antenna

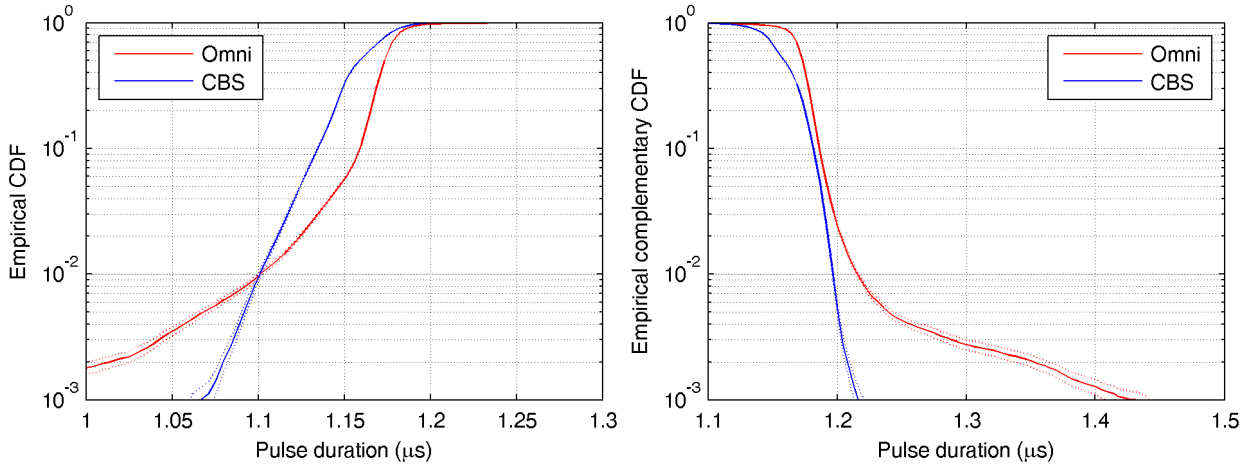

Figure 4.5: Empirical CDF and CCDF of pulse duration by antenna type

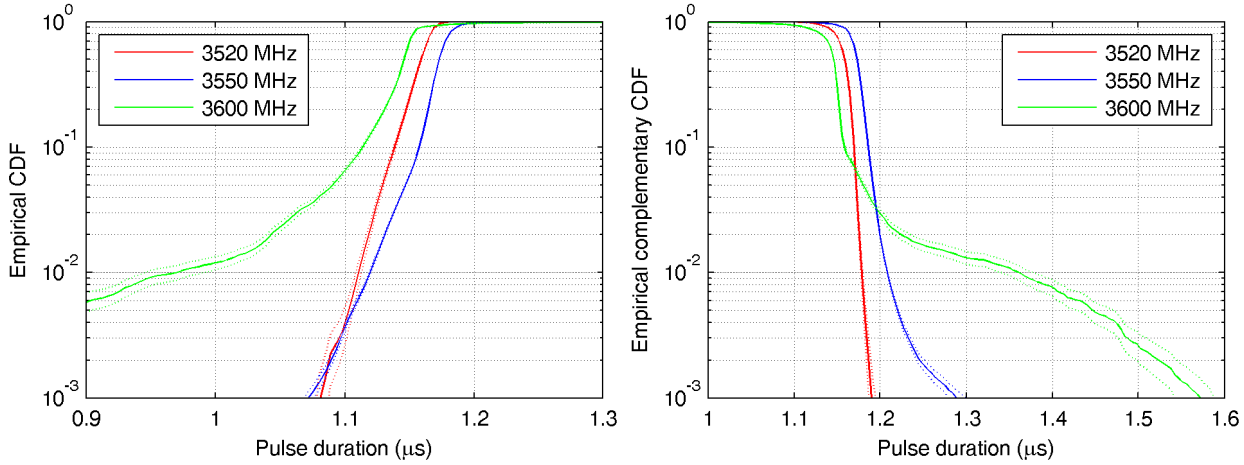

Figure 4.6: Empirical CDF and CCDF of pulse duration by center frequency

(i.e., at 10^{-3} of the CCDF) exceeds that observed with the CBS antenna by 218 ns. The greater frequency of longer pulse durations could be due to the longer paths of reflections and the different gain patterns of the antennas. An omnidirectional antenna receives pulse reflections off terrain and other objects from all azimuth angles with equal gain, whereas the CBS antenna has higher gain toward sea and lower gain toward potential reflectors on land. Other possible explanations include different ship positions or different atmospheric conditions between the two data sets.

Fig. 4.6 illustrates the distribution of the measured pulse durations by center frequency. The center frequency can be used as a surrogate for unique radar transmitters, assuming that each transmitter operates at a different frequency.[3] We observe that the median pulse duration differs

[3]As observed in Section 3.5, the assumption of a one-to-one correspondence between frequency and system does not hold universally.

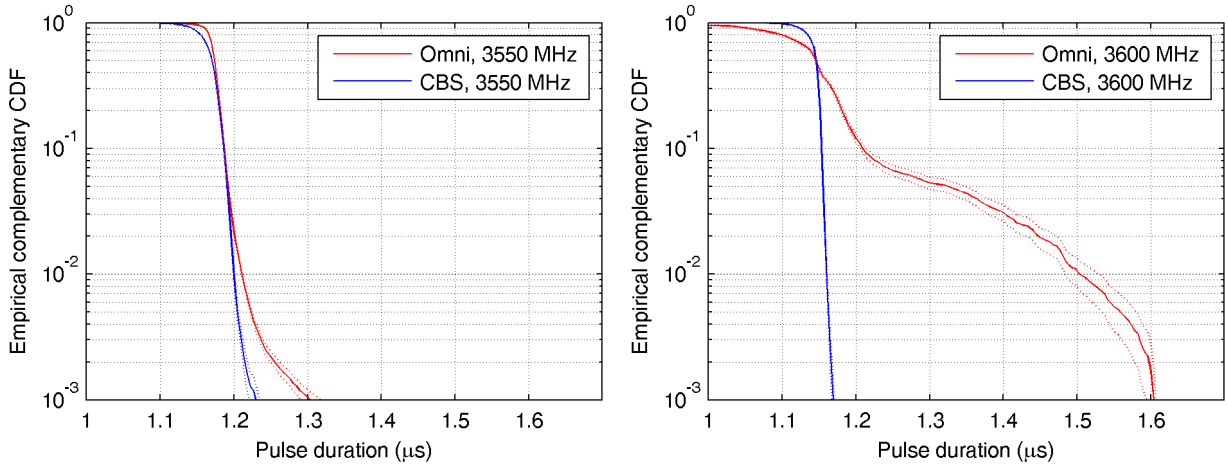

Figure 4.7: Empirical CCDF of pulse duration at 3550 MHz and 3600 MHz by antenna type

by 27 ns across the three observed frequencies. However, a much larger difference is observed in the tails, with the 1st to 99th percentile range differing by a third of a microsecond between the 3600 MHz data and the other two frequencies.

Fig. 4.7 shows the breakdown of the 3550 MHz and 3600 MHz pulse durations by antenna. (Recall from Table 4.1 that no data was available at 3520 MHz with the omnidirectional antenna.) The 3600 MHz pulse durations exhibit a clear difference between the omnidirectional and CBS antennas; although their medians are close, their 90th and 99th percentiles differ by 53 ns and more than a third of a microsecond, respectively.

4.3.2 Pulse repetition interval

The pulse repetition interval is defined as the time between the rising-edge crossings by the envelopes of two successive pulses of their respective half-amplitude levels. Fig. 4.8 plots the empirical CDF and CCDF of the pulse repetition interval aggregated over the total population of pulses. These results show a median pulse repetition interval that is within 13 ns of 1 ms, and that 98 % of the values lie within a range of 40 ns.

The aggregate results are dominated, however, by observations with the omnidirectional antenna at 3550 MHz. Segmenting by antenna and center frequency reveals heavier tails for the observations at 3520 MHz and 3600 MHz, as shown in Fig. 4.9, as well as for measurements with the CBS antenna, which comprise a more balanced sampling of the three frequencies. Though the tails of these subclasses are heavier, their 98 % intervals still lie within a range of just 62 ns, or 62 parts per million of the median value.

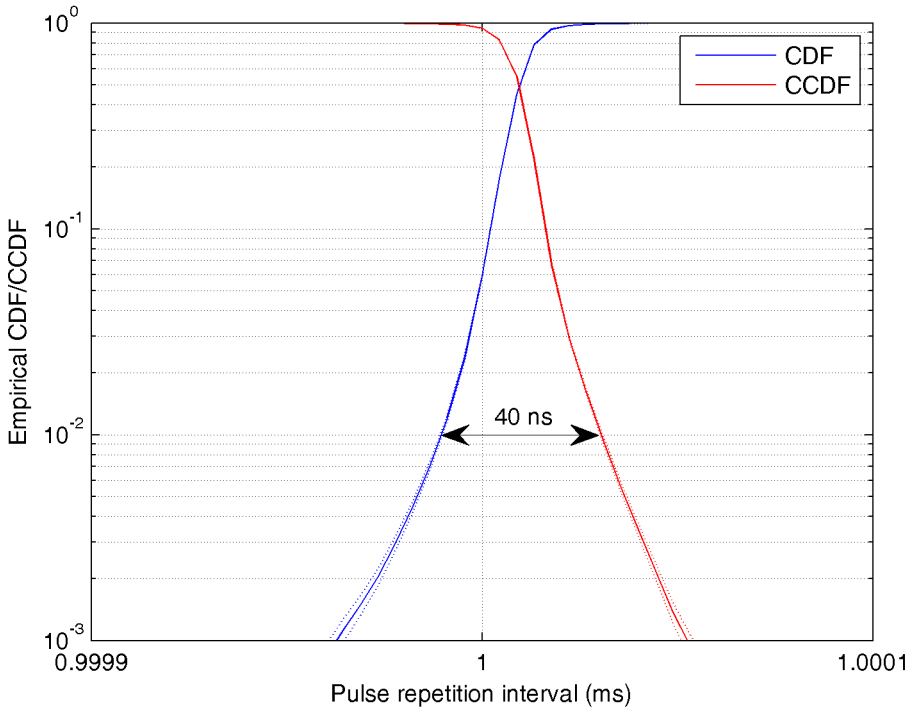

Figure 4.8: Empirical CDF and CCDF of pulse repetition interval over all data

4.3.3 Frequency offset

The frequency offset is defined as the difference between the measured center frequency of a pulse and its nominal center frequency.[4] Fig. 4.10 plots the empirical CDF and CCDF of the frequency offset aggregated over the total population of pulses. The empirical distribution shows a median offset of 663 kHz and 1st and 99th percentiles of -311 kHz and 828 kHz, respectively.

Fig. 4.11 plots the empirical distributions of the frequency offset by center frequency. The results show a larger spread in frequency offset for the 3550 MHz observations than for the other two center frequencies. Between the 1st and 99th percentiles, the 3520 MHz observations vary by 385 kHz, the 3550 MHz observations vary by 1.15 MHz, and the 3600 MHz observations vary by 522 kHz. Fig. 4.12 shows a histogram of the same data.

[4]The center frequency of a pulse is measured with an 8192-point FFT and, hence, has a resolution of $f_S/8192 = 225 \times 10^6/8192$ Hz ≈ 27.5 kHz.

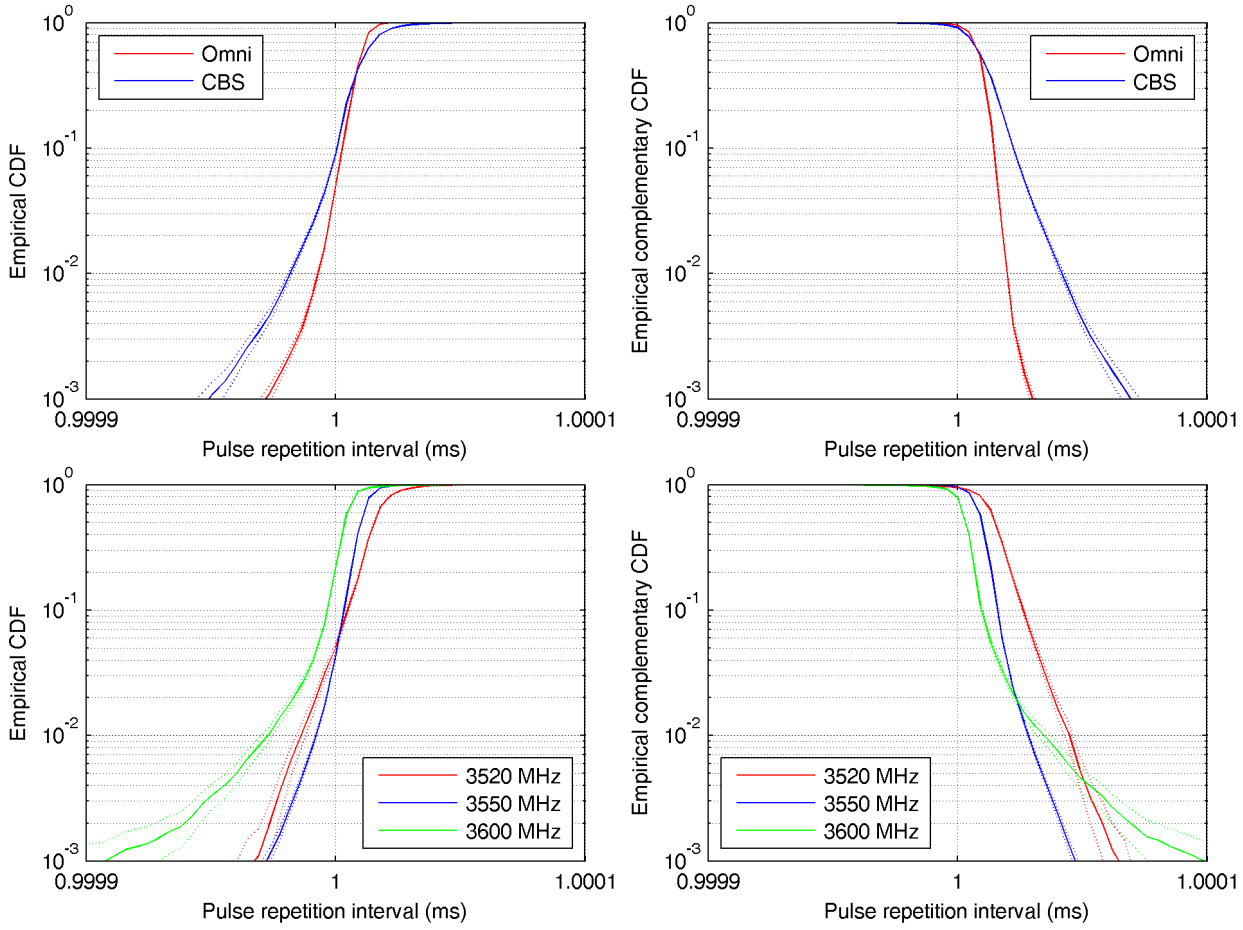

Figure 4.9: Empirical CDF and CCDF of pulse repetition interval by antenna type and by frequency

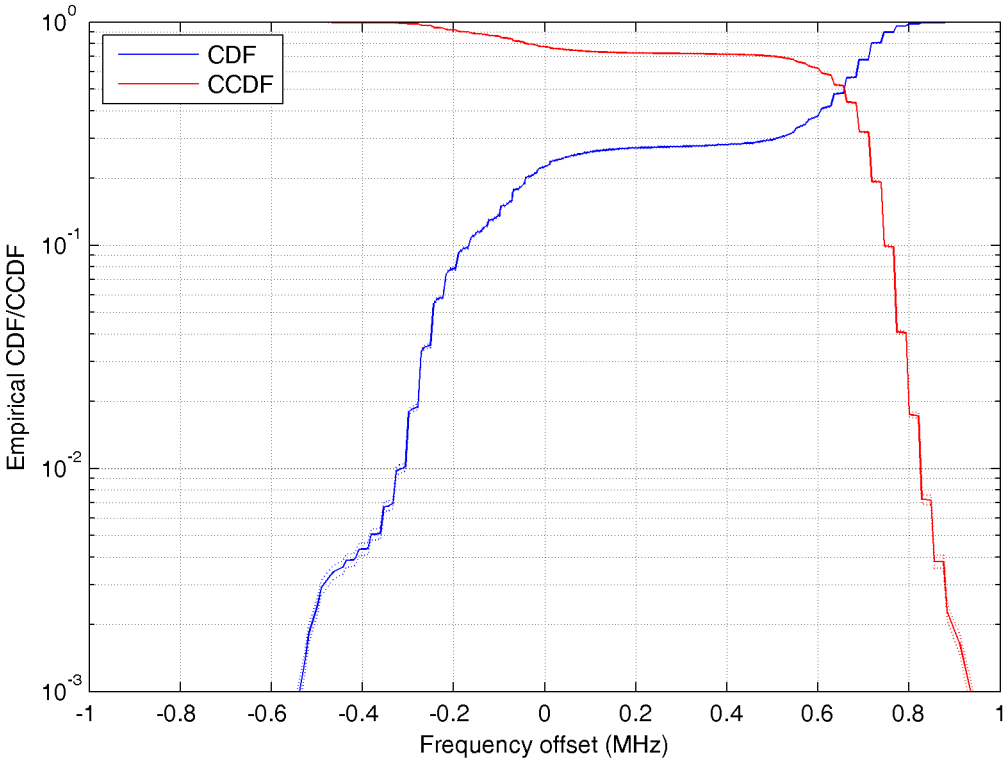

Figure 4.10: Empirical CDF and CCDF of frequency offset over all data

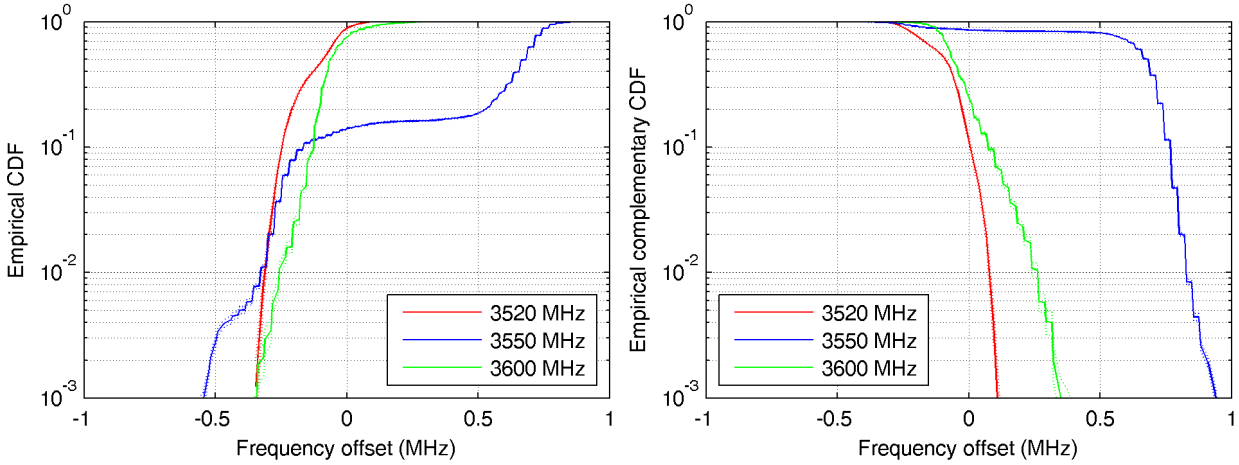

Figure 4.11: Empirical CDF and CCDF of frequency offset by center frequency

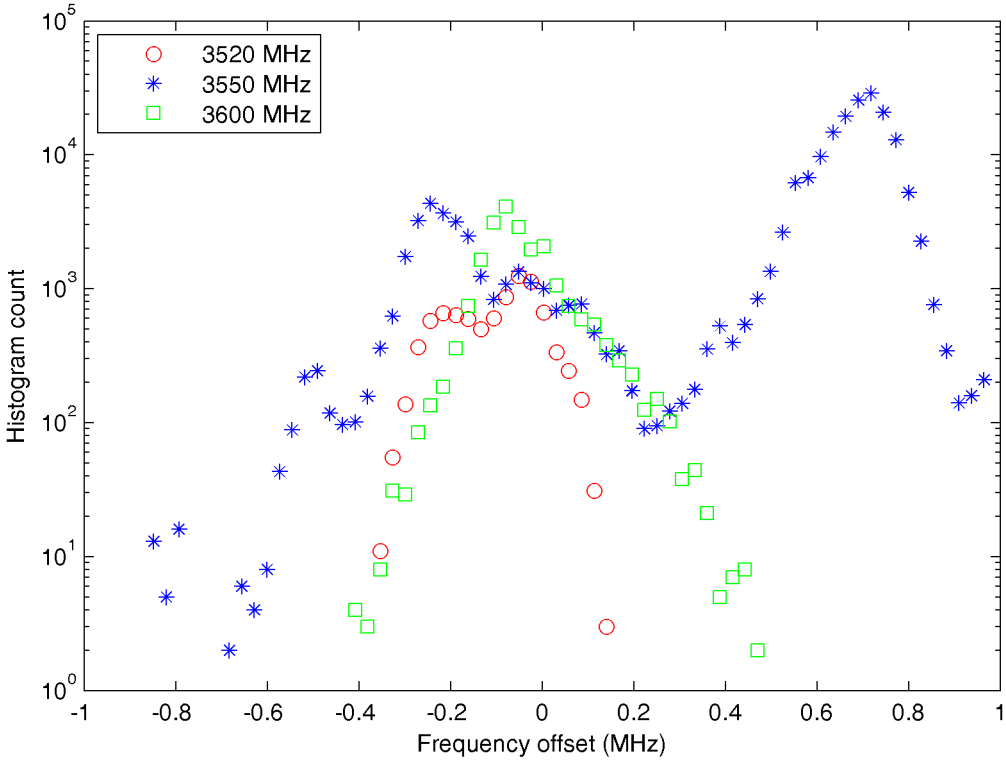

Figure 4.12: Histogram of frequency offset by center frequency

4.4 Summary statistics

Table 4.3 summarizes the mean, median, and 1st and 99th percentiles of sweep and pulse parameters by antenna. Table 4.4 summarizes the statistics of pulse parameters by frequency.

	Omni				CBS				Overall			
	Mean	Med	1 %	99 %	Mean	Med	1 %	99 %	Mean	Med	1 %	99 %
Sweep Interval (s)	3.860	3.855	3.844	3.879	4.012	3.850	3.825	7.722	3.902	3.854	3.833	3.885
Pulse Duration (μs)	1.174	1.173	1.102	1.218	1.160	1.160	1.102	1.200	1.171	1.173	1.102	1.213
Pulse Repet. Intrvl. – 1 ms (ns)	11	13	-4	22	13	13	-18	44	12	13	-9	31

Table 4.3: Statistics of sweep and pulse parameters by antenna: mean, median, 1^{st} percentile (1 %), and 99^{th} percentile (99 %)

	3520 MHz				3550 MHz				3600 MHz			
	Mean	Med	1 %	99 %	Mean	Med	1 %	99 %	Mean	Med	1 %	99 %
Pulse Duration (μs)	1.158	1.160	1.111	1.182	1.174	1.173	1.120	1.209	1.144	1.147	0.973	1.364
Pulse Repet. Intrvl. – 1 ms (ns)	18	18	-13	49	12	13	-4	31	6	4	-27	36
Frequency Offset (kHz)	-96	-71	-291	93	546	690	-326	828	-37	-43	-256	266

Table 4.4: Statistics of pulse parameters by center frequency

Chapter 5

Conclusions

The Point Loma measurement campaign resulted in a total of 8543 60-s power spectra and 1863 high-resolution 60-s waveforms. Over the course of these measurements, the target SPN-43 radar system was observed at three different operational frequencies: 3520 MHz, 3550 MHz, and 3600 MHz. In addition to observing SPN-43 at these frequencies in "normal" operation, the following phenomena were observed and are documented in this report:

- Tuning of the radar across a contiguous range of frequencies
- Two radars operating simultaneously on the same frequency channel
- Adjacent-band emissions into the band of interest
- In-band, frequency-hopping, narrowband emissions from an unknown source

Furthermore, the adjacent-band emissions were frequently observed to be coincident and co-channel with SPN-43 emissions, indicating that the adjacent-band emissions could confound SPN-43 detection by an ESC.

A subset of the high-resolution IQ waveforms containing no adjacent-band or other in-band emissions was selected for further statistical analysis. This analysis focused on key parameters of the target radar that could aid detection, namely, the antenna rotation period, pulse repetition interval, pulse duration, and center frequency. The subset of approximately 800 "clean" acquisitions of in-band radar consisted of $11\,300$ sweeps of the main beam and $223\,000$ individual pulses ranging in peak power by over 40 dB. The statistical analysis of in-band radar parameters yielded the following observations.

- The median antenna rotation period was 3.85 s, 0.15 s lower than reported in the SPN-43 system manual dated 2005 [5]. The difference between the 1st and 99th percentiles (containing $98\,\%$ of the observations) was only 0.05 s.

- The median pulse repetition interval was very close to the nominal value of 1 ms (only 13 ns greater). Furthermore, $98\,\%$ of the values were confined to a range of only 40 ns.
- The overall median pulse duration was $1.17\,\mu$s and varied by $0.027\,\mu$s across the three observed frequencies. However, the tails of their distributions differed more significantly, with the $98\,\%$ spread reaching $0.4\,\mu$s, or $34\,\%$ of the median. The median pulse duration observed here differs by $0.22\,\mu$s from that reported in the SPN-43 system manual [5].
- The median frequency offset from the nominal center frequency ranged from 43 kHz to 690 kHz across the three observed frequencies, and their $98\,\%$ spreads varied from 384 kHz to 1.15 MHz.

Knowledge of these statistics can be used to develop robust ESC detectors. They can also inform the development and selection of waveforms with which these detectors can be tested by a certification body.

Chapter 6

Areas for Future Research

A potential near-term use of the 3.5 GHz waveforms collected in this study is for controlled testing of CBRS ESC systems. At a minimum, the analysis of pulse and sweep parameters provided in Chapter 4 can inform the parametrization of surrogate waveforms being developed by NTIA/ITS for laboratory testing of ESC detectors.

Furthermore, the waveforms themselves could be "played back"—that is, converted to an analog signal and upconverted to the appropriate RF frequency—by a vector signal generator to evaluate the performance of an ESC detector. A benefit of playing back the measured waveforms is that the effects of the propagation channel, which can distort the signal, are inherent in these waveforms. Hence, the measured waveforms better reflect the actual signals an ESC will receive in the field. Future work could determine an appropriate subset of the collected waveforms that represents the range of parameters, channel conditions, and signal-to-noise ratios that were observed in the field.

Waveform recordings and pulse parameters at lower power and SNR might be used to better inform the use of surrogate waveforms or waveform play back. Future work could use equipment with a lower noise figure and focus on measuring signals at a lower trigger threshold. Alternatively, the existing measurements might be better explored with more robust pulse detection and parameter estimation algorithms or algorithms that are more informative about the pulse shape, such as second and higher order moments of the pulse delay spread.

The primary federal incumbent radar system in 3550 MHz to 3650 MHz is the SPN-43 air traffic control radar [9], and the emissions of that system were the focus of this study. However, future Navy maritime radars are under development that will also occupy this band, and their emissions will need to be detected by an ESC, as well. Since the waveforms of these future radars are classified, an important area of future research is the development of surrogate waveforms for

these radars that can be used for the design, development, and testing of ESC detectors.

The research and development of surrogate waveforms for future radars should encompass the validation of the surrogate waveforms against real emissions of these radars. Such a validation could include testing detection algorithms with both the surrogates and the real signals to ensure they elicit comparable detection performance across a range of operating conditions.

Finally, research into channel models and their validation for the 3.5 GHz band would be valuable on two fronts. First, measurements of propagation loss across a wide range of transmitter-receiver locations, antenna heights, and clutter environments would help to validate existing and future models. These models are being used to develop static CBRS exclusion and protection zones and will be used by a CBRS Spectrum Access System for dynamic aggregate interference computations.

Second, *wideband* channel models that include the effects of the channel on pulse shape could be used in conjunction with the surrogate waveforms to render them more realistic. Convolving idealized radar signals with a time-varying channel impulse response derived from field measurements would emulate the dispersive and fading channels that will be encountered by ESC detectors in the field. Hence, the wideband channel models derived from this research would potentially improve the fidelity of tests employing surrogate waveforms.

Bibliography

[1] "Amendment of the commission's rules with regard to commercial operations in the 3550–3650 MHz band." FCC Report and Order and Second Further Notice of Proposed Rulemaking, GN Docket No. 12-354, Apr. 2015.

[2] "Citizens broadband radio service." 2 C.F.R. § 96, 2016.

[3] *Military Standardization Handbook*. Department of Defense, MIL-HDBK-162B, Dec. 1973.

[4] M. G. Cotton and R. A. Dalke, "Spectrum occupancy measurements of the 3550–3650 megahertz maritime radar band near San Diego, California," Technical Report TR 14-500, National Telecommunications and Information Administration, Jan. 2014.

[5] "Operation and maintenance instructions, organizational level, radar set AN/SPN-43C." Naval Air Systems Command, Technical Manual, EE216-EB-OMI-010, vol. 1, Sept. 2005.

[6] "Government briefing on AN/SPN-43C radar set capabilities/interfaces." Wireless Innovation Forum Document WINNF-16-I-0105, Jan. 2016.

[7] F. H. Sanders, J. E. Carroll, G. A. Sanders, and L. S. Cohen, "Measurements of selected naval radar emissions for electromagnetic compatibility analyses," Technical Report TR 15-510, National Telecommunications and Information Administration, Oct. 2014.

[8] "Requirements for commercial operation in the U.S. 3550–3700 MHz citizens broadband radio service band." Wireless Innovation Forum Document WINNF-15-S-0112, Version V2.0.0, Feb. 2017.

[9] "An assessment of the near-term viability of accommodating wireless broadband systems in the 1675–1710 MHz, 1755–1780 MHz, 3500–3650 MHz, 4200–4220 MHz and 4380–4400 MHz bands," tech. rep., U.S. Department of Commerce, National Telecommunications and Information Administration, Oct. 2010.

[10] J. A. Jargon, D. F. Williams, and P. D. Hale, "Developing models for type-N coaxial VNA calibration kits within the NIST microwave uncertainty framework," in *Proc. 87th ARFTG*

Microwave Measurement Conference, (San Francisco, CA), May 2016.

[11] I. BIPM, IEC, IFCC, ILAC, ISO, IUPAC and OIML, *Evaluation of measurement data: Guide to the expression of uncertainty in measurement*. Joint Committee for Guides in Metrology - JCGM 100:2008, Sept. 2008.

[12] T. E. Parker, S. R. Jefferts, and T. P. Heavner, "Medium-term frequency stability of hydrogen masers as measured by a cesium fountain," in *2010 IEEE International Frequency Control Symposium*, pp. 318–323, June 2010.

[13] R. J. Matheson, J. D. Smilley, G. D. Falcon, and V. S. Lawrence, "Output tube emission characteristics of operational radars," Technical Report TR 82-92, National Telecommunications and Information Administration, Jan. 1982.

[14] T. E. Ruden, "Design and performance of a one megawatt, 3.1–3.5 GHz coaxial magnetron," in *1979 9th European Microwave Conference*, pp. 731–735, Sept. 1979.

[15] M. Labitt, "Coaxial magnetron spectra and instabilities," Project Report ATC-74, Lincoln Laboratory, Massachusetts Institute of Technology, June 1977.

[16] "Electromagnetic compatibility criteria for navy systems." NAVSEA S9407-AA GYD-010/Sop-3840 Rev 5, classified SECRET, Jan. 2016.

[17] W. N. Venables and B. D. Ripley, *Modern Applied Statistics with S*. New York: Springer, 4th ed., 2013.

[18] "IEEE standard for transitions, pulses, and related waveforms," *IEEE Std 181-2011 (Revision of IEEE Std 181-2003)*, Sept. 2011.

Appendix A

Data Processing Algorithms

A.1 Pulse selection

For data analysis, we first identify datasets having the desired in-band radar signal. We then discard datasets with significant emissions from adjacent-band emitters.[1] To describe how we select pulses for analysis, or to describe which data we define as a pulse, we first define a sweep as a series of pulses observed when the main beam of the radar travels across our antenna due to the radar's azimuthal rotation. This can be observed in Figs. 3.1 and 3.2. To identify a sweep for analysis consists of finding the local maxima of the amplitude of our I/Q data. We used our spectrogram metadata, specifically we used a spectrogram projected onto its time axis, to look for local maxima. To determine which local maxima to analyze as a sweep, we required sweeps to have a fixed minimum power of -67.8 dBm in a frequency bin, referenced to the antenna output, and a minimum separation of 3.185 s.

Once we identify sweeps for analysis, we next identify pulses for analysis in each sweep. To identify pulses we load a segment (~ 0.455 s of data) that was identified to include a sweep. We find the maximum amplitude and location of this maximum amplitude for the segment. For further analysis, we next reduce the data in memory to 0.25 s of data centered about the maximum amplitude in the segment. As an aside, our algorithm was freeing memory as often a possible due to the large data sizes and the desire to run processes in parallel.

To identify pulses in this 0.25 s of data we look for connected segments within 3 dB of the maximum sweep power. We determine if there is a sample within each ~ 0.5 ms of data having

[1] The algorithm for identifying datasets with emissions from adjacent-band emitters looks for energy above a threshold outside a 20 MHz window centered on the target in-band radar signal. This same procedure eliminates data sets with spurs due to VST saturation.

an instantaneous power within 3 dB of this maximum, working from the maximum power sample outwards. When two consecutive sections of ~ 0.5 ms fail this threshold test, then our test for the connected region is complete. Using this connected region for further analysis we have reduced the 0.25 s of data to a smaller section containing data within 3 dB of the maximum power.

Finally, we identify local maxima, now defined as pulses, having an instantaneous power within 3 dB of the peak sweep power and a minimum separation of 100 μs. We use the locations of these local maxima for analysis of pulse parameters.

A.2 Pulse processing

We calculate the frequency for each pulse by finding the bin of its FFT that has the maximum amplitude. As we use 8192 samples around each pulse, and having acquired data with a sampling rate of 225 MSamples/s, our frequency resolution is approximately 27.5 kHz.

We next demodulate the pulse to zero frequency using the pulse frequency found above. We then low-pass filter the pulse to remove noise. More specifically, we use an infinite impulse response (IIR) Butterworth low-pass filter, with a 10 MHz passband and 15 MHz stopband, and a zero phase filtering algorithm. We note this signal processing leads to improved performance of our pulse parameter algorithms with little measurable distortion. Following this processing, we next find the pulse durations and pulse repletion interval.

Our pulse duration algorithm finds the shortest time between samples below the $50\,\%$ level. In more detail, our pulse duration algorithm first requires the values of the maximum amplitude in the pulse and the amplitude of the noise. The amplitude of the noise is found using the 'shorth' method [18]. We define the $50\,\%$ level as the average of the maximum amplitude and noise amplitude. The algorithm next searches from the maximum amplitude sample outwards until it finds the first samples with amplitude less than the $50\,\%$ level, and reports the time between these samples as the pulse duration.

We calculate the pulse repetition interval by simply reporting the time between samples on the rising edge of subsequent pulses that were used to calculate pulse duration as above.

A.3 Choice of pulse duration algorithm

The pulse duration algorithm we use here is well suited for pulses such as the one shown in Fig. A.1, which has a relatively low amount of noise and roughly monotonically rising and falling tran-

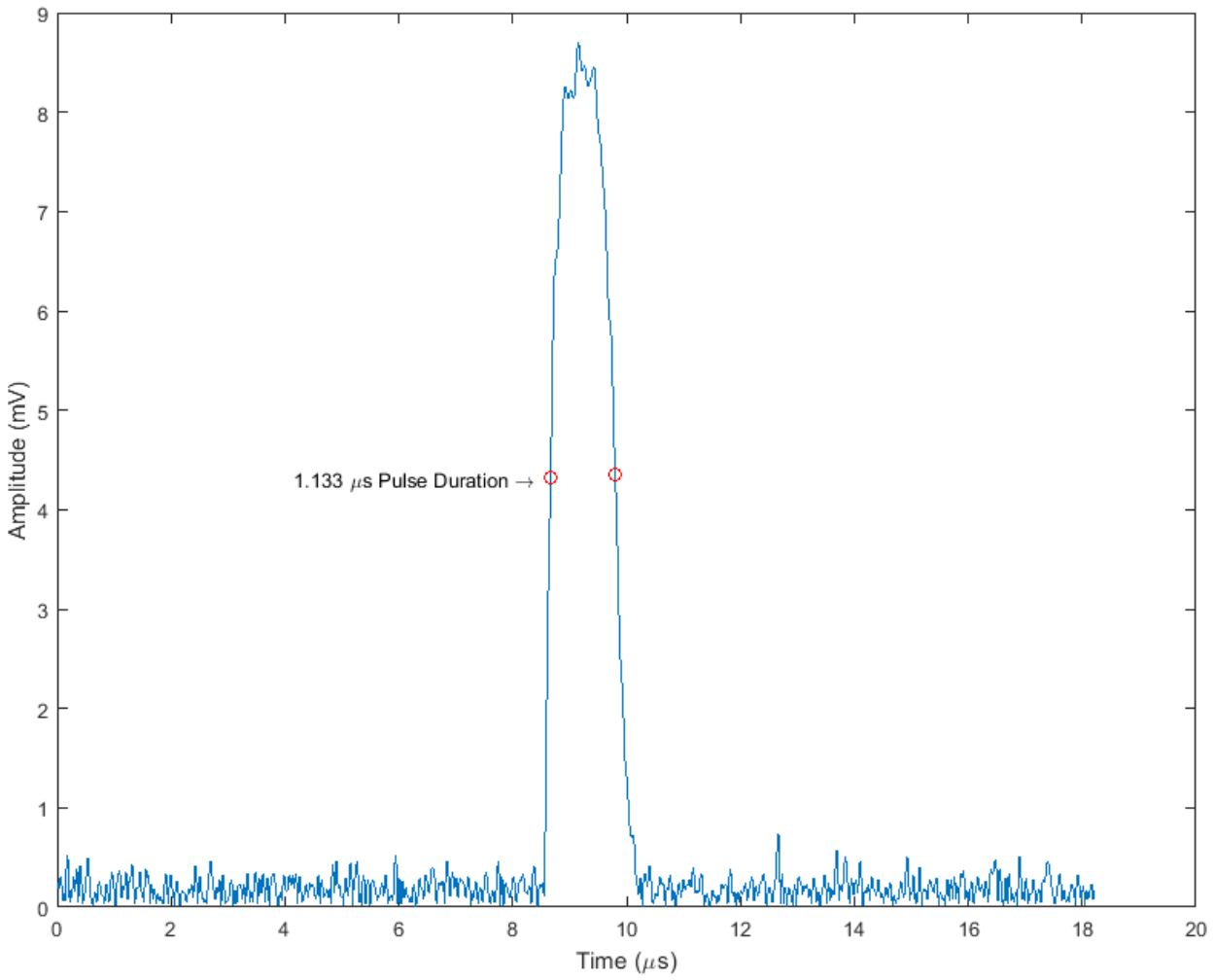

Figure A.1: Pulse example 1

sitions. In the presence of strong multipath, the algorithm can become unstable, as demonstrated in Figs. A.2 and A.3, where the depth of the local minimum between pulses is near the $50\,\%$ level. More robust pulse duration estimators may be useful for exploring the subtleties of our measured pulses but are beyond the scope of the present document.

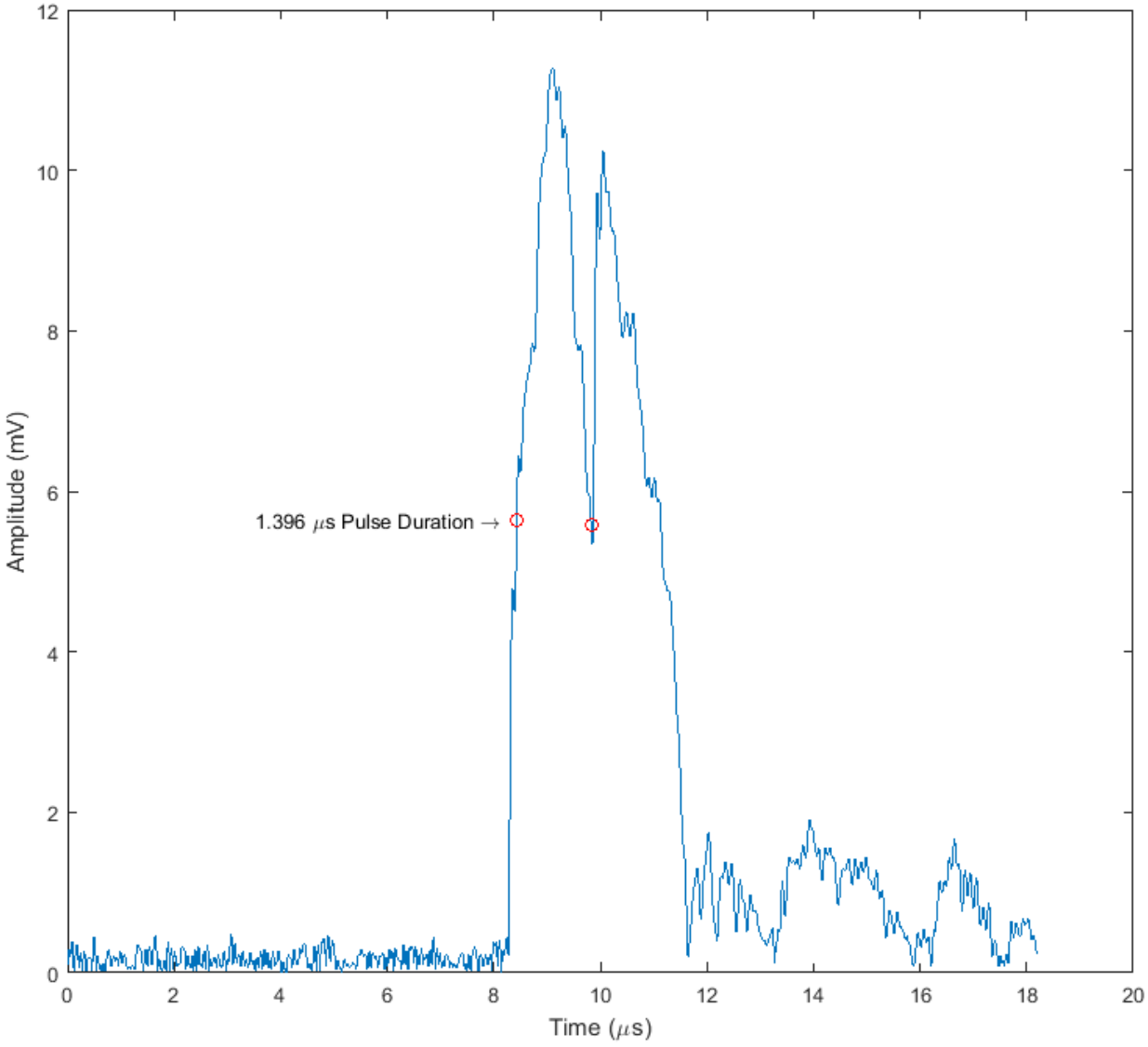

Figure A.2: Pulse example 2, with local minimum slightly lower than the $50\,\%$ level V_{50}.

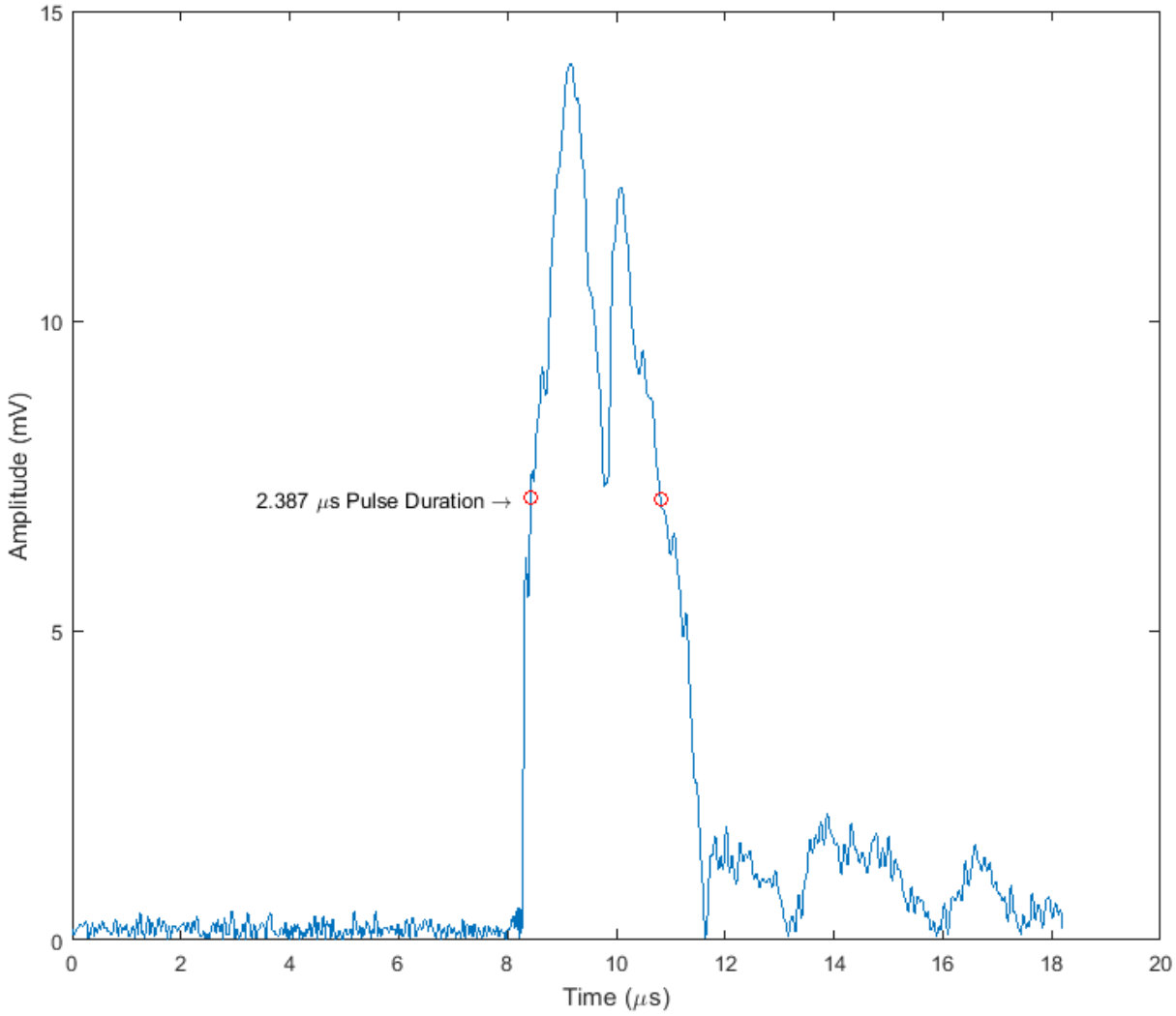

Figure A.3: Pulse example 3, with local minimum slightly higher than the $50\,\%$ level V_{50}.